Red emission of Praseodymium ions (Pr^{3+})

By

Luyanda Lunga Noto

(B.Sc. Hons.)

This thesis is submitted in fulfillment of the requirements for the degree

Magister Scientiae

in the

Faculty of Natural and Agricultural Sciences

Department of Physics

Bloemfontein campus

at the

University of Free State

Promoter: Prof. H.C. Swart

Co – Promoter: Prof. J.J. Terblans

November 2011

This thesis is dedicated to people who shaped my thoughts positively

Nobenza Ruth Noto (25/09/1935 - 22/04/2008)

Mr. M. J. Mahokoto (Wongalethu Sen. Sec. Physical Science teacher)

Ms. M.T. Hermanus (Wongalethu Sen. Sec. Mathematics teacher)

The whole community of Bethulie

Acknowledgements

I have been much honored to be in the midst of several researchers who blessed my life in several ways and shaped my research aptitude. I am sending sincere gratitude to:

- ***Prof. Hendrik C. Swart*** (promoter) for opening the door for me to enter the world of research, and for addressing my short comings with patience.
- ***Dr. Shreyas S. Pitale*** for introducing me to Luminescence Science. Also for the fruitful discussions that he put down to develop me as a researcher.
- ***Prof. Odireleng M. Ntwaeaborwa*** for all the valuable inputs in helping me organize my ideas.
- ***Prof. J.J. Terblans*** (Co – promoter) for all valuable advices on my work.
- ***Dr. Indrajit M. Nagpure*** and ***Dr. Marek A. Gusowski*** for all the valuable discussions about my work and their inputs in developing my aptitude as a researcher
- ***Mr. Hassan Ahmed Seed*** for introducing me to the Fluorescent Carry Eclipse spectroscopy, ***Mr. Kamohelo G. Tshabalala*** and ***Mr. Moshawe J. Madito*** for introducing me to the XRD system, and ***Prof. Roos*** for his valuable advices on AES and XPS.
- University of Free State Physics department staff and fellow students for all the valuable discussions.
- I am grateful for the help that came from the ***Center of Microscopy*** (UFS), **Geology department** (UFS), Deutch Electron Synchotron (DESY) center during the course of my study
- Thank you to South African National Research Foundation for funding my research work.
- Most importantly I am grateful to God's love, my Lord who has carried me from the beginning until the end, and turned all the impossible around to ease my fear. I thank him for having blessed me with my late grandmother ***Nobenza Ruth Noto*** (1935 September 25 – 2008 April 22), who has imparted in me courage and knowledge that poverty and life difficulties are never an obstacle enough to stop one from pursuing his goal, and to whom I dedicate my success. Finally I express gratitude to my father ***Nzingo M. Noto*** for his financial assistance throughout my studies and also to the rest of my family.

Abstract

Red glowing phosphors were prepared by adding Pr^{3+} ions as activators to several oxide host matrixes; $CaTiO_3$, $LaTaO_4$, $YTaO_4$, and $GdTaO_4$. The perovskite $CaTiO_3:Pr^{3+}$ compound is a phosphor that glows with a single red emission around 613 nm at room temperature upon irradiation with UV light of 230 – 360 nm wavelengths or an electron beam. The source of the single red emission is the intervalence charge transfer between Pr^{3+} and Ti^{4+} ions, which opens up a channel to completely depopulate the $^3P_0$ state, by populating the $^1D_2$ state. This leads to a dominant emission coming from the $^1D_2 \rightarrow ^3H_4$ transition. The dynamics of Pr^{3+} in $YTaO_4$, $LaTaO_4$, and $GdTaO_4$ have not been explored excessively, and the resulting emission of these compounds doped with Pr^{3+} comes from both $^3P_0$ and $^1D_2$ states of Pr^{3+}.

The compounds were prepared by solid state reaction at 1200 ^oC and $CaTiO_3$ was prepared by directly firing TiO_2 (Anatase phase) and $CaCO_3$ for 4 hours. The compound was doped with several mol% concentrations of Pr^{3+} from $PrCl_3$ compound to optimize the output emission intensity. The rare-earth tantalate phosphors were prepared by directly firing Ta_2O_5 with Y_2O_3, La_2O_3, or Gd_2O_3 for 4h to obtain $LaTaO_4$, $YTaO_4$, and $GdTaO_4$ respectively. The tantalates were doped with 0.5 mol% concentration of Pr^{3+} from $PrCl_3$ and the synthesis was carried through in the presence of 30 wt% Li_2SO_4 flux agent. The role of the flux agent in this instant was to increase the reaction rate by acting as an intermediate that converts the reagents to reactive species, lower the reaction temperature required for the final compound to form and to facilitate crystallinity and to control particle sizes.

The phase of the phosphor compounds was identified by using X-ray diffraction (XRD, Bruker AXS D8 Advance). The XRD patterns of $CaTiO_3$ with different Pr^{3+} concentrations match that of the standard orthorhombic $CaTiO_3$ (JCPDS card no. 22-0153). The XRD patterns of $LaTaO_4$, $YTaO_4$, and $GdTaO_4$ with 0.5 mol % of Pr^{3+} suggest the presence of the reagent ions in the final product. The surface morphology of the compounds was traced using Scanning Electron Microscopy (SEM) and that of $CaTiO_3$ showed particles of different shapes and sizes. The SEM

shows the surface morphology of $GdTaO_4$ and $LaTaO_4$ to be of particles with different shapes and also to have sharp edges.

The luminescence properties of $CaTiO_3:Pr^{3+}$, $LaTaO_4:Pr^{3+}$, $YTaO_4:Pr^{3+}$, and $GdTaO_4:Pr^{3+}$ were monitored using a PerkinElmer Lambda 950 UV/VIS spectrometer, for diffuse reflectance measurements to identity the absorbing centers in the phosphors. Photoluminescence (PL) and phosphorescence lifetime measurements of $CaTiO_3:Pr^{3+}$ were done using Varian Carry-Eclipse fluorescence spectrometer. PL of $LaTaO_4:Pr^{3+}$, $YTaO_4:Pr^{3+}$, and $GdTaO_4:Pr^{3+}$ was measured with DESY synchrotron working with photons from 50 to 330 nm wavelengths. Phosphorescence lifetime measurements and the energy distribution of localized trap levels of $LaTaO_4:Pr^{3+}$, $YTaO_4:Pr^{3+}$, and $GdTaO_4:Pr^{3+}$ were measured using Thermoluminescence (TL) 10091, NUCLEONIX spectrometer.

$CaTiO_3:Pr^{3+}$ phosphor with a single red emission peak around 613 nm is co-doped with In^{3+} to charge compensate the local sites where a trivalent ion Pr^{3+} substitutes for a divalent ion Ca^{2+}. It is found that In^{3+} charge compensation from 0.05 to 0.1 mol% has an effect of enhancing the red emission intensity and afterglow decay time of $CaTiO_3:Pr^{3+}$. The lifetime measurements were carried out using Varian Carry-Eclipse for $CaTiO_3:Pr^{3+}$ co-doped with different In^{3+} concentrations and using (TL) spectroscopy at 30 ^{o}C for $LaTaO_4:Pr^{3+}$, $YTaO_4:Pr^{3+}$, and $GdTaO_4:Pr^{3+}$. The phosphorescence lifetime (**τ**) observed for different In^{3+} co-doped in $CaTiO_3:Pr^{3+}$ was 7.6 s for 0.05 mol% In^{3+}, 11.2 s for 0.1 mol% In^{3+}, 6.3 s for mol% In^{3+} and 2.03 s for mol% In^{3+}. For the orthotantalates it was approximated 620 s for $GdTaO_4:Pr^{3+}$, 655 s for $YTaO_4:Pr^{3+}$ and 663 s for $LaTaO_4:Pr^{3+}$. The depth of the trap levels was investigated using TL and were found to be residing at 0.71, 0.83, 1.02 and 1.48 eV depths for $GdTaO_4:Pr^{3+}$, at 0.68, 1.02, 1.43, and 1.60 eV depths for $YTaO_4:Pr^{3+}$ and at 0.46, 0.55 and 0.75 eV depths for $LaTaO_4:Pr^{3+}$.

Surface chemical stability is an important parameter for phosphors that are projected for industrial purposes, such as the manufacturing of field emission displays (FED) screens and others. The surface chemical stability and its effects on CL intensity under prolonged electron

beam irradiation were investigated, for $CaTiO_3:Pr^{3+}$, $LaTaO_4:Pr^{3+}$, $YTaO_4:Pr^{3+}$ and $GdTaO_4:Pr^{3+}$ in-situ using AES (PHI 549) at 1×10^{-8} Torr and 1×10^{-6} Torr O_2 .

The resulting surface chemical state changes were traced using PHI 5000 *versa-probe* XPS. The XPS revealed that on the surface of $CaTiO_3:Pr^{3+}$ new species such as CaO and CaO_x suboxide non luminescent layers had formed on the surface during the electron beam irradiation process as per the ESSCR mechanism. On the surfaces of the tantalate phosphors there was also a formation of sub oxides due to the electron stimulated surface chemical reaction (ESSCR) that is stimulated by the prolonged electron beam irradiation. These showed stability under the electron beam irradiation.

Keywords

Solid State reaction, Intervalence charge transfer, Charge compensation, Photoluminescence, Cathodoluminescence, electron trapping centers, Thermoluminescence

Acronyms

IVCT - Intervalence charge transfer

XRD - X-ray Diffraction

SEM - Scanning Electron Microscopy

PL - Photoluminescence

TL - Thermoluminescence

CL - Cathodoluminescence

DESY - Deutsches Electronen Synchrotron

FED - Field Emission Spectroscopy

AES - Auger Electron Spectroscopy

APPH	-	Auger peak-to-peak heights
XPS	-	X-ray Photoelectron Spectroscopy
ESSCR	-	Electron Stimulated Surface Chemical Reaction
DLTS	-	Deep Level Transient Spectroscopy
CIE	-	Mathematical model describing the way colors can be represented
Torr	-	133.32 Pa

Table of contents

Title and affiliation i

Dedication ii

Acknowledgement iii

Abstract iv

Keywords vi

Acronyms vi

Table of Contents viii

Chapter 1

Introduction

1.1. The source of Light 1

- 1.1.1. Incandescence 1
- 1.1.2. Luminescence 1
- 1.1.3. Absorption 2
- 1.1.4. Absorption in activated phosphors 3

1.1.5. Conditions for luminescence 3

1.2. Problem statement 5

1.3. Objectives of the study 6

1.4. Layout of the thesis 7

1.5. References 8

Chapter 2

Properties of $CaTiO_3$ and (Y,La,Gd)TaO_4

2.1. Project based phosphors 10

2.1.1. Background of $CaTiO_3$:Pr^{3+} 10

2.1.1.1. Perovskite materials 10

2.1.1.2. Stochiometry 11

2.1.1.3. Crystallography 11

2.1.1.4. $CaTiO_3$ crystal structure 12

2.1.1.5. $CaTiO_3$:Pr^{3+} crystal structure 14

2.1.1.6. Pr^{3+} ions luminescence states 15

2.1.1.7. Red emission of Pr^{3+} in $CaTiO_3$ 16

2.1.1.8. Intersystem crossing 17

2.2.1.9. Afterglow mechanism in $CaTiO_3:Pr^{3+}$ 19

2.1.2. Ortho-tantalate phosphors 20

2.1.3. Luminescence and trap centers in $(Y,La,Gd)TaO_4:Pr^{3+}$ 22

2.2. Synthesis method 23

2.3. Reference 25

Chapter 3:

Experimental Characterization Techniques

3.1. X- ray diffraction 29

3.2. Scanning Electron Microscopy 32

3.3. Photoluminescence Spectroscopy and Synchrotron 33

3.4. Thermoluminescence Spectroscopy 35

3.5. Ultraviolet-Visible absorption Spectroscopy 37

3.6. Cathodoluminescence and Auger Electron Spectroscopy 49

3.7. X-ray Photoelectron Spectroscopy 41

3.8. References 44

Chapter 4

In^{3+} Charge compensation of $CaTiO_3:Pr^{3+}$

4.1. Introduction 46

4.2. Experimental 47

4.3. Results and Discussion 48

4.4. Conclusion 60

4.5. Reference 61

Chapter 5

Surface chemical changes of $CaTiO_3:Pr^{3+}$ upon electron beam irradiation

5.1. Introduction 62

5.2. Experimental 63

5.3. Results and Discussion 63

5.4. Conclusion 71

5.5. Reference 72

Chapter 6

Luminescent dynamics of Pr^{3+} in $MTaO_4$ host

6.1. Introduction 73
6.2. Experimental 74
6.3. Results and Discussion 75
6.4. Conclusion 88
6.5. Reference 89

Chapter 7

CL emission degradation of rare-earth tantalate phosphors

7.1. Introduction 91
7.2. Experimental 92
7.3. Results and Discussion 93
7.4. Conclusion 103
7.5. Reference 104

Chapter 8

Summary and Future work

8.1. Summary 106

8.2. Future Work 108

8.3. Publications 109

8.4. Research presentations 110

1

Introduction

1.1. The source of light

People living in rural areas depend on candles and paraffin or oil powered lamps to light their homes at night. Not only are these options dangerous, and harmful to the environment, they also negatively impact health, education, and safety [1]. The ever developing technology has come up with different forms of materials that supply us with different forms of light energy, like; incandescence and luminescence emitting materials.

1.1.1. Incandescence

This type of emission has been available for some time, both during the day from the sun and during the night from light bulbs [2]. Incandescent lamps emit visible electromagnetic waves at temperature above 500 ^{o}C, due the heating effect they are subjected to when an electric current is passed through their filaments. The emitted continuous band of light has a peak that depends on the temperature of the filament [3].

1.1.2. Luminescence

This is an emission of visible or near visible electromagnetic radiation as a result of re-emission of absorbed external energy by the radiated material, which brings about the transition of electrons from the valence to the conduction band of the material. The energy that is transmitted to the material to give rise to luminescence may come from different sources. The one that comes from the absorption of electromagnetic waves is referred to as photoluminescence, cathodoluminescence from an electron beam, electroluminescence from an electric field, and sonoluminescence from sound waves [4,5,6].

When a certain luminescent material is subjected to an excitation by an external source, it may emit light whilst still subjected to the excitation source and stop after it has been removed. Such luminescence is referred to as fluorescence. In the case of some materials, luminescence may continue for a considerable interval after the source of excitation has been removed. Such luminescence is then referred to as phosphorescence or afterglow [5].

1.1.3. Absorption

Different types of semiconductor materials are employed in a variety of applications, like: photodiodes, photovoltaic cells and others. When a semiconductor material is directed upon by an energetic radiation, the accompanying energetic particles may be absorbed, reflected or scattered by the heavy nucleus of the atoms. In general, the spectral response of practical devices depends on the energy band gap and the absorption coefficient[i] of the material, and those of higher absorption coefficient absorb more energy compared to those of lower coefficient [7]. Focus is directed on the absorption of photons.

Optical absorption in semiconductor materials is mainly a mechanism that brings about the electronic transition from the valence band states to the states in the conduction band. In such kind of absorption, the wavelength of the incident electromagnetic radiation plays a big role in the absorption coefficient. As the photon energy increases, more electrons become excited to the states in the valence band, and therefore bring about increased photon absorption [7]. Equation 1 explains the relation between the absorption coefficient and the wavelength of the material.

$$\boldsymbol{\alpha = 4\pi k/\lambda} \qquad [\mathbf{1}]$$

where $\boldsymbol{\alpha}$ is the absorption coefficient, $\boldsymbol{\lambda}$ is the wavelength of the incoming electromagnetic radiation, and $\boldsymbol{k}$ is the extinction coefficient, which is a factor that determines how much light of a particular wavelength a material can absorb [7]. Absorption may change the luminescent properties of a material enormously depending on the number of impurities that may be introduced into it, and also the size of the particles used to enhance luminescence. Discussion is now extended to the absorption in activator based phosphors.

---

[i] Absorption coefficient is a factor that determines how far in the material the incident energetic particle will be absorbed.

1.1.4. Absorption in rare-earth activated phosphors

Most luminescent materials (like phosphors[ii]) are not intrinsic[iii], but rather extrinsic[iv], in that they are doped with activators[v] (i.e. impurity atoms) to improve their luminescent properties. For such materials the emission of light is owed to both the host and the activator [8]. The addition of the impurity atoms to the host (matrix) brings about defects and deviation from stochiometry introduced by a physical or chemical process under which the dopants are incorporated in the material [8].

The incorporation of activators in the host material gives rise to unusual and discrete energy levels, and become centres that are active to give luminescence. The impurities reside in the energy band gap and thus reduce the amount of energy needed to generate an electron – hole pair. This increases the photon wavelength with which the phosphor is radiated. However some impurities do not act as activators, but as killers and quenchers [8].

1.1.5. Conditions for luminescence

The energy absorbed from incident radiation by a luminescent material may be dissipated by an emission of light or may even be quenched (i.e. non-radiative transition as a result of loosing energy to heat). The condition for luminescence is explained using potential energy curves of both the ground and excited state that have minima. Thus a stable energy position can be attained. At or near room temperature, the minima of the excited and ground state do not occur at the same configuration coordinate, because of thermal vibrations that increase interactions between the luminescent centre and its environment [5].

[ii] Luminescent material that emits light mainly as a result of dopants

[iii] Intrinsic materials are pure semiconductors without any significant dopants.

[iv] A material that has appreciable amount of dopants incorporated into its structure.

[v] Dopant atoms that have an ability to improve the luminescence of a phosphor material.

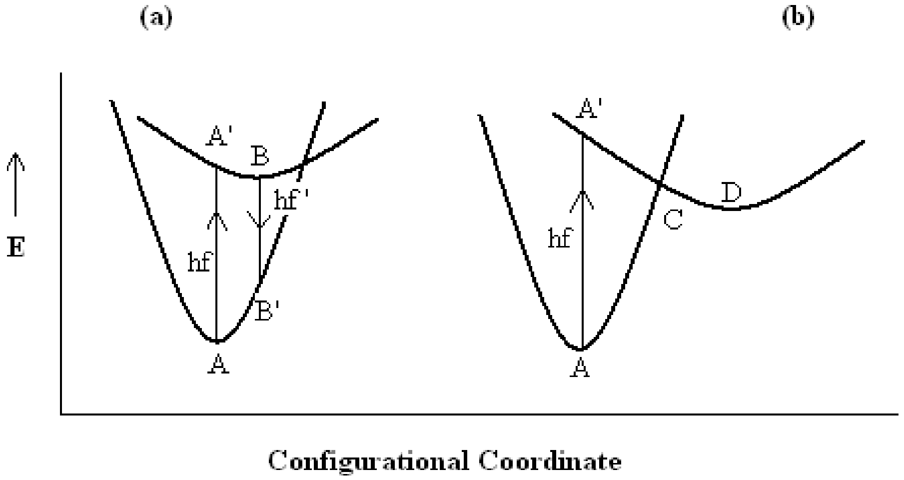

Figure 1.1: Luminescence condition for absorbed radiation energy: (a) potential curves to explain light emission, (b) potential curves used to explain quenching.

Figure 1.1a; absorption of an incident radiation brings about transition from point **A** → **A'**. Since the latter position is not stable, the carriers make a non-radiative transition to a stable configuration (point **B**). When de-excitation takes place, the system undergoes a transition from **B** → **B'** by an emission of electromagnetic radiation (photons). The system then again attains a stable configuration in the ground state (point **A**) from an unstable one (point **B'**) by undergoing non-radiative transition [5].

Figure 1.1b; as a result of increased thermal vibrations, the minimum of the excited state is positioned completely beyond the interaction with ground state potential curve. After the transition **A** → **A'**, system tends to shift towards a stable configuration (point **D**). However, before this is achieved, most energy is quenched as result of the non-radiatively transition from **C** → **A** due to the strong coupling of the two potential curves [5].

However the miss alignment of the potential of the excited state and that of the ground state is not the only factor that may suppress luminescence of phosphor materials. Luminescence may be suppressed by the excess amount of atoms doped into the host (concentration quenching) [9].

1.2. Problem statement

Phosphors with a colour index that matches that of pure blue and green have already made it to the commercial sector. However properties of red glowing phosphors prohibit them from making it to the market. Up to now Y_2O_3:Eu^{3+} phosphor with CIE coordinates of (0.64, 0.36), and with a reddish-orange colour is industrially accepted as a red phosphor for television displays because of its intense and sharp emission line, which surpasses that of all other red glowing phosphors. There are expensive adaptations required to improve the colour rendering index of Y_2O_3:Eu^{3+} and make it more reddish, such as filtering which is expensive to achieve. Together with this, is the expensive excitation close to mercury excitation at 254 nm [10,11,12,13].

Such parameters lead to expensive prices for devices that require a light emission, and amongst those is television displays. Although it is difficult to synthesize red glowing phosphors, an effort is a necessity. The sense of difficulty arises because there is no phosphor compound that glows with a red emission that is near to that of ideal red light with CIE coordinates of (0.63, 0.33). Praseodymium (Pr^{3+}) doped $CaTiO_3$ is however a promising red phosphor that glows with a single red light emission around 613 nm wavelength. The red emission of $CaTiO_3$:Pr^{3+} has CIE coordinates (0.680, 0.311) that are near to those of the ideal red light [10,11,12,13].

However the intensity of the $CaTiO_3$:Pr^{3+} needs to be improved and the mechanism behind the single red emission needs to be better understood. The latter will help in the purification of the phosphor's red light with a pursuit to make its colour rendering index close to that of ideal red light. The aim of the study is partly to understand the mechanism behind the single red emission of $CaTiO_3$:Pr^{3+} at room temperature, and also to improve the intensity of the phosphor by reducing the density of quenching centres that are generated as a result of charge imbalance. The charge imbalance arises as a result of Pr^{3+} substitution in of Ca^{2+} during the synthesis process [13].

Phosphorescent materials have an ability to trap the excitation energy and release it gradually over time. This accounts for the long afterglow that is observed from such materials. Phosphorescent devices can be used as energy conservation devices such as a multi colour signboard for road traffic regulation at night. Well developed phosphorescent materials can be used in households as white lamps, which absorb radiation from the sun and emit white light throughout the night inside the houses. This would require well developed blue, red, and green phosphorescent phosphors. However phosphorescent compounds that emit red light are not yet well developed as blue and green phosphorescent phosphors, and this too probes the need to research more on red phosphors. [14].

Part of this work focuses on phosphorescence of red emitting phosphors such as $CaTiO_3$:Pr^{3+}, $YTaO_4$:Pr^{3+}, $GdTaO_4$:Pr^{3+}, and $LaTaO_4$:Pr^{3+}. The aim was on measuring the lifetime of their phosphorescence and to approximate the depth of the electron traps that lie within the forbidden region of these materials.

The chemical stability of the phosphor materials is important because it partly contributes to the lifespan of the CL emission intensity. Most materials that are chemically unstable phosphors oxidize in the long run, and this may compromise the CL intensity. Such properties are very important for phosphors that are to be projected for industrial purposes, like television screens. The need to investigate the chemical stability is in general very important for application purposes to insure longer lasting luminescence [15,16].

Studies to investigate the surface chemical stability of $CaTiO_3$:Pr^{3+}, $YTaO_4$:Pr^{3+}, $GdTaO_4$:Pr^{3+} and $LaTaO_4$:Pr^{3+} were done *in-situ* using an Auger electron spectroscopy (AES). The chemical changes that take place under electron beam exposure were traced using X-ray photoelectron spectroscopy (XPS).

1.3. Objectives of the study

- To prepare $CaTiO_3$:Pr^{3+}, $YTaO_4$:Pr^{3+}, $GdTaO_4$:Pr^{3+} and $LaTaO_4$:Pr^{3+} phosphors by solid state reaction.
- Characterize luminescence properties of the phosphors using PL and UV/V spectroscopies.
- Investigate the effects of electron beam irradiation on the surface of the phosphors using AES.
- Improve luminescence intensity using In^{3+} ions as charge compensators.
- Use TL spectroscopy to investigate the energy distribution of electron traps in (Gd, Y, La)TaO_4:Pr^{3+}.

- XRD and SEM will be used to identify phase formation and surface morphology, respectively.

1.4. Layout of the thesis

The work is divided into chapters

Chapter 1: The present chapter dealt with the aspects of luminescence, the factors that motivated the study, what the study aims to achieve and how the rest of the thesis is laid out.

Chapter 2: This chapter describes the crystallographic details of the materials under investigation and also the origins of luminescence are also presented in this chapter.

Chapter 3: Description of the characterization techniques that are used to probe information from the luminescent systems, which are under investigation.

Chapter 4: In^{3+} charge compensation in $CaTiO_3$:Pr^{3+} as a method of enhancing the single red luminescence of Pr^{3+} by reducing the density of the carrier trapping centres.

Chapter 5: $CaTiO_3$:Pr^{3+} is subjected to a prolonged electron beam irradiation with an intention of altering the surface chemistry in situ using an AES. The surface chemical changes are known to be the main reason behind CL intensity degradation as per the ESSCR mechanism. The XPS is used to identify the surface chemical changes that took place under the electron beam.

Chapter 6: Pr^{3+} dynamics are investigated in (Gd, Y, La)TaO_4 using DESY Synchrotron radiation for photoluminescence. The energy distribution of electron trapping centres is mapped using TL spectroscopy.

Chapter 7: CL degradation is investigated from the chemically stable compounds, (Gd,Y,La)TaO_4:Pr^{3+} at 1×10^{-6} Torr O_2.

Chapter 8: Summary of the thesis and the possible future work is presented

1.5. Reference

Text reference

[1] L.R. Uys, ***Fundamental nursing,*** 1999, Maskew Miller Longman, South Africa, p309

[2] H.B. Faber, ***Military pyrotechnics – volume 3,*** 2009**,** BiblioLife, USA, p216

[3] M.A. Cayless and A.M. Marsden, ***Lamps and Lighting***, 1983, 3rd Ed. The Pitman Press, Great Britain, p139

[4] F.G. Smith, T.A King and D. Wilkins, ***Optics and photonics-An Introduction***, 2008, 2nd Ed. John Wiley and Sons, USA, p430

[5] G.F.J. Garlick, ***Luminescent materials***, 1949, Oxford university press, London, p3

[6] M. Fox, ***Optical properties of materials,*** 2001, Oxford University press, New York, p98

[7] B.G. Yacobi, ***Semeconductor materials – An introduction to basic principles***, 2003, Kluwer Publishers, New York, p183

[8] A. Kitai, ***Luminescent materials and applications***, 2008, John Wiley & sons, England, p264

[9] M.S. Dhlamini, ***Luminescent properties of synthesized PBS nanoparticle phosphors***, 2008,[Thesis], University of Free State, South Africa

[10] C. Gheorgies, P. Boutinaud, M. Loic, V.O. Atanasiu, J. Opt. Elec. Adv. Mater. **11** (5), (2005) 583

[11] S. Li, X. Liang, J. Mater. Sci. Mater. Elec. **19** (2008) 1147

[12] W. Tang, K. Wang, B. Xuhui, D. Chen, J. Mater. Sci. **42** (2007) 9915

[13] J. Zhi, A. Chen, L.K. Ju, J. Opt. Mater. **31** (2009) 1667

[14] Mineto Iwasaki**,** Duk Nam Kim**,** Keiko Tanaka**,** Takahiro Murata**,** Kenji Morinaga, J. Sci. Tech. Adv. Mater. **4** (2), (2003) 137

[15] S.S. Pitale, V. Kumar, I.M. Nagpure, O.M. Ntwaeaborwa, E. Coetzee, and H.C. Swart, J. Appl. Phys. **109** (2011) 013105

[16] S. H. Chen, A.P Greeff, H.C. Swart, J. Lumin **113** (2005) 191

Figures

Figure 1.1 G.F.J. Garlick, ***Luminescent materials***, 1949, Oxford university press, London

2

Properties of $CaTiO_3$ and (Y,La,Gd)TaO_4

2.1. Introduction

Most inorganic compounds are activated by using rare-earth ions as dopants which act as luminescent centres. However some may emit in the absence of the rare earth ion as a result of defect levels. Phosphor compounds activated using Eu^{3+} and Ce^{3+} have been studied by doping them in several matrices, and recently attention has been on Tb^{3+} and Pr^{3+} activated compounds. Here onwards the dynamics of Pr^{3+} in $CaTiO_3$ are studied with the intention of understanding the mechanism leading to the phosphor's single red emission at room temperature. Further studies will be done on $LaTaO_4:Pr^{3+}$, $YTaO_4:Pr^{3+}$ and $GdTaO_4:Pr^{3+}$ to compare the dynamics of Pr^{3+} in the three different hosts.

2.1.1. Background of $CaTiO_3:Pr^{3+}$

Phosphor materials (e.g. $CaTiO_3:Pr^{3+}$) mainly constitute of a matrix and dopant ions. Where $CaTiO_3$ is a perovskite matrix and Pr^{3+} is the rare-earth dopant ion. Each of the two plays its role in the emission of the electromagnetic radiation, and in this case the matrix is responsible for the afterglow of the emission, and the Pr^{3+} ion plays a role in the nature of the observed emission from this phosphor material [1,2].

2.1.1.1. Perovskite materials

In general $CaTiO_3$ is an inorganic compound that exhibits a perovskite structure. Perovskite compounds play important roles in various fields, ranging from electronics because of their electronic properties that are close to those of metals, telecommunication devices because it makes devices of smaller sizes and light masses possible, and many more. These compounds have a large number of oxygen vacancies that make it valuable in catalyst researches and optical studies. The way in which perovskite compounds are designed and the environment under which they are synthesized gives them the ability to support required properties in the fields mentioned above [3, 4].

2.1.1.2. Stochiometry

The stochiometry of materials describes the chemical formulae of the material presented, the transformation from the reagents to products quantitatively and qualitatively, including the reaction equation. However not all compounds exhibit stochiometry, some are non – stochiometric. These cannot be represented by a well defined ratio of integers, and are therefore not proportioned. Often non – stochiometric compounds are solids that contain point defects (i.e. interstitial atoms, vacancies, etc.) [5].

Perovskite structures have a general stochiometry given by the formulae $\boldsymbol{ABO_3}$, where ***A*** and ***B*** represent metal cations and ***O*** often representing an oxygen anion. The two cations can assume any charges as long as their charge combination provides an aggregate of 6+ valency. This brings about charge neutrality to the compound, because the $\boldsymbol{O_3^{2-}}$ anion has valency of 6-. The cation ***A*** site may be occupied by a monovalent, divalent or trivalent ion, and ***B*** site is occupied by a transition metal (an element that can give rise to cations with an incomplete d sub-shell) ion [5].

2.1.1.3. Crystallography

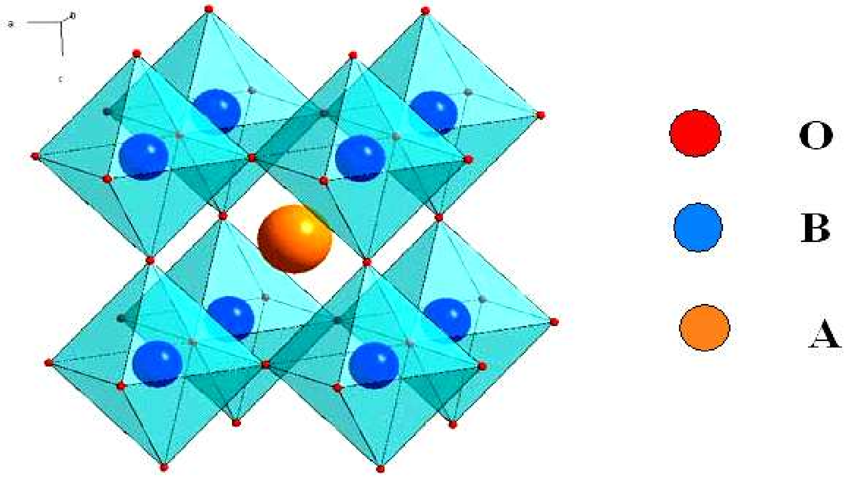

Figure 2.2: An ABO_3 Perovskite lattice structure

The traditional view of an ideal lattice structure of perovskite (fig 2.2) is that of a cubic structure, which is made of two cubic octahedron structures. The first cubic octahedron is very large and is situated at the centre of the perovskite structure, and its corner atoms are those of oxygen and encloses the large cation ***A***. The second one is a smaller – corner sharing cubic octahedron that encloses the smaller cation ***B*** in an oxygen cage [6, 7, 8].

Another way to view perovskite structures is by an 8 corner – sharing $\boldsymbol{BO_6}$ octahedron, which is often referred to as an oxygen cage, and this structure has cation ***A*** filling up the in-between space. From the view of the two octahedrons forming the perovskite structure, cation ***A*** has 12 – fold oxygen coordination (fig 2.3) in the central cubic octahedron and cation ***B*** has 6 – fold oxygen coordination in the oxygen cage (fig 2.2) [5].

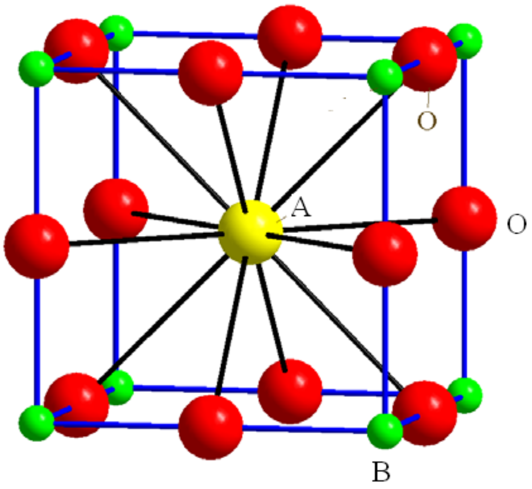

Figure 2.3: Oxygen coordination with cation ***A*** *in the central cubic octahedron of a perovskite structure*

2.1.1.4. $CaTiO_3$ crystal structure

Perovskite structures are in general very flexible in that they are able to change their structural shape in order to accommodate any change that they are subjected to. The sizes of the ions within a compound have a role of determining how straight its lattice structure can be. Hence an incorporation of cations of sizes which differ from the ideal sizes of cations ***A*** and ***B*** has an outcome that results in the structural shape of the perovskite differing from the ideal cubic structure. This is the reason for the distorted nature of most perovskites [4,9,10,11].

As mentioned above, Perovskite structures are made of a smaller corner – sharing octahedron structure that encloses cation ***B***, and a large central cube octahedron structure that encloses cation ***A***. In $CaTiO_3$ compound, the divalent Ca^{2+} cations substitute in the site of cation ***A***. The tetravalent Ti^{4+} cations tend to occupy all sites of cation ***B*** in the oxygen cage. Ca^{2+} (r = 1.42 Å) cations are too small for the ***A*** (r = 1.44 Å) cation sites that they have occupied. Therefore the perovskite structure acts to reduce the central cubic octahedron site in order for the Ca^{2+} ions to fit well. The outcome of this is the deformation from the cubic to an orthorhombic symmetry (fig 2.4) that $CaTiO_3$ compounds exhibit [10,12,13].

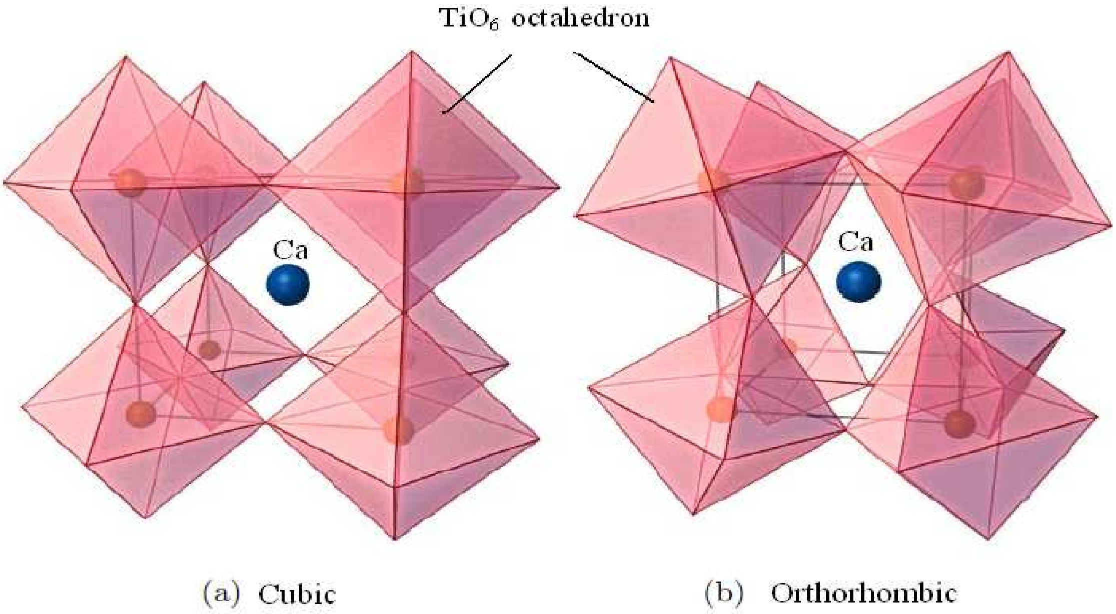

(a) Cubic (b) Orthorhombic

Figure 2.4: Perovskite distortion from an ideal cubic structure (a) to an orthorhombic structure (b)

The smaller radius of Ca ions forces the structure to reduce the **A – A** distance without having to deform the oxygen cage. Hence the oxygen cages undergo an anti – phase tilting in order to fill the space formed by a cation of a smaller radius. The degree with which the ideal perovskite structure distorts in the formation of $CaTiO_3$ compound is approximated by the Goldschmidt's tolerance factor, ***t*** (Eq. 2.1):

$$\boldsymbol{t} = \frac{(r_A + r_0)}{\sqrt{2}\,(r_B + r_0)} \qquad \textbf{[2.1]}$$

where $\boldsymbol{r_A}$, $\boldsymbol{r_B}$, $\boldsymbol{r_o}$ are the radii of the cations in the site of cations ***A*** & ***B***, and the oxygen ion, respectively. The ideal cubic perovskite has a tolerance factor, $\boldsymbol{t} = 1$, and for $CaTiO_3$ $\boldsymbol{t} = 0.97$, hence it exhibits a distorted structure. Compounds with a tolerance factor that is greater than $\boldsymbol{t} = 1$ are often stacked in a hexagonal manner. The symmetry of $CaTiO_3$ varies with temperature, and it exhibits an orthorhombic symmetry with space group *Pbnm* at temperature below 1380 K. It undergoes a phase transition between 1380 and 1500 K to a tetragonal structure, and assumes a tetragonal symmetry with a space group *14/mcm* above 1500 K. Finally at temperature above 1580 K, $CaTiO_3$ exhibits a cubic structure with a space group *Pm3m*, because the tilting of the oxygen cages disappears [4,12,14,15,16].

2.1.1.5. $CaTiO_3$:Pr^{3+} structure

Upon introducing a Pr^{3+} dopant ion to $CaTiO_3$ structure: Pr^{3+} ion of 1.14 Å radius will substitute in the site of Ca^{2+} with a radius of 1.42 Å. Activator ion doping into the matrix ($CaTiO_3$ structure) is done such that charge compensation is taken into account as the performance of this phosphor material critically depends upon it. To compensate for charge neutrality in the $CaTiO_3$:Pr compound, 2 Pr^{3+} ions are required to substitute 3 Ca^{2+} ions. The substitution of Ca^{2+} ions is the outcome of point defects in the structure of $CaTiO_3$: Pr^{3+}, which act as traps of electron transitions from the matrix valence band to the energy states of Pr^{3+} ions, by non-radiatively promoting electron-hole recombination upon excitation [10, 17].

The Pr^{3+} ions of smaller radius substitute in the site of Ca^{2+} ions and evenly reduce the large cube octahedra of the perovskite structure. Experimental studies reveal that the corner sharing oxygen cages of $CaTiO_3$ exist as a six – fold coordinated octahedron [TiO_6] and a five – fold coordinated square base pyramid [TiO_5] as a result of the tilts which the oxygen cages have undergone to accommodate the Ca^{2+} cations. The Ti – O interaction is stronger for the 6 – fold oxygen cages than those of the 5 – fold coordination [16,18,19,20].

The further distortion that is brought by the Pr^{3+} ions when they substitute in to the site of the Ca^{2+} ions, brings about the disappearance of the [TiO_6] cluster in the perovskite structure and only the emergence of [TiO_5]. This reduces the 12 – fold coordination of the ion in the **A** cation site with oxygen to 8 – fold coordination. This reduction brings about an enormous amount of oxygen vacancies, which are expected in $CaTiO_3$:Pr^{3+} phosphor. These vacancies consequently lead to the afterglow property of $CaTiO_3$: Pr^{3+} that is observed [17,21].

2.1.1.6. Pr^{3+} ions luminescence states

The luminescence observed in phosphor materials comes about as a result of the broad luminescent centres that are present within its band structure, in the form of defect structures. This includes rare-earth ions, transition-metal ions, self trapped excitons, etc. The observed luminescence spectra consist of broad emissions that come from the interactions between the electronic system of the luminescent centre and the vibrations of the ions with the atoms that surround it. For rare-earth doped phosphors; the spectra consist of sharp lines that come from the electronic transitions only. The effects of the environment on the luminescence centres that are derived from rare-earth doped phosphors mainly affect the life time of the transitions [22].

The trivalent rare-earth ions (like; Pr^{3+}, Ce^{3+}, Eu^{3+}, etc.) have *n* electrons in the 4f shell. From the resulting *Dieke* energy level diagram (not drawn to accurate scale) of Pr^{3+} ions (Fig 2.5), the meta states from which electron transitions may occur and bring about electromagnetic radiation emission, are illustrated. Pr^{3+} ions are known to emit green, blue and red colours depending on the host within which they are doped. The emission of the electromagnetic radiation comes about when the excited electrons are de-excited from a high energy level to a lower lying energy level. The energy levels of the ions are separated from each other by a certain amount of energy. This leads to the different colours that come with different electron transitions within the Meta-states [22,23].

Upon excitation, the electrons move from the valence band into the conduction band from where they are de-excited into the 4f5d state. The electrons further de-excite to the ^3P_j (j = 0, 1, 2), some to the ^1S_o state, and some to the $^1D_2$ state. The electrons from the ^1S_o state de-excite to the $^3H_4$ state and emit a green light. The electrons from the ^3P_o state may either de-excite non-radiatively down to the $^1D_2$ state or radiatively de-excite to the $^3H_4$ state and therefore emit a blue colour. The electrons in the $^1D_2$ state may de-excite to the $^3H_4$ state and therefore emit a red light whose intensity depends strongly on the excitation source [23,24].

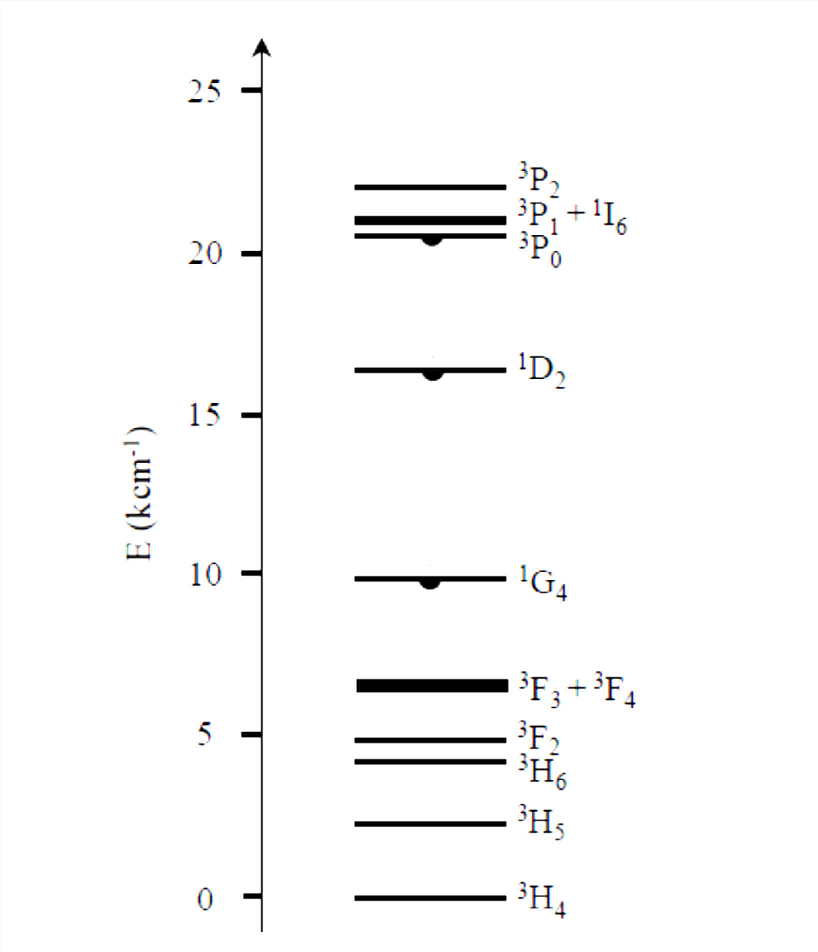

Figure 2.5: The energy level Scheme of Pr^{3+} *ions*

The luminescence behaviour of the Pr^{3+} ions is deeply affected by their distance from the O^{2-} ions or the metal ion present in the host from which it is doped. Often the bluish emission of Pr^{3+} ion is associated with rhombohedral structures, and the red emission is associated with cubic and orthorhombic structured crystals. A combination of the greenish-blue and red emission brings out the whitish emission which is observed in tetragonal phases [18,25,26].

2.1.1.7. Red emission of Pr^{3+} in $CaTiO_3$

The study of non – radiative mechanisms that are involved in between meta– states, aids with the understanding of luminescence quenching, and helps in the design of efficient luminescent materials. $CaTiO_3$: Pr^{3+} phosphor is a blue and red emitting material, and often the blue emission is quenched due to the non – radiative path – ways in between the meta– states of Pr^{3+} ions, which are available in oxide based lattices. This behaviour can either be attributed to the multi – phonon relaxation, cross relaxation and or the intersystem crossover either to the low lying 4f5d levels or through the Pr^{3+} – to – metal charge transfer (IVCT – *intervalence charge transfer*). In $CaTiO_3:Pr^{3+}$ IVCT is accepted as the model that leads to the single red emission at room temperature, and emphasis is placed on this mechanism [24,27,28].

2.1.1.8. Intersystem crossing

This process is promoted by the crystal field depression of the 4f5d levels. When the Pr^{3+} ion is substituted into $CaTiO_3$, the corner sharing oxygen cages (TiO_6) tilt even further. This further distortion reduces the distance between the Pr^{3+} ion and the Ti^{4+} ions up to a point where they are close enough (< 3.16 Å) for Pr^{3+} ion orbitals to overlap directly with those of the Ti^{4+} ions. This direct metal – metal orbital overlapping induces charge transfer between the two ions, whenever there is an external source of energy (photon, heat, electron radiation, etc.). This leads to a bound exciton consisting of an electron shared amongst adjacent titanium neighbours [25,29].

$$Pr^{3+} / Ti^{4+} \rightarrow Pr^{4+} / Ti^{3+} \qquad \textbf{[2.2]}$$

This is the transfer of an electron from the Pr^{3+} ion to the Ti^{4+} ion, and thus brings about the reduction of Ti^{4+} ion to Ti^{3+} ion and the oxidation of Pr^{3+} ion to Pr^{4+} ion. This charge transfer mechanism is referred to as the *intervalence charge transfer* (IVCT: heteronuclear IVCT between two different cations and homonuclear between cations of the same element) as illustrated by Eq. 2.2. The IVCT brings about the IVCT state (fig. 2.6) that may be situated between 26 500 – 28 000 cm^{-1} within the forbidden region of $CaTiO_3$ matrix in between the $^1D_2$ and the ^3P_o states, and it provides an efficient quenching channel for the non – radiative depopulation of the ^3P_o state by a cross over to the $^1D_2$ because of the strong coupling that it has with the two meta– states. When sufficient energy is supplied to the IVCT by the host, then the crossover may be allowed [27,29,30,31,32].

$CaTiO_3:Pr^{3+}$ phosphor is a blue and red emitter, and at room temperature (~ 25 ^oC), the IVCT state is positioned at 26 700 cm^{-1}. At this position, the population of ^3P_o state may completely be depopulated by non-radiatively crossing over to the IVCT state and again non-radiatively cross over to the $^1D_2$ state and therefore increasing the population of the $^1D_2$ state and therefore leading to a single intense red emission from the $^1D_2 \rightarrow {}^3H_4$ transition. The resulting intense red colour from this transaction is marked by chromaticity coordinates of (0.68, 0.31), which are very close to the ideal red colour [25,30,32,36].

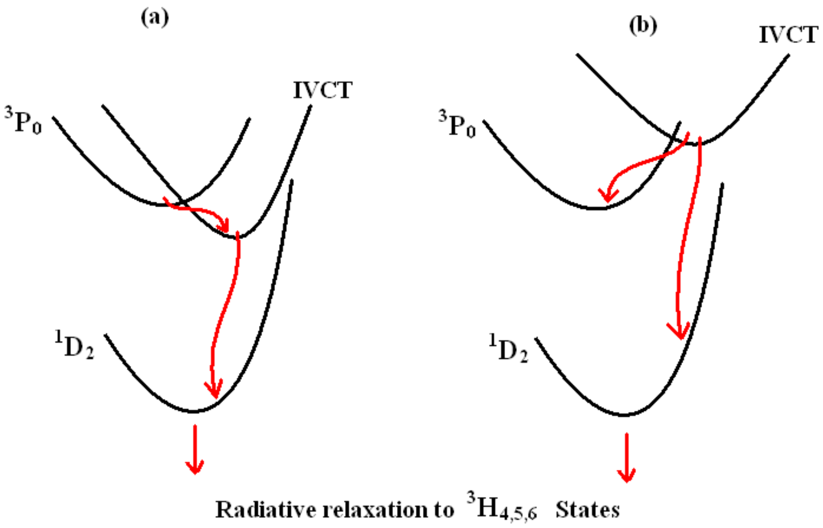

Figure 2.6: Configuration coordinate diagram showing the position of the IVCT at 27 ^oC (300 K) (a) and at -196 ^oC (77 K) (b)

At liquid Nitrogen temperature (-196 ^oC), the emission of the ^3P_o state is induced and it increases with an increase in concentration of the dopant ion. This happens because there is no thermal energy to assist with the promotion of ^3P_o state population crossover to the IVCT state. The expected red luminescence from the $^1D_2 \rightarrow {}^3H_4$ is poor because of the existence of more surface defects that act as quenching centres. In this case the IVCT state is positioned slightly above the $^1D_2$ state and it is not effective in depopulating the ^3P_o state. However as the concentration of the Pr^{3+} ions is increased, the IVCT state is positioned beyond the $^1D_2$ state, its population relaxes to ground state (valence band) via multiphonon relaxation. And when it positioned in this manner no luminescence is observed at all [25,30,32,36].

The position of the IVCT state is entirely dependent upon the distance between the Pr^{3+} and Ti^{4+} ions. When the distance between the two ions is very short, then less energy is required for the electron to move from one cation to the other. This then leads to a shallow positioned IVCT state and consequently poor depopulation of the ^3P_o state, and therefore a poor emission of the red light. This is another way to explain the existence of the blue emission at low temperature. The model for the IVCT position becomes extremely important for such cases [28,35,36].

2.1.1.9. The afterglow mechanism in $CaTiO_3:Pr^{3+}$

When a Pr^{3+} ion is introduced in the $CaTiO_3$ compound, it substitutes in the site of one of the Ca^{2+} ion sites. The Pr^{3+} and the Ti^{4+} ions give the compound an aggregate of 7+ valency, and this then brings an imbalance of charge in that site. This charge imbalance is compensated by generating intrinsic defects, such as negatively charged Ca^{2+} vacancies, and positively charged oxygen vacancies that promote afterglow. In principle, if two Pr^{3+} ions occupy two Ca^{2+} ions, they must generate one Ca^{2+} vacancy according to charge compensation. Therefore more Pr^{3+} ions doping, into the lattice brings about more Ca^{2+} vacancy formation that act as quenching centres because Pr^{3+} ions tend to transfer energy to them [18, 37].

The existence of oxygen vacancies create a local coulomb force that may attract and trap the electrons, which are then released upon introducing thermal energy in the material. The $^3H_4$ state on the other hand also acts as a hole (h^+) trap, and once it has trapped a hole it exists in Pr^{3+}/h^+ ionic complex (fig 2.7). The electrons in the oxygen traps and the holes trapped in $^3H_4$ attract one another and form a bound state (Exciton). As the temperature increases, the electrons in the oxygen trap acquire enough energy and excite to back to the $^1D_2$ state, and then finally relax by undergoing $^1D_2 \rightarrow {}^3H_4$ transition (fig 2.7), which results in the intense red light afterglow [25,37].

The afterglow emission is observed upon excitation with wavelengths shorter than or equal to 330 nm or equal to 360 nm, the electron-hole pairs are generated in the conduction and valence band of the matrix that can either be self trapped or trapped by defect centres, and therefore result the most intense afterglow. Whereas an irradiation with a source of wavelength that is equal to 360 nm, is directed to the IVCT band and this promotes electron transfer from the Pr^{3+} to Ti^{4+}. At very low temperature the oxygen vacancies trap more electrons and store them for a longer period than at higher temperature, and consequently a longer afterglow is expected from the $CaTiO_3:Pr^{3+}$ phosphor material [30,37].

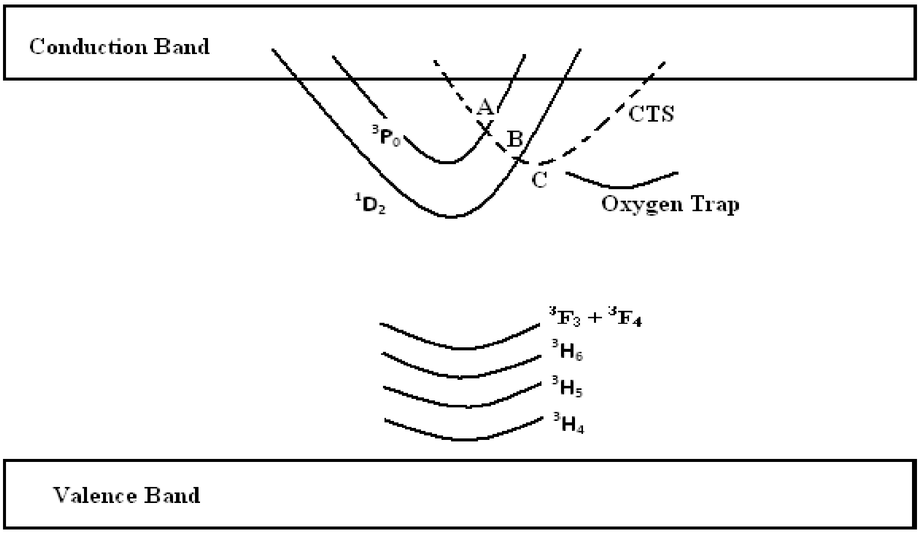

Figure 2.7: Luminescent mechanism of $CaTiO_3$ structure doped with Pr^{3+} ions

2.1.2. Ortho-tantalate phosphors

Phosphor compounds absorb radiation of certain energy and emit it in a different energy range as electromagnetic waves. Those which absorb X-rays and emit luminescence of electromagnetic waves at a different energy relative to that of X-rays are called x-ray phosphors, and the ortho-tantalate phosphors exhibit such characteristics. These compounds have been used for different applications, like dosimeters to measure radiation exposure in mining environments, during medical x-ray imaging procedures and optoelectronics. However these compounds are excessively used for radiation measurement applications. The mechanism from which the trapped radiation can be measured is associated with the trap levels within these compounds, which generate localized energy states in the forbidden region of their electron band structure. The stored radiation is revealed from these compounds by thermoluminescence measurements or by a microsecond pulsing laser [38,39].

X-ray phosphors like $YTaO_4$, $LaTaO_4$ and $GdTaO_4$ have been studied by activating them with rare-earth ions to yield emission coming from the host material luminescence centres and the activator luminescence centres. A flux agent is crucial for the formation of these compounds, and in its absence, the compound may not fully form. The role of the flux agent in this instant is to increase the reaction rate by acting as an intermediate that converts the reagents to reactive species, lower the reaction temperature required for the final compound to form and to facilitate crystallinity to control particle sizes. There are several flux agents that may be used in chemical reactions, and for $YTaO_4$, $LaTaO_4$, $GdTaO_4$, and Lithium sulphate has been used extensively [40,41,42,43].

$LaTaO_4$ is a perovskite compound, and on the contrary to $CaTiO_3$ compound that is an ABO_3 perovskite, $LaTaO_4$ has an ABO_4 stochiometry. An ABO_4 structure has BO_6 corner sharing octahedrons arranged in layers (fig. 2.8) that are not linked to each other like in the ABO_3 structure. In this instant the BO_6 octahedron is made of oxygen atoms that house the tantalum (Ta) ion. In between the BO_6 layers are the inner octahedron layers that house the lanthanum (La) ion [42,44].

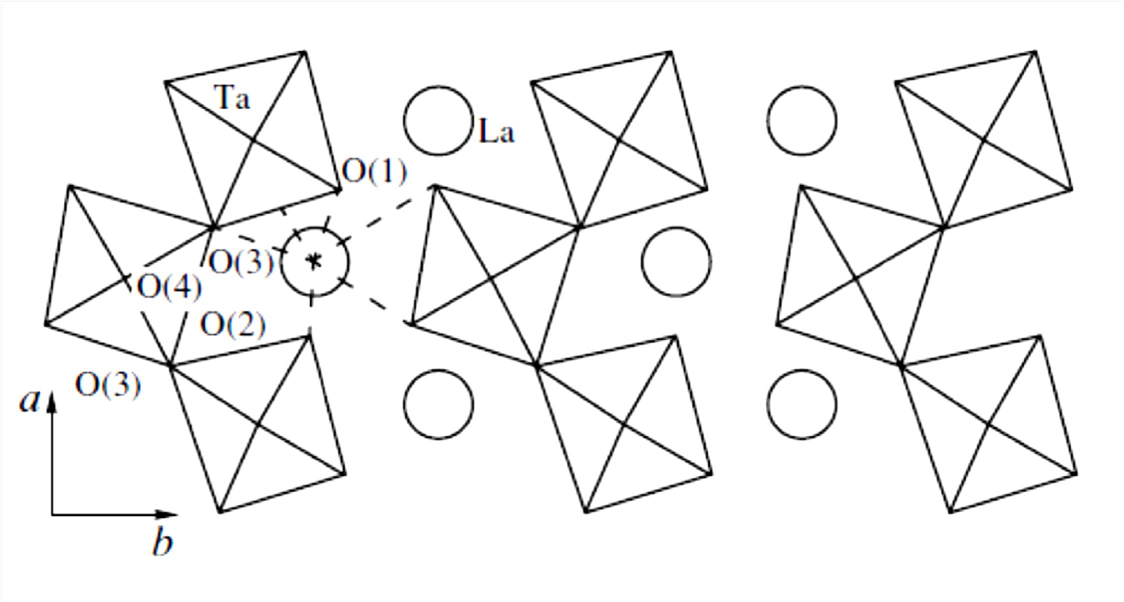

*Figure 2.8: LaTaO4 structure projected in a two dimensional plane **ab***

$YTaO_4$ and $GdTaO_4$ are fergusonite compounds, which are 0.5% distorted scheelites with ABO_4 stochiometry. A fergusonite can transform to scheelite or zircon structure under the influence of pressure or temperature, and a tantalate fergusonite structure changes under the influence of temperature. $YTaO_4$, and $GdTaO_4$ exist in three phases that are synthesis temperature dependent; A high temperature tetragonal phase (T – type) which is a scheelite and exists above 1450 ^{o}C, an intermediate phase that is monoclinic (M' –type) which exists below 1400 ^{o}C, and the low temperature monoclinic phase (M – type) that exists below 1000 ^{o}C. The excessively studied phases are the two monoclinic ones and the difference between the M and M' phases are in the Ta – O coordination. M' phase has 6 Ta – O coordination and M phase has 4 Ta – O coordination. The rare – earth (R → Y or Gd) ion has 8 R – O coordination. Fig. 2.9 shows an M' phase crystal structure of $YTaO_4$, and it is similar to that of $GdTaO_4$ M' phase [45,46,47,48,49,50].

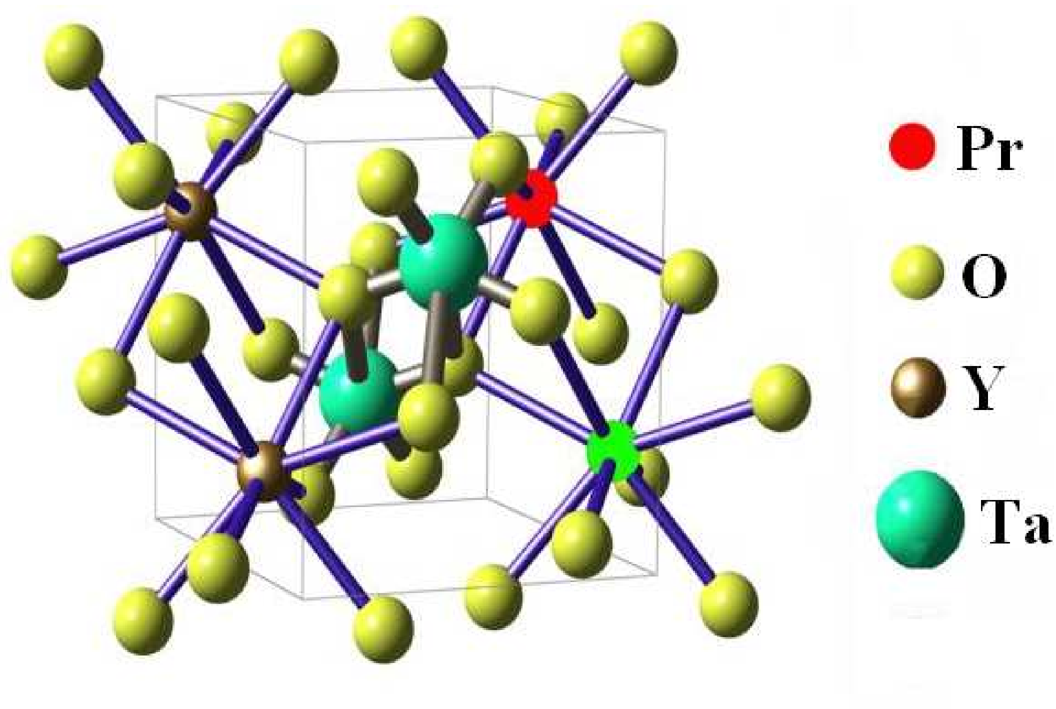

Figure 2.9: $YTaO_4$ crystal structure

2.1.3. Luminescence and trap centres in $(Y,La,Gd)TaO_4:Pr^{3+}$

Non doped $YTaO_4$, $LaTaO_4$ and $GdTaO_4$ compounds absorb x-rays in the region of 254 nm wavelengths, and re-emit the radiation in the ultraviolet-visible region (328 nm). This emission is attributed to defect levels as result of charge transfer absorption of the TaO_4 group. Upon doping the compound with a rare – earth ion that acts as an activator, the overall emission maybe attributed to both the host and activator luminescent centres. The distance between Ta – O coordination plays an important role in the emission of the compounds for both the activated and non activated host. The shorter the distance, the more efficient the charge-transfer absorption from the TaO_4 becomes. The distance is shorter for the M' phase than for the M phase, and this makes the M' a suitable phase for a phosphor with an efficient intensity. When Pr^{3+} is doped into $YTaO_4$, $LaTaO_4$ or $GdTaO_4$, it substitutes in the sites of Y, La or Gd ions [40,43,49].

Oxide compounds have many oxygen related defects that generate localized carrier trapping centres that are situated within the forbidden region of their band structure. The trap levels assume different depths within the forbidden region, and the shallow ones trap and transfer the carriers to the luminescent centre over time, and this process accounts for the persistent afterglow property in these compounds. The model in figure 2.10 limits the carriers to electrons for simplicity; the electrons excited to the conduction band relax to both the luminescence centre and the trap centre, and those trapped by shallow centres will be transferred to the luminescent centre [51].

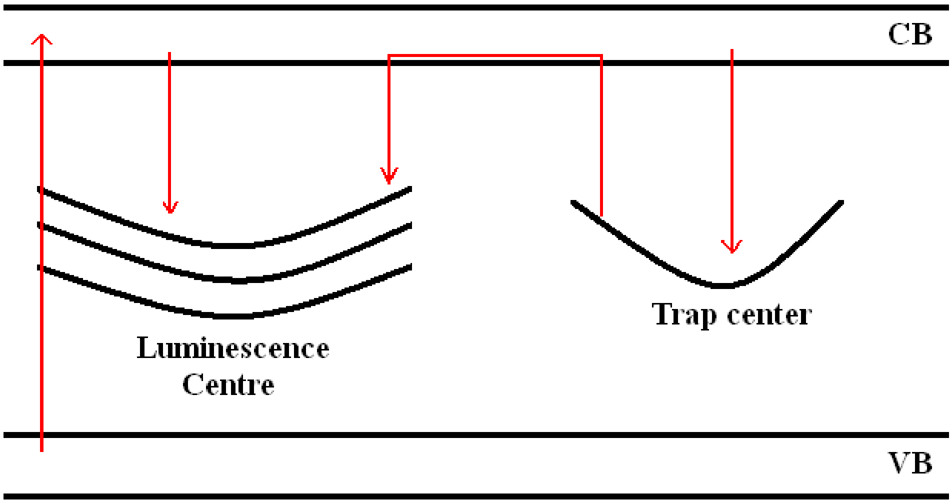

Figure 2.10: Phosphorescence mechanism

2.2. Synthesis method

In general matter is anything that occupies space and has mass, and it exists in different states, like; solids, liquids, gases and plasma, etc. Solids exhibit the most condense phase that is unified into a crystal structure that are often crowded by impurities. The molecular behaviour of these different phases of matter is different in that gases have molecules that randomly wander in space. When energy is removed from such molecules they condense to a liquid phase, and similarly liquids condense to solids when their energy is removed. Solids have their atoms closely packed into a rigid structure that may be a regular geometric lattice (*crystalline solid*) or an irregular geometric lattice (*amorphous solid*) [52].

Solid state reaction is the fabrication of solid materials either by direct transformation of a single solid material from one phase to another one through decomposition, or by directly mixing a solid material with other substances (*gases, liquids or other solids*) through ion interdiffusion to create multi component solid materials, at very high temperature. The solid state reaction may be prepared in the presence of the a fluxing agent that acts in facilitating crystal structure formation and also helps in achieving doping processes at very low temperature. The fluxing component has an additional ability of improving the surface morphology of the crystals. Solid state reactions are known to fabricate complete products of a single phase due their high temperature [53]. All four samples; $CaTiO_3:Pr^{3+}$, $LaTaO_4:Pr^{3+}$, $YTaO_4:Pr^{3+}$ and $GdTaO_4:Pr^{3+}$ were prepared by solid state chemical reaction at 1200 ^{o}C inside a furnace.

2.3. Reference

Text reference

[1] W. Tang, D. Chen, Mater. Research Bull. **44** (2009) 836

[2] X. Zhang, J. Zhang, X. Zhang, L. Chen, L. Yongshi, X.J. Wang, Chem. Phys. Lett. **434** (2007) 237

[3] A. Meldrum, L.A. Boatner, W.J. Weber, R.C. Ewing, J. Nucl. Mater. **300** (2002) 242

[4] B. Steele, A.D. Burns, A. Chernatynskiy, R.W. Grimes, S.R. Phillpot, J. Mater. Sci. **45** (2010) 168

[5] T. Wolfram & S. Ellialtioglu, ***Electronic and Optical properties of d-band perovskites***, 2006, Cambridge University press, USA, p3

[6] X. Zhang, J. Zhang, Xia Zhang, M. Wang, H. Zhao, S. Lu and X.J. Wang, **10** (2007) 1011

[7] A. Corgne, B.J. Wood, Contrib Mineal Petrol, **149** (2005) 85

[8] H.L. Wang, ***Structure and Dielectric properties of perovskite – Barium Titanate (BaTiO$_3$)***, 2002, [Thesis], San Jose State University

[9] Y.X. Wang, W.L. Zhong, C.L. Wang, P.L. Zhang, J. Solid Stat. Comm. **117** (2001) 461

[10] Y.X. Wang, W.L. Zhong, C.L. Wang, P.L. Zhang, Phys. Lett. A **291** (2001) 338

[11] H. Morawiec and D. Stroz, Applied crystallography: proceedings of the XIX conference, 2004, world Scientific publishing, London, p407

[12] V. Vashook, N. Trofimenko, M. Kuznecov, P. Otchik, J. Zosel, U. Guth, J. of Alloys and Compd. **419** (2006) 271

[13] M.T. Sebastian, ***Dielectric materials for wireless communication***, 2008, Oxford Press, UK, p 161

[14] S. Saha, T.P. Sinha, A. Mookerjee, Eur. Phys J. B **18** (2000) 207

[15] J.A. Souza, J.P. Rino, Phys. Rev. Lett. **40** (20), (1978) 1337

[16] L.S. Cavalcante, V.S. Marques, J.C. Sczancoski, M.T. Escote, M.R. Joya, J.A. Varela, M.R.M.C. Santos, P.S Pizani, E. Longo, J. chem. Eng. **143** (2008) 299

[17] K.T. Jacob, S. Gupta, Bull. Mater. Sci. **32** (6), (2009) 611

[18] P. Boutinaud, E. Pinel, M. Dubois, A.P. Vink, R. Mahiou, J. Lumin. **111** (2005) 69

[19] F.M. Pontes, C.D. Pinheiro, E. Longo, E.R. Leite, S.R. de Lazaro, J.A. Varela, P.S. Pizani, T.M. Boschi, F. Lanciotti, J. Mater. Chem. Phys. **78** (2002) 227

[20] M.L. Moreira, E.C. Paris, B.S. da Nascimento, V.M. Longo, J.R. Sambrano, V.R. Mastelaro, M.I.B. Bernardi, J. Andres, J.A.Varela, E. Longo, Acta. Mater. **57** (2009) 5174

[21] K. Ueda, H. Yangi, H. Hosono, H. Kawazoe, J. Phys.: Condens. Matter **11** (1999) 3535

[22] S. Kasap, P. Capper, ***Handbook of electronic and photonic Materials***, 2006, Springer, p983

[23] H.S. Sang, Y. J. Duk, W.P. Chang & S.Z. Dong, Jpn. J. Appl. Phys. **42** (2003) 3508

[24] E. Pinel, P. Boutinaud, R. Mahiou, J. Alloys Compd. **380** (2004) 225

[25] P. Boutinaud, L. Sarakha, E. Cavalli, M. Bettinelli, P. Dorenbos, R. Mahiou, J.Phys. D: J. Appl. Phys **42** (2009) 045106

[26] P. Boutinaud, E. Cavalli, M. Bettnelli, J. Phys.: Condens Matter **19** (2007) 386230

[27] P. Boutinaud, E. Pinel, M. Oubaha, R. Mahiou, E. Cavalli, M. Bettinelli, J. Opt. Mater. **28** (2006) 9

[28] P. Boutnaud, R. Mahiou, E. Cavalli, M. Bettinelli, Chem. Phys. Let. **418** (2006) 185

[29] V.K. Rai, J. Appl. Phys. B **95** (2009) 329

[30] P.J. Deren, R. Pazik, W. Strek, P. Boutinaud, R. Mahiou, J. Alloys Compd. **451** (2008) 595

[31] Y. V. Zorenko, J. Opt. Spectro. **88** (2004) 551

[32] C. Ghoerghies, P. Boutinaud, M. Loic, V.O. Atanasiu, J. Optoelectron. Advance. Mater. **11** (5), (2009) 583

[33] J.C. Kang, J.S.Choi, B.P. Seung, S.H. Cho, J.S. Yoo, J.D. Lee, J. Aerosol Sci. **28** (1), (1997) S541

[34] R. Fujiwara, H. Sano, M. Shimizu, M. Kuwabara, J. Lumin. **129** (2009) 231

[35] A.P. Vink, P. Dorenbos, C.W.E. van Eijk, J. Solid Stat. Chem. **171** (2003) 308

[36] P. Boutinaud, R. Mahiou, E. Cavalli, M. Bettinelli, J. Lumin. **122-123** (2007) 430

[37] W. Jia, D. Jia, T. Rodriguez, D.R. Evans, R.S. Meltzer, W.M. Yen, J. Lumin. **119-120** (2006) 13

[38] G. Liu, B. Jacquier (Eds.), ***Spectroscopic properties of rare earths in optical materials***, 2005, Springer

[39] A. Lakshmanan***, Luminescence and Display Phosphors: Phenomena and Applications***, 2008, Nova Science publishers

[40] E.J. Popovici, M. Nazarov, L. Muresan, Do Young Noh, E. Bica, M. Morar, I. Arellano, E. Indrea, Phys. Proc. **2** (2009) 185-190

[41] M. Gu, X. Xu, X. Liu, L Qiu & R. Zhang, J. Sol-gel Sci. Tech. 35 (2005) 193

[42] A.D. Salman, M.J. Hounslow***, Particle breakage,*** vol 12, 2007, Elsevier BV

[43] E.J. Popovici, M. Nazarov, L. Muresan, Do Young Noh, L.B. Tudoran, E. Bica, E. Indrea, J. Alloys Compd. **497** (2010) 201

[44] M.T. Dove, ***Structure and dynamics: an atomic view of materials***, 2003, Oxford university Press

[45] A. Grzechnik, K. Friese, V. Dmitrev, H.P. Weber, J.Y. Gesland and W.A. Crichton, J. Phys.: Condens. Matter **17** (2005) 763

[46] V. Panchal, N. Garg, A.K. Chauhan, S.M. Sharma, J. Sol. Stat. Comm. **130** (2004) 203

[47] A. Hristea, E.J. Popovici, L. Muresan, M. Stefan, R. Grecu, A. Johnsson, M. Boman, J. Alloys. Compd. **471** (2009) 524

[48] I.D. Arellano, M. Nazarov, D. Y. Noh, Revista Colombiana de Fisica, **41** (1), (2009)

[49] G. Blasse and A. Bril, J. Lumin. **3** (1970) 109

[50] M. Gu, X. Xu, X. Liu, L. Qiu and R. Zhang, J. Sol-gel Sci. Tech. **35** (2005) 193

[51] M.J. O'Brien and R.L. Lyman, ***Seriation, stratigraphy, and index fossils: the backbone of archaeological dating***, 2002, Kluwer Academic Publishers, New York, p25

[52] C.H. Bamford and C.H.Tipper, ***Comprehensive chemical kinetics,*** Vol 22, 1980, Elsevier Scientific publishers, New York, p41

[53] A.S. Wadhwa and H.S.Dhaliwal Er., ***A Texbook of Engineering Material and Metallurgy***, 2008, University Science press, India, p115

Figures

Figure 2.5 P. Boutinaud, E.Pinel, M. Dubois, A.P. Vink, R. Mahiou, J. Lumin. **111** (2005) 69

Figure 2.8 V.V. Molchanov, M.G. Zuer, S.V. Bogdanov, J. Inorganic Mater. **40** (1), (2004) 73

Figure 2.9 I.D. Arellano, M. Nazarov, D.Y. Noh, Revista Colombiana de Fisica, 41 (1), (2009)

3

Experimental characterization techniques

$CaTiO_3:Pr^{3+}$, $LaTaO_4:Pr^{3+}$, $YTaO_4:Pr^{3+}$ and $GdTaO_4:Pr^{3+}$ were prepared by solid state reaction, and their luminescence dynamics were probed using spectroscopic techniques to yield luminescence information. Several experimental techniques were used to achieve this goal, such as X-ray diffractometer, Scanning electron microscopy, Photoluminescence Spectroscopy, Thermoluminescence Spectroscopy, Cathodoluminescence Spectroscopy, DESY Synchrotron, Ultraviolet-visible absorption spectroscopy, Auger Electron Spectroscopy, X-ray photoelectron Spectroscopy. The aim of this chapter is to provide better understanding of these techniques.

3.1. X-ray Diffraction

X-ray diffraction (XRD – fig. 3.1) is an analytical technique primarily used for phase identification of crystalline compounds, and it can also be used to provide information on unit cell dimensions. X-ray diffraction is known as a common technique for the study of crystal structures and atomic spacing. Information provided by this technique is based on constructive interference of monochromatic X-rays that are generated within a cathode ray tube and a crystalline sample that is mounted on the sample holder. The waves of the x-rays incident to the crystal compound create an oscillating electric field that interacts with electrons of the compound atoms. The electrons coherently scatter the incoming electromagnetic radiation. Diffraction occurs when the atoms arranged in a periodic array scatter radiation at specific angles [1].

The X-rays that interact to produces constructive interference result in Bragg peaks observed on the spectrum. The incident angle of the X-rays is equal to that of the reflected rays. The relationship of the angle and wavelength of the diffracted X-rays in terms of reflection by the crystal planes is determined by Bragg’s law (Eq. 3.1) [2]:

$$n\lambda = 2dsin(\theta) \qquad [3.1]$$

where λ is the wavelength of the incident light rays, θ, the angle of incidence, and d being the interplanar spacing that sets the difference between the path and length for the rays scattered from the top plane and the rays scattered from the next plane parallel to the top one. The crystallographic planes that are used to define direction and distances in a crystal, are identified by Miller indices, and for a cubic crystal with a lattice parameter a_o, the interplanar distance can be labelled by Miller indices (***hkl***) and be represented by d_{hkl} (Eq. 3.2) [2]:

$$d_{hkl} = \frac{a_o}{\sqrt{h^2 + k^2 + l^2}} \qquad [3.2]$$

The sample that I used in XRD systems was a powder material of few grams, and it is often packed inside a sample holder that has a flat surface. When the X-rays that are of a single wavelength are directed onto the sample from the X-ray source, they become reflected by the crystallites. The reflection causes the single X-ray beam to split into several beams at different angles, relative to the sample surface. The instrument has a detector that swings around the sample, as the sample is rotated, and it registers the angle and the intensity of the beams. The registered data is then interpreted as a spectrum of intensity and angle of the X-rays called a diffraction pattern [3].

Phase identification comes out as the most desired property from the X-ray diffraction patterns of compounds including quantitative phase analysis to determine the relative amounts of phases in a mixture. Each pattern of the X-ray diffraction of some sample is expressed by a spectrum made of both the position and intensity of the Bragg peaks, where the position of the peaks is defined by the dimensions of the unit cells. The intensity of the peaks is derived from the distribution of atoms in the unit cell of every crystalline phase present in the sample, which is a fingerprint of each discrete compound. This enables identification of the crystalline phase present in some compound. This is possible because each compound has a unique diffraction pattern, and for mixed compounds the pattern is a combination of all individual patterns. Often the d – spacing of the planes leads to the identification by comparison with that from the ICCD (International Centre for Diffraction Data) [2,4].

Figure 3.1: The X-ray diffraction system: D8 Advnace Bruker

Heat treatment is necessary for luminescent materials to enhance crystallinity and often to remove derivatives of the reagents that are used to generate a particular compound. As it is mentioned earlier that heat treatment has an effect of inducing particle agglomeration and therefore result bigger crystallites. This effect can be clearly picked up by the XRD, in that bigger crystallites result sharp and narrow peaks, where as smaller crystallites result broader peaks. This is attributed to the lack of resolving power of very small particles. Often the absence of dopant ion peaks incorporation in the XRD spectrum may mean that they are evenly distributed within the matrix. The sizes of crystallites can be approximated from the Bragg peaks by Scherer's equation [3].

The first procedure in extracting information about the crystallite sizes from the Bragg peaks is to analytically fit one of the intense peaks, then extract the full width at half maximum (FWHM) from the fit curve. The peak width at FWHM is equal to $\boldsymbol{\beta_m}$. The corresponding width of the standard sample having a large crystallite size is then represented by $\boldsymbol{\beta_s}$. From Warren's equation the approximated width, $\boldsymbol{\beta}$, can then be estimated by equation 3.3:

$$\boldsymbol{\beta^2 = \beta_m^2 - \beta_s^2} \qquad [\mathbf{3.3}]$$

From Scherer's equation (Eq. 3.4) the $\boldsymbol{\beta}$ from Warren's relation is then used to approximate the size ($\boldsymbol{d}$) of the crystallites. $\boldsymbol{\theta}$ and $\boldsymbol{\lambda}$ are the incident angle and the wavelength of the X-rays incident onto the sample compound. In most cases $\boldsymbol{\beta m} \gg \boldsymbol{\beta s},$ and this leads to $\boldsymbol{\beta} \cong \boldsymbol{\beta_m}$.

$$\boldsymbol{d} = \frac{\mathbf{0.89}\boldsymbol{\lambda}}{\boldsymbol{\beta Cos(\theta)}} \qquad [\mathbf{3.4}]$$

X-ray diffraction is famous for the identification of unknown crystalline materials (e.g. minerals, inorganic compounds). Determination of unknown solids is critical to studies in geology for the identification of fine-grained minerals such as clays and mixed layer clays that are difficult to determine optically, studies in material science to determine the unit cell dimensions and investigate sizes of crystallites of some compound under analysis with the help of Scherer's equation, environmental science to measure sample purity. In addition, the XRD patterns can also be used to provide information on strain [5].

3.2. Scanning Electron Microscopy

Scanning electron microscopy (fig. 3.2) is a surface technique that is essentially designed to capture images of three dimensional objects on specimen surfaces. A typical instrument is equipped with an electron gun, secondary electrons detector, BS detector, and a specimen holder. All these are housed within a vacuum chamber. Secondary and backscattered electrons that emerge from the specimen surface when it is probed by primary electrons from the electron gun within the system are employed to produce specimen images. Secondary electrons images are used to extract topographic contrast, and backscattered electron images are used to extract compositional differences on the surface [6]. This technique can operate in conjunction with EDS (energy dispersive spectroscopy) or WDS (wavelength dispersive spectroscopy) for mapping and elemental composition analysis [6,7].

Figure 3.2: Shimadzu SSX -550 SEM

3.3. Photoluminescence Spectroscopy and Synchrotron

Photoluminescence is a resulting optical transition when a material (e.g. phosphor) absorbs electromagnetic waves (light) of sufficient energy to excite electrons from the valence band to the conduction band and leaving behind holes, and in return generate electromagnetic waves when the carriers recombine. An instrument used to characterize such properties is referred to as photoluminescence (PL) spectroscopy. Such a system can be achieved using a laser, a xenon lamp or synchrotron radiation to generate the electron hole pairs in the electron structure of a sample, and the light from the source is focused to the sample using lenses. The output of the detected emission is displayed as PL intensity as a function of the emitted light wavelength. The instrument can be used to carry out investigations of phosphor emission wavelengths, emission intensity optimization and luminescent changes upon co-doping an activated phosphor with a sensitizer ion. Most advanced PL spectroscopy techniques can be used to measure photoluminescence, photoluminescence excitation centres and phosphorescent lifetimes. Amongst such techniques is the Varian-Carry Eclipse system (fig. 3.3), which uses a xenon lamp as a source of excitation [8,9].

Figure 3.3: Varian Carry-Eclipse fluorescent spectroscopy

A synchrotron radiation is on the other hand different compared to the other sources. It gives a very intense beam almost like a laser, however not with a fixed wavelength, but over a broad spectrum from X-rays, ultraviolet, visible, to infrared electromagnetic waves. A synchrotron (fig. 3.4) is a particle accelerator that accelerates a charge in a cyclic path in which the electric field is used to accelerate the particle and the magnetic field used to bend particle. The circumference of the cyclic path can be different in meters depending on the size of the synchrotron laboratory [10].

The process begins when an electron gun generates electrons and ejects them into the linear accelerator where they are accelerated to a third of the speed of light by an electric field. These electrons will then be moved to the booster ring with 289 m circumference for a DESY (Deutsch Electron Synchrotron), where they are accelerated to about 91 % of the speed of light using pulsed electric field. When 91% is reached, then the particle is passed to a storage ring of 2304 m circumference. Inside the storage ring the particle is introduced to a stronger magnetic field and pulsing electric field. This ring will accelerate the particle to 99 % of the speed of light. At this speed, when the magnetic field bends the electrons, it forces them to lose energy in the form of electromagnetic waves called synchrotron radiation. The resulting beam of light is directed to beamline channels that may be of different lengths and the end of these channels, sample characterization is performed [10].

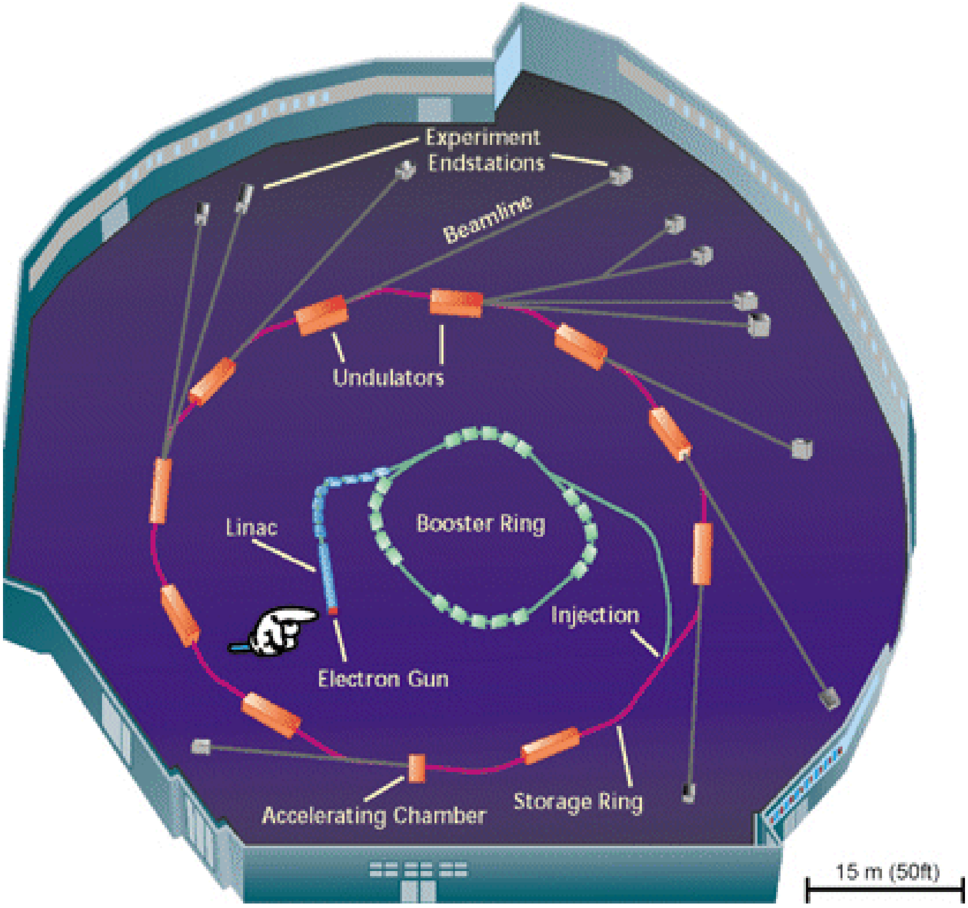

Figure 3.4: Schematic representation of a synchrotron facility

3.4. Thermoluminescence Spectroscopy

It is a natural ability of materials fabricated at high temperature, especially the oxides to have defects in their lattice structure. These defects generate localized energy levels positioned within the forbidden band gap of a material and they act as traps of both the holes and electrons upon excitation (fig. 3.5). These electron traps are often generated by oxygen vacancies, which may assume different orientations and thus positioned at different depths. When the material is heated after the material had been radiated, the trapped carriers will accumulate sufficient energy to jump out of the trap sites. These released carriers will then be attracted by the luminescent centre [11,12].

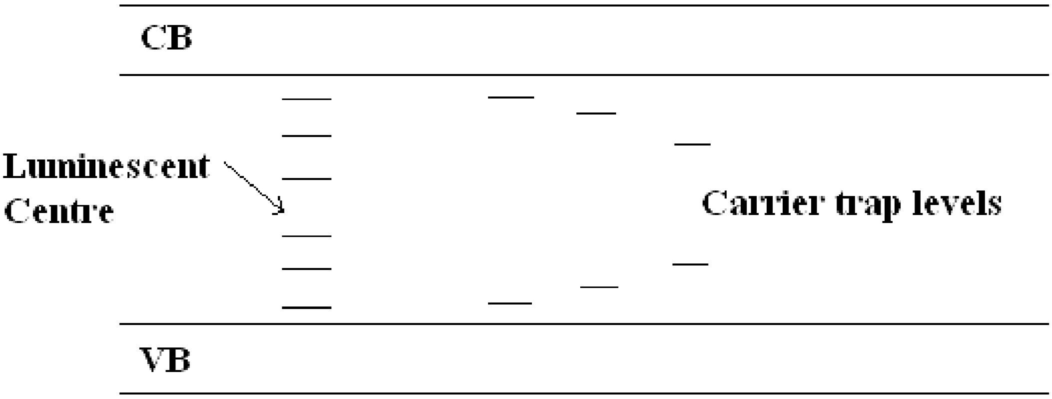

Figure 3.5: Mechanism behind thermoluminescence

The resulting luminescence is used to approximate the depth of the trap levels within the forbidden region, and a thermoluminescence spectroscopy (fig. 3.6) is used to reveal such information. Such information is extracted from the glow curve which is the resulting thermoluminescence emission as function of temperature. The traps in the system may even be isolated from each other and positioned at different depths, and the carries trapped in deeper trap sites require higher thermal energy [11,12].

Figure 3.6: TL 10091, NUCLEONIX spectrometer

Thermoluminescence spectroscopy is used in various fields of study which include radiation dating of rocks, which is an archaeological method of determining the age of rocks based on the stored radiation within the trap levels of a material. The released thermoluminesce glow that comes from materials with naturally occurring radioactive isotopes is then correlated to the age of a rock. The archaeological age is then calculated by working out the quotient of the adsorbed radiation at the time of measurement over the total radiation dose material is able to absorb per year [11,12].

3.5. Ultraviolet-Visible absorption spectroscopy

When light is projected towards a solid material, the light waves are reflected, absorbed or transmitted. If the waves are incident on a flat metallic material, they are specular (fig. 3.7) reflected backwards upon arrival at the surface. Non – metallic materials may at once absorb and reflect or absorb, reflect and transmit the incoming waves. The latter applies to materials that are sufficiently transparent to allow a certain portion of the light waves to pass through their structure.

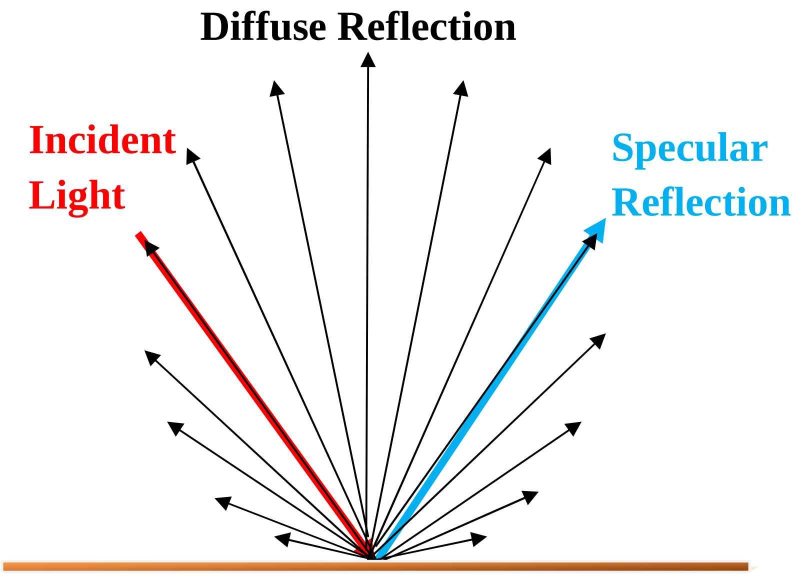

Figure 3.7: Incident light reflection on the surface on a solid material

The ability of materials to absorb and reflect is an important parameter that is used by the UV/Vis spectroscopy to identify how phosphor materials respond to light radiation. Light reflection by solids occurs in several ways. However of importance in the context is diffuse reflectance (fig. 3.7), which occurs when light is projected onto rough surfaces like that of powder materials [13,14].

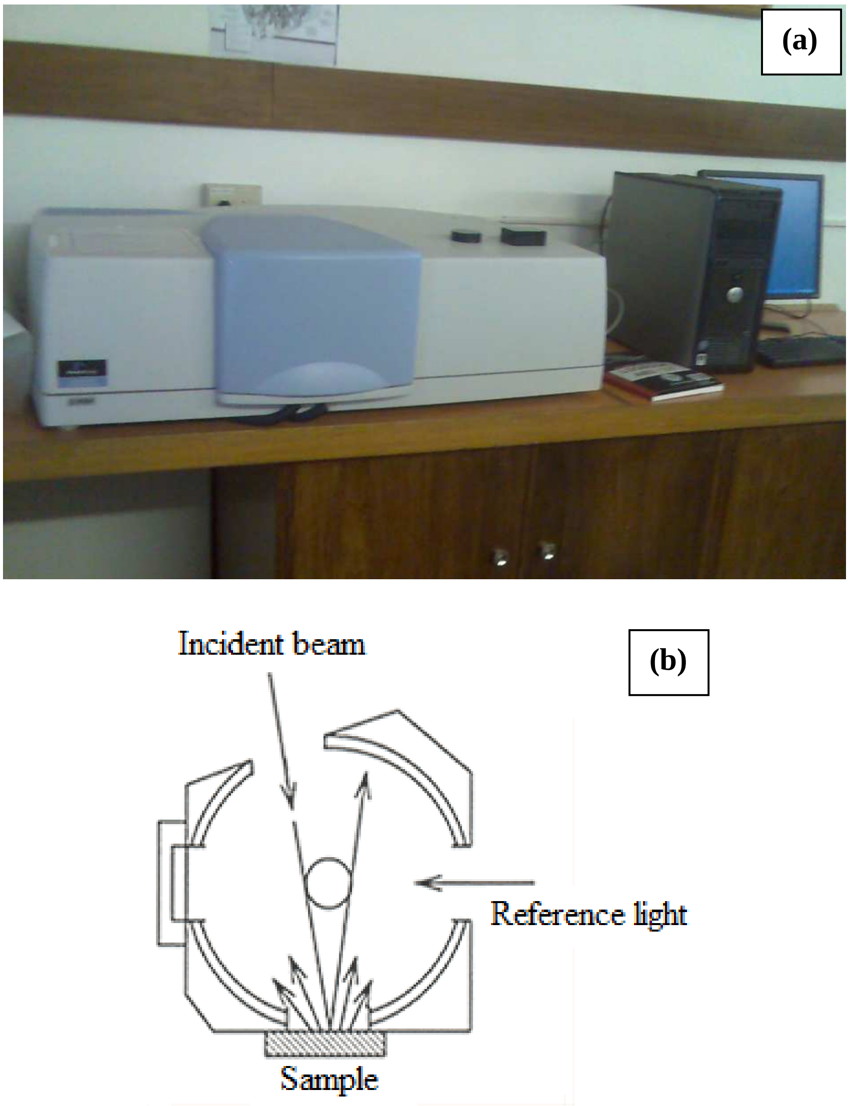

Figure 3.8: (a) UV/Vis spectroscopy at University of Free State, Physics Department and (b) Schematic of the integrating sphere interior

The UV/Visible spectroscopy (figure 3.8a) is equipped with two source lamps: Deuterium (from about 10 nm to 330 nm) and Tungsten lamps (300 nm to wavelength greater than 3000 nm). The lamps are used to irradiate the sample, with the Deuterium used from 200 nm up to 319 and then shift to Tungsten up to 1000 nm. Upon irradiating the sample, the source beam is split into two beams. One beam is directed to the sample and the other is sent to the detector as a reference. The sample is positioned inside an integrating sphere (figure 3.8b) that collects the diffusely scattered light by the sample. Some of the incident light is absorbed by the sample. The collected light eventually falls onto the detector, which subtracts the collected light from the source light to determine the amount that has been absorbed. The detectors used in this system are the PbS and PMT measuring the near infrared region, and Ultraviolet and visible region, respectively. This technique allows determination of the absorbance characteristics of phosphor materials [15].

3.6. Cathodoluminescence and Auger Electron Spectroscopy

Cathodoluminescence (CL) measurements are done *in-situ* by probing the sample with an electron beam in a vacuum chamber of 1×10^{-6} Torr O_2 pressure and below. Auger electron spectroscopy (AES) sytem is used to probe the surface with an electron beam, and an optical fibre is attached to the system is used to collect the emitted photons and transmits them to the CL spectrometer. AES PHI 549 and Ocean Optics Inc. PC2000 (fig. 3.9) were used to carry out CL degradation under a prolonged electron beam irradiation.

Figure 3.9: AES PHI 549

AES is an analytical technique used specifically in the study of surfaces, especially in the material science field. AES makes use of the Auger effect (fig. 3.10) to yield elemental information on the surface of the specimen. I used an electron beam of 2 keV energy to ionize the atoms residing on the surface of the phosphor material. An electron from an inner energy level (i.e. energy level E_2 from figure 3.10) is ejected, leaving behind a vacancy. Then an electron from E_1 may jump to E_2 to fill the vacancy [16].

As the outer level electron jumps to the inner shell, energy is liberated and may generate an x-ray photon, or used to excite another electron in E_1 or E_3 [16,17]. The electron that may be ejected from E_3 or E_1 is called an Auger electron, and carries energy that gives out the characteristics of the element of the atoms on the surface of the specimen [18].

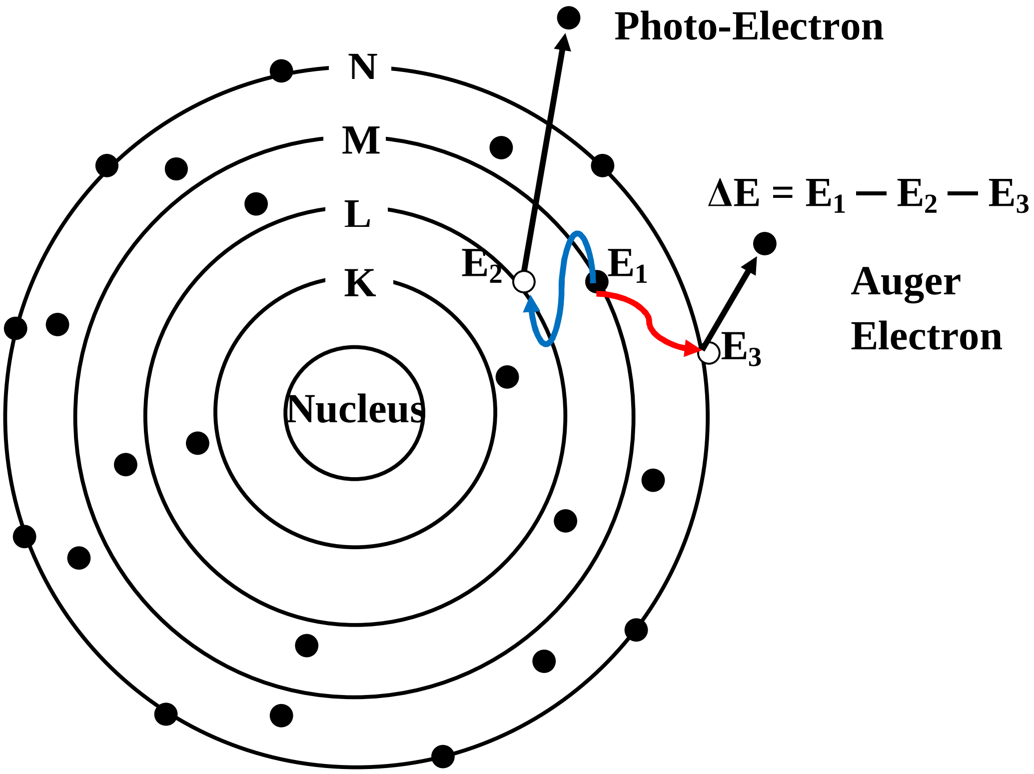

Figure 3.10: Auger mechanism

The probability that the secondary particle emitted from the specimen is an x-ray or an auger electron is dependent on the binding energy of the atom that is on the specimen surface. The emission of an auger electron is favoured by energy levels of lower binding energies (i.e. atoms of lower atomic number) compared to the emission of x-rays [18,19].

AES is highly surface sensitive in that it analyzes approximately from 1 to 5 nm depths, and its lateral resolution depends on the nature of the electron being used. It is sensitive to all elements except hydrogen and helium with detection limits of 0.1-1% atomic or 0.1 monolayers. Hygrogen has 1 electron and Helium 2 electron, thus their electrons are not sufficient for the auger effect. This explains why AES cannot detect hydrogen and Helium [20].

3.7. X-ray photoelectron spectroscopy

In the vacuum chamber of an AES, there exists gases and amongst them are O_2 and H_2O. The electron beam is known to dissociate the surface of the sample and the gases that it interacts with, into atomic species that may adsorb onto the surface of the specimen. According the electron stimulated surface chemical reaction (ESSCR) mechanism, electron beam dissociation of the surface of the specimen and adsorption of O^- atomic species may lead to surface oxidation. The nature of the resulting oxide compound may be traced using X-ray photoelectron spectroscopy (XPS) [21]. XPS PHI 5000 versa probe using 100 μm, 25 W and 15 kV Al monochromatic x-ray beam (fig. 3.11) was used to analyze the degraded samples.

Figure 3.11: PHI 5000 versa-probe XPS

XPS aims at characterizing elemental composition, chemical state and the electronic state of the elements on the specimen surface. According to figure 3.12, the specimen surface atoms are ionized by an irradiation of Aluminium or Magnesium X-rays. Simultaneously XPS measures the kinetic energy (KE) and number of electrons that escape from 1 to 10 nm of the material surface being analyzed. The energy carried by a particular wavelength is equal to a known, and the electron binding energy (BE) of emitted electrons can be measured using an equation (Eq. 3.5) [19][22].

$$E_{binding} = E_{photon} - E_{kinetic} - \text{Ø} \qquad \textbf{[3.5]}$$

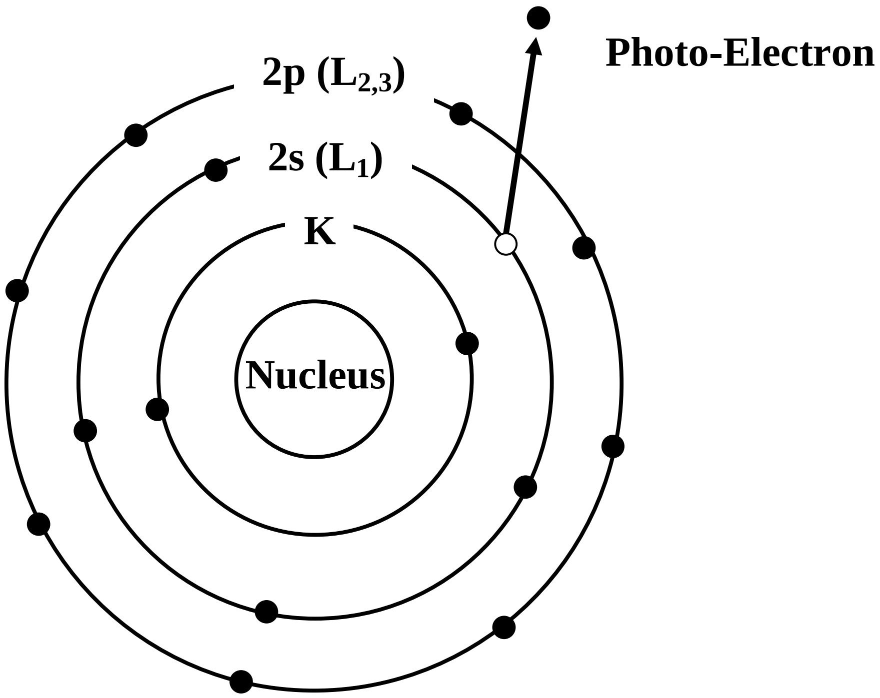

Figure 3.12: Mechanism behind the operation of XPS

where the binding energy is that of an electron emitted by electron configuration within the atom, the photon energy being that of the X-ray used, kinetic energy is that of the photoelectron and Ø is the work function of the detector [22]. The binding energy of each atom is unique; hence the energy peaks of different atoms have different energy positions.

XPS earned its popularity by its ability of chemical analysis, and like AES it cannot detect H_2 and He because their electrons come from the valence band. This causes them not to have unique energy peaks [19,23].

3.8. Reference

[1] M.A. Prelas, G. Popouci, L.K. Bigelow, ***Handbook of industrial diamonds and diamond films***, 1998, CRC Press

[2] E.H. Kisi C.J. Howard, ***Applications of Neutron diffraction***, 2008, Oxford university press, New York

[3] H. Lipson and H. Steeple, ***Interpretation of x-ray powder diffraction patterns***, 1970, MacMillan, London

[4] V.K. Perchasky and P.Y. Zavalij, ***Fundamentals of powder diffraction and structural characterization of materials***, 2nd Ed., 2009, Springer

[5] D.M. Moore, R.C. Reynolds (Jr.), ***X-ray diffraction and the identification and analysis of clay minerals***, 1989, Oxford Press, New York

[6] S.J.B. Reed, ***Electron Microprobe analysis and scanning electron microscopy in geology***, 2005, 2nd edition, Cambridge Press, New York

[7] J.I. Goldstein, H. Yakowits, ***Practical Scanning Electron Microscopy; Electron and Ion Microprobe Analysis***, 1977, Plenum Press, London

[8] A.M. Fox, ***Optical properties of solids***, 2nd Ed., 2010, Oxford University Press, New York, p120

[9] G.V. Bordo, H.G. Rubahn, ***Optics and spectroscopy at surfaces and interfaces***, 2005, Wiley-VCH, p120

[10] A.V. Bordovitsyn, I.M. Ternov ***Synchrotron radiation theory and its development: in memory of I.M. Ternov,*** 1999, World Scientific publishing

[11] M.J. O'Brien, R.L. Lyman, ***Seriation, stratigraphy, and index fossils: the backbone of archaeological dating***, 2002, Kluwer Academic Publishers, New York

[12] J. Mike, C. Walker, ***Quaternary dating methods***, 2005, John Wiley and sons, England

[13] D.R. Stille, ***Manipulating light: reflection, refraction, and absorption***, 2006, Compass Point Books, USA

[14] W. A. Wooster, ***Diffuse X-ray reflection from crystals***, 1997, Dover Publications, Inc. USA

[15] R.J. Anderson, D.J. Bendell, P.W. Groundwater, *Organic spectroscopic analysis,*2004, The royal society of chemistry, Great Britain

[16] J.C. Tracy, ***Electron Emission Spectroscopy***, 1972, Edited by W. Dekeyser, L. Fiermans, G. Vanderkelen *et al;*D Reidel publishers, Dordrecht –Holland

[17] E.B. Podgoršak, ***Radiation Physics for Medical Physicists***, *2006*, Birkhäuser publishers, Switzerland, p91

[18] J.M. Walls, ***Methods of Surface Analysis***, 1989, Cambridge University Press.

[19] D. Briggs and M.P. Seah, ***Practical Surface Analysis by Auger and X-ray Photoelectron Spectroscopy***, 1993, John Wiley & Sons Ltd

[20] C.J. Vickerman**,** ***Surface analysis: the principal techniques***; 1997, Wiley and sons Inc; England

[21] H.C. Swart, J.S. Sebastian, T.A. Trottier, S.L. Jones and P.H. Holloway, J. Vac. Sci. Technol. **14** (3), (1996) 169

[22] C.D. Wagner, W.D. Riggs, L.E. Davis, *et al*, ***Handbook of X-ray Photoelectron Spectroscopy*** Perkin-Elmer Corp., 1979, Eden Prairie, MN, USA

[23] N.M.K. Lamba, A.K. Woodhouse, S.L. Cooper, ***Polyurethanes in Biomedical Applications***, 1997, CRC Press, p101

4

In^{3+} Charge Compensation in CaTiO$_3$:Pr^{3+}

4.1. Introduction

Phosphorescent materials have drawn attention for applications in medical imaging, warning signs, soft illumination and several other applications. The oxide materials have an ability to generate many positively charged oxygen vacancies within their lattices, which reside within the forbidden region of the band structure. These oxygen vacancies are the major contributors to the phosphorescence behaviour of phosphors. The praseodymium doped red emitting calcium titanate ($CaTiO_3:Pr^{3+}$) phosphor has colour coordinates ($x = 0.68$, $y = 0.31$) close to those of ideal red light. The orthorhombic perovskite $CaTiO_3:Pr^{3+}$ is a phosphorescent phosphor, as a result of the oxygen vacancies that arise when the trivalent Pr^{3+} ions are substituted in the site of the divalent Ca^{2+} ions. These vacancies are attributed to self compensation of the material, and they have the ability to attract negative carriers, which they release back to the luminescent centres of Pr^{3+} after a certain period. The phosphorescence mechanism of $CaTiO_3:Pr^{3+}$ is based on charge compensation, trapping and detrapping of charge carriers [1,2,3,4,5].

The single red emission peak around 613 nm is attributed to the intervalence charge transfer (IVCT), which lies below the $^3P_0$ level at room temperature (figure 4.1a). In this position, IVCT completely depopulates the $^3P_0$ level non-radiatively by crossing it over to the $^1D_2$ level. The population then de-excites radiatively to the $^3H_4$ level. At low temperature close to liquid nitrogen temperature, the IVCT is above both the $^3P_0$ and $^1D_2$ levels, making it possible to get blue and red emission from Pr^{3+}. Enhancement of $CaTiO_3:Pr^{3+}$ emission intensity has been achieved by incorporating Al^{3+}, Bi^{3+}, B^{3+} and Lu^{3+} metal cations as charge compensators. The phosphor can be prepared using different synthetic methods like solid state, sol-gel, peroxide-base route and combustion. Many phosphors, having a mismatch in the valency which results in

Noto et al, SAIP’ 2011 Proceedings, p254
Noto et al, J. Alloys Compd. *Submitted December 2011*

defect formation and act as a deterrent in the case of emission, are traditionally synthesized using charge compensatory additives [1,2,6,7,8,9,10]. Although Zn^{2+} and/or Mg^{2+} doping were found to be quite effective in increasing both the fluorescence and phosphorescence of $CaTiO_3:Pr^{3+}$ they can only be used in preparing red phosphorescent/persistent phosphors and not fluorescent phosphors needed for display application [11]. This chapter aims to address the goal of emission enhancement, by adding In^{3+} ions as co-dopants to charge compensate the additional positive charge of Pr^{3+} ions. This was achieved when In^{3+} ions were substituted in the site of Ti^{4+} ions to suppress or improve the afterglow, making it possible for this material to be used either as a fluorescent or phosphorescent phosphor.

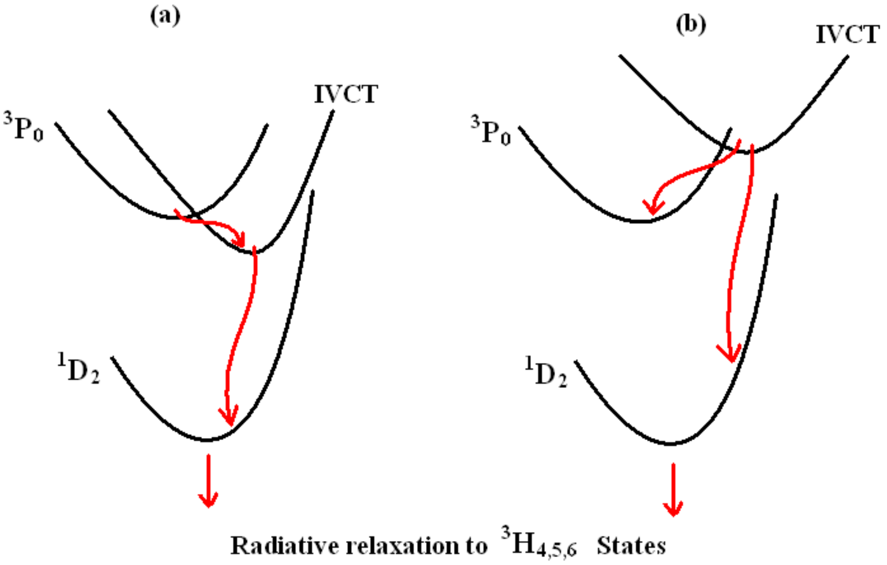

Figure 4.1: IVCT model for the depopulation of the $^3P_0$ *level.*

4.2. Experimental

$Ca_{1-x}TiO_3:xPr^{3+}$ (x = 0.1, 0.2, 0.3, 0.4, 0.5), and $Ca_{0.8}Ti_{1-y}O_3:0.2Pr^{3+},yIn^{3+}$ (y = 0.05, 0.1, 0.2, 0.3) phosphors were prepared by solid state reaction method. The objective was to obtain the optimum concentrations of Pr^{3+} and In^{3+} that will in turn optimize the PL intensity and charge compensation. The phosphors were prepared by stochiometrically mixing (1 – x)$CaCO_3$, (1-y) TiO_2(Anatase phase), x$PrCl_3$, and y$In(NO_3)_3$ into a slurry mixture, and dried at 150 °C for 10h.

The mixture was preheated and then fired at 1200 ^{o}C for 4h and the resulting compounds were ground into fine powders.

The PL spectra were measured using the Varian Carry-Eclipse fluorescence spectrometer for photoluminescence excitation (PLE) and emission (PL) characteristics. Phosphorescence lifetime measurements and defect quantifications and depth approximation were achieved using thermoluminescence TL 10091, Nucleonix spectrometer. The phosphorescence measurements were carried out by pumping carriers to the luminescent centres using 50 xenon lamp flashes, with 100 ms delay between the flashes. A PerkinElmer Lambda 950 UV/VIS spectrometer was used to record the diffuse reflectance spectra. The phase and surface morphology were identified using a Bruker AXS D8 Advance X-ray diffractometer (XRD) and Scanning electron microscopy (SEM) (Shimadzu SSX-550, Kyoto, Japan), respectively.

4.3. Results and Discussion

The XRD patterns of the $CaTiO_3$:0.002Pr^{3+} with different concentrations of In^{3+} (figure 4.2) match that of the standard orthorhombic $CaTiO_3$ (JCPDS card no. 22-0153). The patterns suggest that there were no effects from the Pr^{3+} and In^{3+} ions. The surface morphology shows agglomerated particles with different shapes and sizes. The particle sizes were estimated to be approximately 0.6 μm, using the diffraction peaks and Scherrer's equation (Eq 4.1)[12]:

$$\boldsymbol{s = \frac{k\lambda}{\beta\, cos\theta}} \qquad [\mathbf{4.1}]$$

where $\boldsymbol{s}$ is the average size of $CaTiO_3$ particle, $\boldsymbol{\beta}$ is the full-width-at-half-maximum of the diffraction at angle $\boldsymbol{\theta}$, $\boldsymbol{k}$ is the shape factor that is approximately 0.89 and $\boldsymbol{\lambda}$ is the wavelength of the X-rays (1.54 Å) used to characterise the compounds [12].

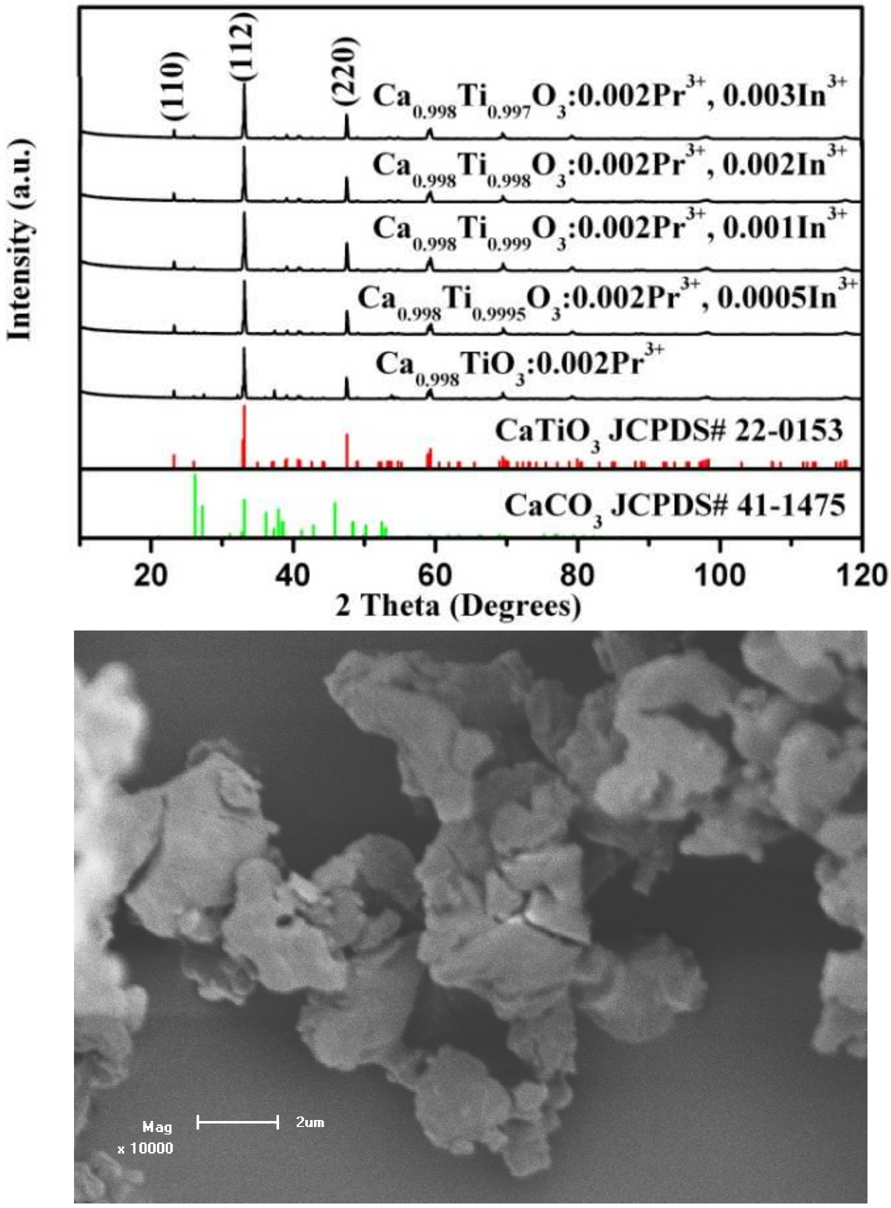

Figure 4.2: XRD patterns of $Ca_{0.8}TiO_3:0.2Pr^{3+}$ *with different* In^{3+} *concentrations and SEM image captured at 2 μm magnification.*

Figure 4.3a shows the PL emission spectra of $CaTiO_3$ doped with different concentrations of Pr^{3+} ions, that was captured with a medium photon multiplier tube (PMT) voltage. At room temperature, the single red emission of Pr^{3+} around 613 nm is attributed to the IVCT complete quenching of the blue emission of the $^3P_0$ level by promoting the red emission of the $^1D_2$ level. Figure 3b shows the corresponding PL intensity variation with Pr^{3+} concentration.

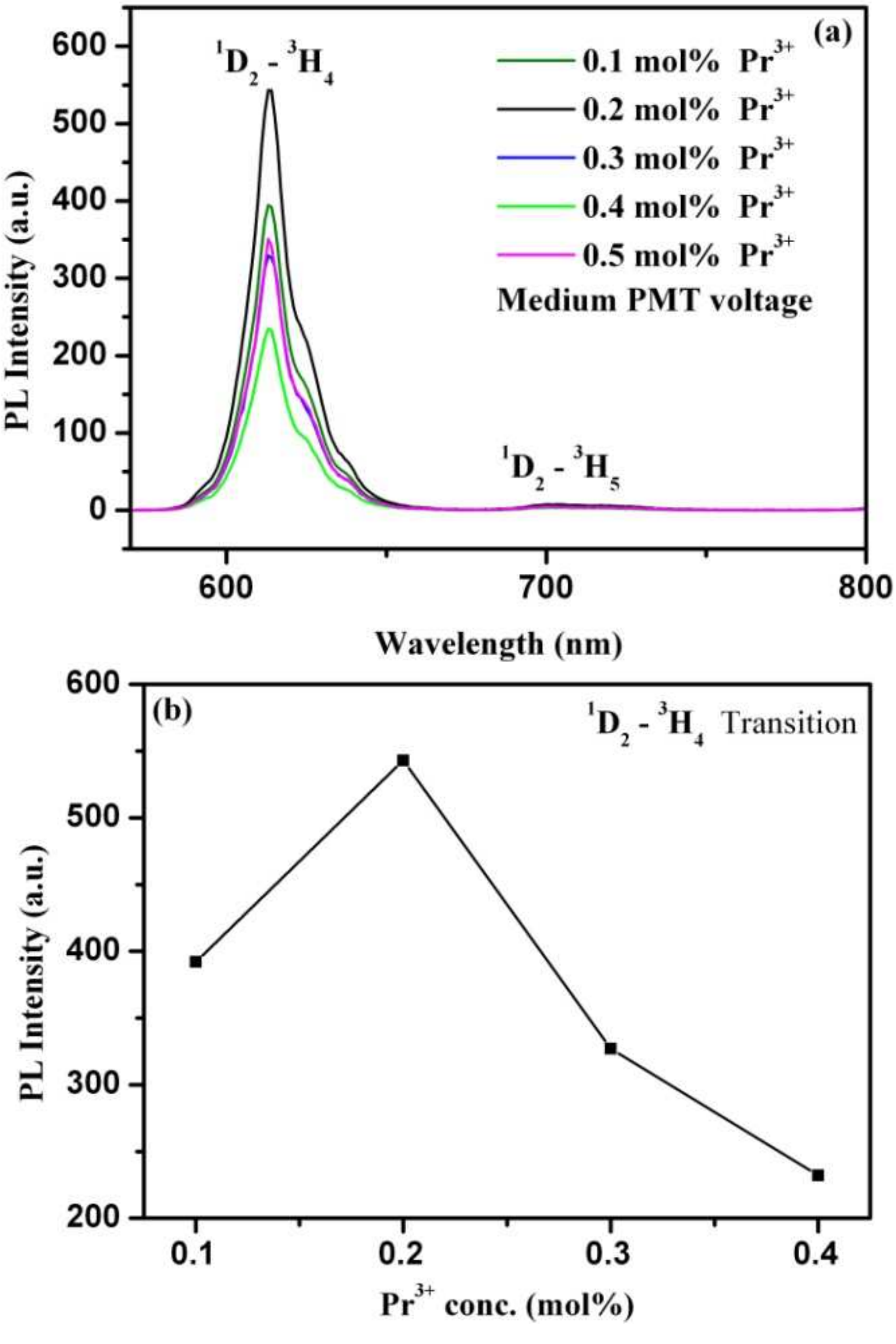

Figure 4.3. (a) PL spectra of $CaTiO_3:xPr^{3+}$ (b) PL intensity as a function of Pr^{3+} concentration.

The PL intensity increases from 0.1 to 0.2 mol%, then decreases from 0.3 to 0.4 mol% doping. The increase in the PL intensity from 0.1 to 0.2 mol% is a result of increased luminescent centres of Pr^{3+} with increasing Pr^{3+} concentration. However, at Pr^{3+} concentrations higher than 0.2 mol% the luminescence emission was quenched because of reduced distance between Pr^{3+} centres. That is, when Pr^{3+} centres are close enough to each other, their ability to trap carriers is increased, which later de-excite non-radiatively because of phonon interaction [3,6].

From the diffused reflectance spectra of $CaTiO_3$:0.2Pr^{3+},yIn^{3+} (figure 4.4), upon excitation of the system, the major absorption comes through electron transition from 2p(O) state to the 3d (Ti) states which are excitable by a wavelength that is approximately 330 nm. Lower wavelength excitation will promote electrons from the 4f level to the 4d5d level of Pr^{3+}. 4f – 4f ($^3H_4 \rightarrow {}^3P_0$, $^1I_6$, $^3P_1$, $^3P_2$) absorption of Pr^{3+} is also triggered upon exciting the material with a wavelength around 430 nm to 500 nm. The $^3H_4 \rightarrow {}^3P_0$ absorption is not that much prominent upon 613 nm excitation [1,2].

PL excitation (λ_{em} = 613 nm) and emission (λ_{ex} = 300 nm) spectra of $CaTiO_3$:0.2 Pr^{3+} doped with different In^{3+} concentrations are presented in figure 4.5a, and the data were captured using low PMT voltage at room temperature. In^{3+} co-doping has no effect on the position of the IVCT, and hence no additional contribution of the blue emission is observed from $^1D_2 \rightarrow {}^3H_4$ transition of Pr^{3+} luminescent centres.

The excitation spectra is formed by 3 broad bands, one situated around 250-270 nm from the 4f→4f5d absorption of Pr^{3+} ions, and the other one around 300 – 320 nm, which is attributed to the absorption edge of $CaTiO_3$ (2p (O) → 3d (Ti))[1,3]. The one at around 360 nm is assigned to a low-lying Pr to-metal (Pr^{3+} –Ti^{4+}) intervalence charge transfer state. The Absorption edge band (marked with an asterisk in figure 4.5a) shifts from lower wavelength to higher wavelengths as the intensity increases as result of the change in the electronic structure.

Figure 4.5c&d extend more on the excitation band positions by deconvoluted version of the spectra in figure 5a. The peaks from the deconvolution correspond to those obtained from the diffuse reflectance spectra as in the above paragraph. According to Bautinaud et al [1] and S. Tin et al [4], the absorption band shifts are a result of the change in the band structure of the material which may be introduced by small phase changes. The forbidden region of $CaTiO_3$: $0.2Pr^{3+}$, $0.1In^{3+}$ is the smallest in this situation.

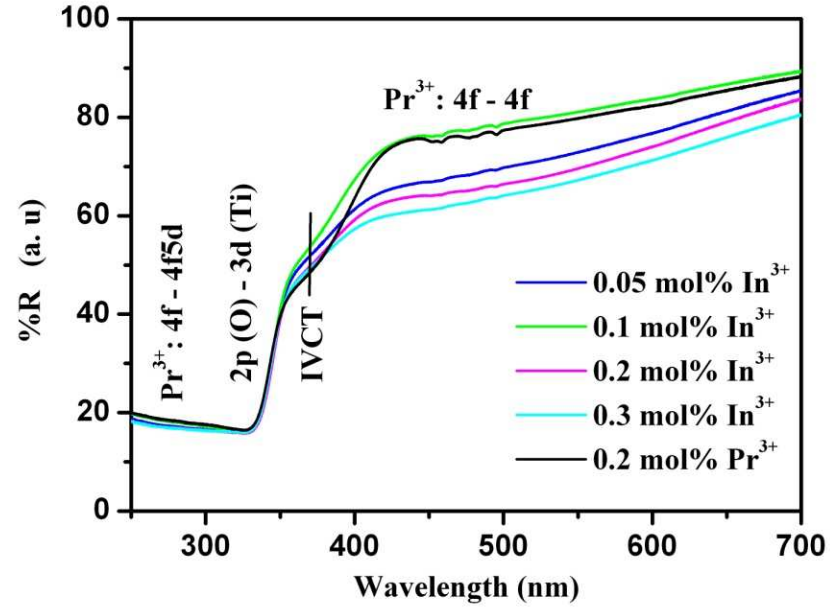

Figure 4.4: Diffuse reflectance spectra of $CaTiO_3$*:0.2* Pr^{3+}*,* yIn^{3+}

The PL emission spectra (figure 4.5a) of $CaTiO_3$:$0.2Pr^{3+}$, yIn^{3+} (y = 0.05, 0.1, 0.2, and 0.3 mol%) were measured using a low PMT voltage (400 V) at room temperature. 0.1 mol% In^{3+} concentration shows the highest PL intensity (figure 4.5b), and for higher In^{3+} concentrations, concentration quenching comes to play. The role of In^{3+} in $CaTiO_3$:Pr^{3+},In^{3+} system is to serve as a charge compensator by supressing the effect of non-radiative processes, to enhance Pr^{3+} emission. When Pr^{3+} ions are stochiometrically doped in $CaTiO_3$, they are substituted in the site of Ca^{2+} ions. This introduces an additional positive charge in the local area where they reside, resulting in charge imbalance [1,2].

The material tends to compensate for such imbalance by generating negative defects around the additional positive charge which reside in the forbidden region (as illustrated in figure 4.6). These are negative oxygen point defects $(O_i^{\cdot\cdot})$ that temporarily trap and release h^+ to the $^3H_4$ level, and also positive calcium $(Ca_i^{''})$ point defects that trap and hold e^-, are formed in the process.

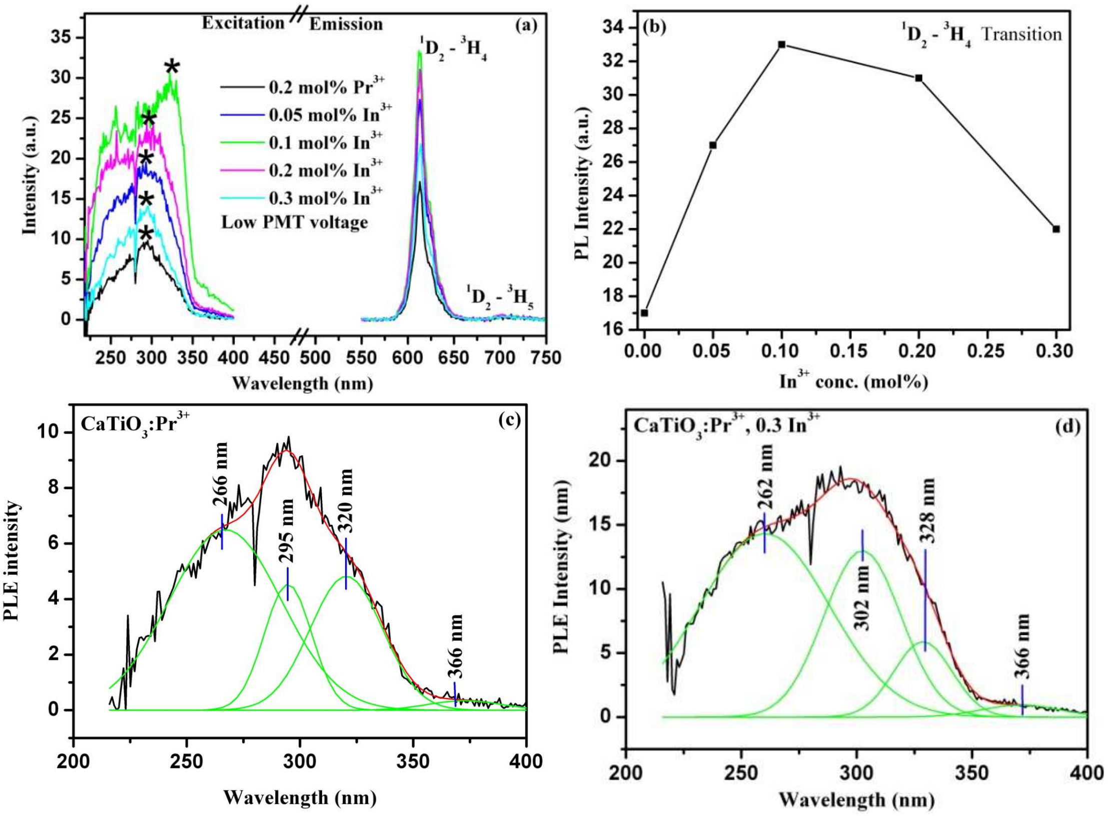

Figure 4.5: (a) PL spectra of $CaTiO_3:0.2Pr^{3+}$ doped with different In^{3+} concentration and (b) PL intensity as a function of In^{3+} concentration.

The latter point defects are responsible for the generation of negative calcium vacancies (V_{Ca}'') that trap and hold h^+. Upon excitation, the carriers trapped by $Ca_i^{\cdot\cdot}$ and V_{Ca}'' centres recombine non-radiatively. Introducing In^{3+} ions in the system serves to minimize the density of the non-radiative centres by reducing the density of charge imbalance in the local areas where Pr^{3+} ions are situated, through substitution of Ti^{3+} ions. The reduced density of non-radiative centres ensures more supply of carriers to the Pr^{3+} centres, and hence an enhanced emission of $CaTiO_3:Pr^{3+}$ in the presence of In^{3+} co-dopant [1,2,8,10].

When the material compensates for charge imbalance by generating negative oxgen point defects around the additional positive charge, positive oxygen vacancies ($V_O^{\cdot\cdot}$) are formed in the process. The trapping and release of carriers by the $V_O^{\cdot\cdot}$ and O_i'' centres, result in the long afterglow emission by $CaTiO_3:Pr^{3+}$[4,7,9].The afterglow decay curves of $CaTiO_3:Pr^{3+}$, In^{3+} are presented in figure 4.7 and the corresponding decay times in Table 4.1, and each phosphor was excited for 10 minutes..

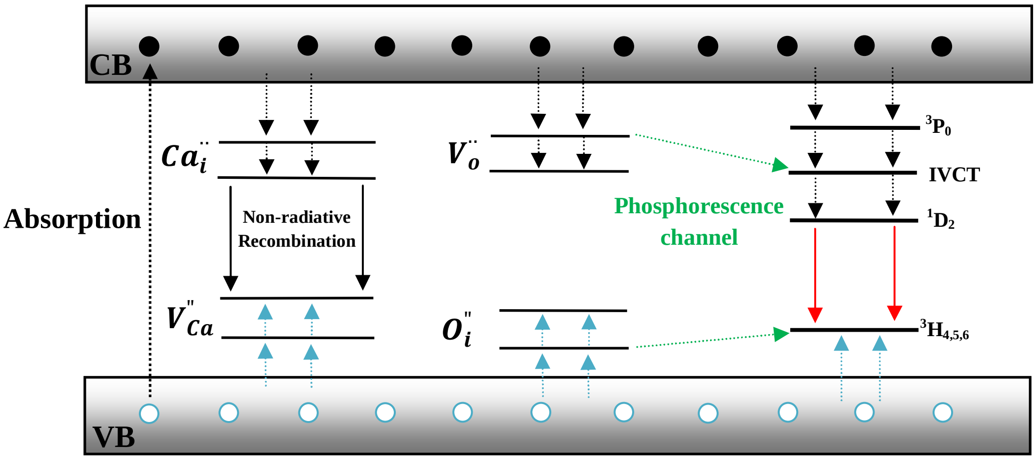

Figure 4.6: Charge transfer mechanism in $CaTiO_3:Pr^{3+}$, In^{3+}

Upon adding In^{3+} ions, the afterglow decay time increased from 330 to 400 s with an increase in In^{3+} concentration.The increased afterglow time upon adding In^{3+} ions may be a result of more oxygen vacancies formed in the system at the local sites of In^{3+}.The latter effect may be because of the increased non-radiative centres that are generated as a result of structural distortion by higher mole percentage doping of In^{3+} [1,2,3,7,8]. Oxygen vacancies are formed due to self compensation of the material when Ca^{2+} is replaced with a Pr^{3+} ion. If more In^{3+} is added into the Ti^{4+} position this process is reversed and the number of defects maybe decreases specially for higher concentrations as in this case and the decay times will decrease. The addition of In therefore may decrease the defect formation at higher concentrations. Ghildiyal et. al. [13] found that the aliovalent ion substitution viz. Li^{+1}, K^{+1} and Na^{+1} suitably minimize the vacancy and defects created by Tb^{+3} ion doping in Sr_2SiO_4.

The phosphorescence decay curves are divided into two components; The fast decay component within the first second, and the slow decay component lasting longer than one second, which is attributed to trapping and detraping of charge carriers by oxygen vacancies [2,3,4]. As proposed by Ghildiyal et. al. [13], Charge compensation may have negative effects on the phosphorescence life time of phosphors; the phosphorescence lifetime measurements presented in table 1 indicate the effect of In^{3+} charge compensation in the matrix at different In^{3+} concentrations.

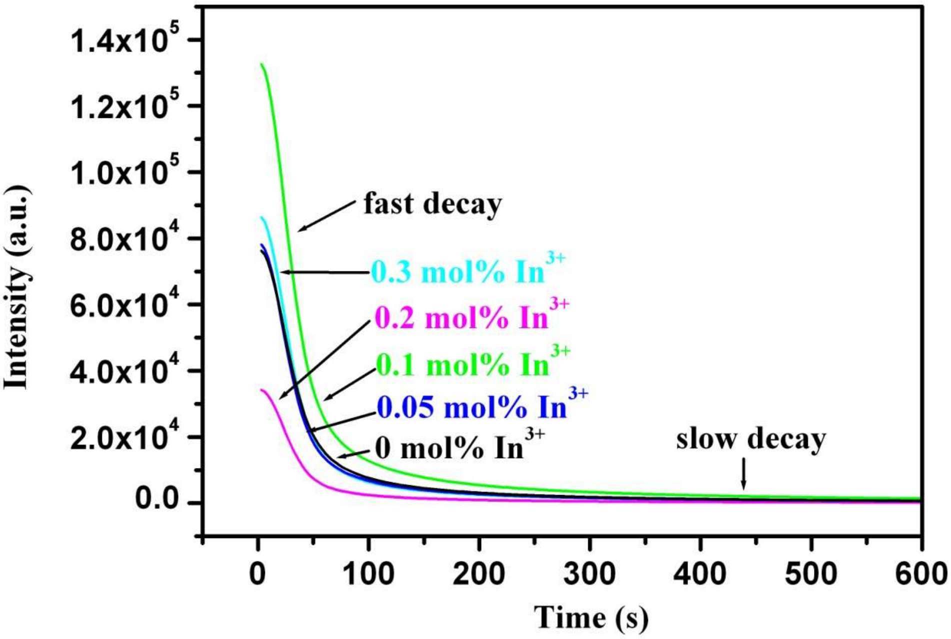

Figure 4.7 : Phosphorescence decay curves $CaTiO_3:Pr^{3+}, In^{3+}$

The curves are fitted with a second order exponential decay equation (Eq. 4.2) [1,2,8,10].

$$\boldsymbol{I(t) = Ae^{-t/\tau_1} + Be^{-t/\tau_2}} \qquad [\mathbf{4.2}]$$

where $\boldsymbol{I}$ is the luminescence intensity as a function of time $\boldsymbol{t}$, with $\boldsymbol{A}$ and $\boldsymbol{B}$ are the amplitudes of the first and the second components, and $\boldsymbol{\tau_1}$ and $\boldsymbol{\tau_2}$ represent the lifetime of the first and second components.

As mentioned in the above discussion of phosphorescence lifetime, the process is dependent on trapping and detrapping of carriers by trap centres of different depths within the material [14]. Carriers that are initially trapped within deeper trap centres reveal a longer afterglow as compared to those trapped within shallow trap centres [5]. The TL was used to reveal the actual depth and to trap centres and their change in density upon adding different concentrations of In^{3+} in $CaTiO_3:Pr^{3+}$ phosphor. The resulting glow curves are presented in figure 4.8, and the data in table 4.2. With fig. 4.8a presenting $Ca_{0.998}TiO_3:0.002Pr^{3+}$, fig. 4.8b presenting

$Ca_{0.998}Ti_{0.9995}O_3:0.002Pr^{3+},0.0005In^{3+}$, fig. 4.8c presenting $Ca_{0.998}Ti_{0.999}O_3:0.002Pr^{3+},0.001In^{3+}$, fig. 4.8d presenting $Ca_{0.998}Ti_{0.998}O_3:0.002Pr^{3+},0.002In^{3+}$, and fig. 4.8e presenting $Ca_{0.998}Ti_{0.997}O_3:0.002Pr^{3+},0.003In^{3+}$.

Table 4.1: Decay times τ_1 and τ_2 for $CaTiO_3:Pr^{3+}$ and co-doped with In^{3+} phosphors.

Compound	**τ_1 (S)**	**τ_2 (S)**	**R^2**
$Ca_{0.998}TiO_3:0.002Pr^{3+}$	32.6 ± 0.6	330 ± 54	0.991
$Ca_{0.998}Ti_{0.9995}O_3:0.002Pr^{3+},0.0005In^{3+}$	30.3 ± 0.6	340 ± 62	0.991
$Ca_{0.998}Ti_{0.999}O_3:0.002Pr^{3+},0.001In^{3+}$	32.0 ± 0.6	370 ± 69	0.990
$Ca_{0.998}Ti_{0.998}O_3:0.002Pr^{3+},0.002In^{3+}$	30.1 ± 0.6	400 ± 129	0.989
$Ca_{0.998}Ti_{0.997}O_3:0.002Pr^{3+},0.003In^{3+}$	30.4 ± 0.6	400 ± 127	0.989

The broad single glow curve that may be deconvoluted to different sub glow peaks is an indication of closely overlapping trap centres [14]. The activation energy needed to detrap carriers within such trap centres may be estimated using Chen's first order kinetic model (Eq. 4.3) [15]. The activation energy is proportional to the depth of the trap centres.

$$\boldsymbol{E = 2.52\left(\frac{kT_m^2}{\omega}\right) - 2kT_m} \qquad [4.3]$$

where $\boldsymbol{E}$ is the depth of the traps in eV, $\boldsymbol{k}$ = 8.617 eV.K^{-1} is Boltzmann's constant, $\boldsymbol{T_m}$ is the temperature corresponding to the maxima of a thermal peak, and ω is the FWHM of a thermal peak. The corresponding frequency factor $\boldsymbol{s}$ (s^{-1}) was calculated using equation 4.4 [14], and the concentration of the trap centres was modelled with Randal Wilkins model (Eq. 4.5) [16]. The corresponding data is given in table 4.2.

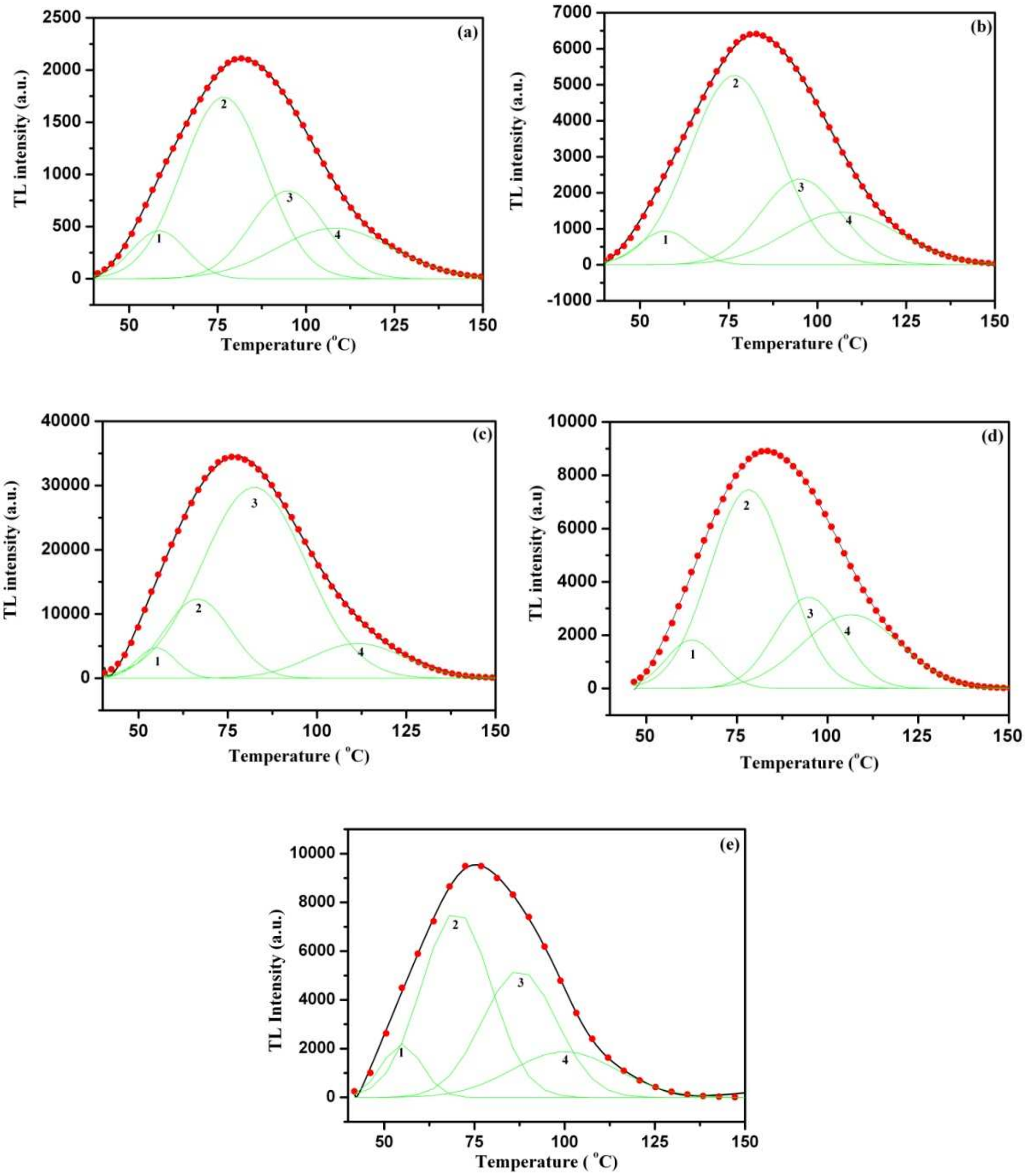

Figure 4.8: Deconvoluted glow curves of $CaTiO_3$:Pr^{3+} and In^{3+} co doped phosphors

$$\boldsymbol{s = \left(\frac{\beta E}{kT_m^2}\right) exp\left(\frac{E}{kT_m}\right)} \qquad [\mathbf{4.4}]$$

The glow curves where acquired using a linear heating rate of 2 °C/s ($\boldsymbol{\beta}$ = 2 °C).

$$\boldsymbol{I(t) = n_o s exp\left(-\frac{E}{kT_m}\right)} \qquad [\mathbf{4.5}]$$

Where $\boldsymbol{n_o}$ (cm^{-3}) is the carrier (electrons) concentration trapped at time $\boldsymbol{t}$ (s) and $\boldsymbol{I}$ is the TL intensity.

Table 4.2: The kinetic parameters of trap levels relating to CaTiO$_3$:Pr^{3+} and co-doped with In^{3+} phosphor

	peak1	***peak2***	***peak3***	***peak4***
$Ca_{0.998}TiO_3$:0.002Pr^{3+}				
Max. Temp., $\boldsymbol{T_{max}}$ (K)	331	349	368	381
FWHM	32 ± 6	21 ± 4	23 ± 6	15 ± 2
Activation Energy, ***E*** (eV)	0.69	1.19	1.20	2.03
Frequency factor, ***s*** (s^{-1})	4.1×10^{09}	4.7×10^{16}	9.1×10^{15}	2.7×10^{26}
Concentration, $\boldsymbol{n_o \times 10^3}$ (cm^{-3})	14.5	09.2	10.1	06.4
$Ca_{0.998}Ti_{0.9995}O_3$:0.002Pr^{3+},0.0005In^{3+}				
Max. Temp., $\boldsymbol{T_{max}}$ (K)	330	350	368	379
FWHM	14 ± 2	25 ± 3	22 ± 8	31 ± 14
Activation Energy, ***E*** (eV)	1.63	1.00	1.27	0.94
Frequency factor, ***s*** (s^{-1})	2.9×10^{24}	5.4×10^{13}	5.9×10^{16}	4.9×10^{11}
Concentration, $\boldsymbol{n_o \times 10^3}$ (cm^{-3})	18.4	33.8	29.4	42.2
$Ca_{0.998}Ti_{0.999}O_3$:0.002Pr^{3+},0.001In^{3+}				
Max. Temp., $\boldsymbol{T_{max}}$ (K)	328	340	355	384
FWHM	26 ± 3	28 ± 3	18 ± 7	10 ± 2
Activation Energy, ***E*** (eV)	0.84	0.83	1.45	2.13

Frequency factor, ***s*** (s^{-1})	1.5×10^{12}	4.4×10^{11}	1.3×10^{20}	7.0×10^{40}
Concentration, n_o **× 10**^{3} (cm^{-3})	19.0	20.6	12.8	70.2
$Ca_{0.998}Ti_{0.998}O_3:0.002Pr^{3+},0.002In^{3+}$				
Max. Temp., T_{max} (K)	335	351	368	380
FWHM	14 ± 4	21 ± 10	18 ± 6	26 ± 7
Activation Energy, ***E*** (eV)	1.60	1.20	1.50	1.14
Frequency factor, ***s*** (s^{-1})	7.2×10^{24}	6.0×10^{16}	8.6×10^{20}	2.4×10^{14}
Concentration, n_o **× 10**^{3} (cm^{-3})	25.5	38.9	33.0	48.5
$Ca_{0.998}Ti_{0.997}O_3:0.002Pr^{3+},0.003In^{3+}$				
Max. Temp., T_{max} (K)	328	343	361	373
FWHM	28 ± 1	20 ± 9	19 ± 4	11 ± 1
Activation Energy, ***E*** (eV)	0.78	1.20	1.40	2.60
Frequency factor, ***s*** (s^{-1})	1.5×10^{11}	1.9×10^{17}	2.1×10^{19}	7.8×10^{35}
Concentration, n_o **× 10**^{3} (cm^{-3})	52.8	39.6	37.5	21.3

4.4. Conclusion

The single red emission at 613 nm which corresponds to $^1D_2$ – $^3H_4$ transition of Pr^{3+} as a result of complete depopulation of the $^3P_0$ state, is observable upon activating $CaTiO_3$ with Pr^{3+}. In^{3+} was co-doped into $CaTiO_3:Pr^{3+}$ phosphor to achieve charge compensation by suppressing the density of the quenching centre, and also to enhance phosphorescence decay time by generating more oxygen vacancies. The resulting effect was an enhanced luminescence intensity of the single red emission peak at 613 nm and afterglow decay time. In^{3+} concentration was effective in luminescence intensity enhancement up to 0.1 mol% and for higher mol% doping concentration quenching occurred. The increased phosphorescence lifetime upon increasing In^{3+} concentration is caused by structural deformation which leads to a generation of more defects in the material that lead to a longer trapping and detrapping process, as revealed by trap center quantification using TL spectroscopy. The phase of the phosphors was identified using XRD, from which no visible traces are present that may point to possible distortion of $CaTiO_3$ upon incorporating Pr^{3+} and In^{3+} ions into this matrix. Particles of $CaTiO_3$ were estimated using Scherer's equation from the XRD patterns, and the average particle size was 0.6 μm. The surface morphology was identified using SEM and the particles were agglomerated and they were of different shapes and sizes.

4.5. References

[1] P. Boutinaud, L. Sarakha, E. Cavalli, M. Bettinelli, P. Dorenbos, R. Mahiou, *J.Phys. D: Appl. Phys.*, **42** (2009) 045106

[2] P. Boutinaud, E. Pinel, M. Dubois, A.P. Vink, R. Mahiou, *J. Lumin.*, **111** (2005) 69

[3] P.J. Deren, R. Pazik, W. Strek, P. Boutinaud, R. Mahiou, *J. Alloys Compd.*, **451** (2008) 595

[4] S. Yin, D. Chen, W. Tang, *J.Alloy and Compd.*, **441** (2007) 327

[5] X. Zhang, C. Cao, C. Zhang, S. Xie, G. Xu, J. Zhang, X. Wang, *Mater. Res. Bull.*, **45** (2010) 1832

[6] S. Li, X. Liang, *J. Mater. Sci: Mater Electron*, **19** (2008) 1147

[7] P. Bautinaud, E. Pinel, M. Oubaha, R. Mahiou, E. Cavalli, M. Betinelli, *J. Opt. Mater.* **28** (2006) 9

[8] X. Zhang, J. Zhang, X. Chen, S. Lu, X.J. Wong, *J. Lumin.* **122** (2007) 958

[9] W. Tang and D. Chen, *Phys. Status Solidi A* **206** (2), (2009) 229

[10] W. Tang, D. Chen, *Mater. Res. Bull.*, **44** (2009) 836

[11] P. Boutinaud, E. Pinel, R. Mahiou, *Opt. Mater.*, **30** (2008) 1033

[12] P.S. Khiew, S. Radiman, N.M. Huang, Md. Soot Ahmad, *J.Cryst. Growth*, **254** (2003) 239

[13] R. Ghildiyal, C.H. Hsu and C.H. Lu 2011 *Int. J. Appl. Ceram. Technol.*, 8(4) 759

[14] S.S. Pitale, S.K. Sharma, R.N. Dubey, M.S. Qureshi, M.M. Malik, J. Lumin. **128** (2008) 1587

[15] R. Chen, J. Appl. Phys. **40** (1969) 570

[16] Md. S. Alam, S. Bauk, Adv. Studies Theor. Phys. **4** (14), (2010) 66

5

Surface chemical changes of $CaTiO_3:Pr^{3+}$ upon electron beam irradiation

5.1. Introduction

$CaTiO_3:Pr^{3+}$ phosphor has a better colour rendering index compared to the currently used phosphor ($Y_2O_3:Eu^{3+}$) in Television technology. However, operating conditions of television display devices demand life-testing of phosphor materials for their surface chemical stability [1]. Field Emission Displays (FED) require low voltage phosphors that are resistant to electron beam irradiation ageing, and oxide phosphors have been found as optimal candidates for FEDs [2,3]. $SrTiO_3:Pr^{3+}$ was reported to be a successful candidate for red phosphors in FEDs, in 1996 [4]. This study is done to investigate the surface chemical changes of $CaTiO_3$ under prolonged electron beam irradiation *in-situ* at 1×10^{-6} O_2 and 1×10^{-8} Torr, which is from a similar family as $SrTiO_3$; the perovskite type crystal structures.

In ultra high vacuum, there exist various gases of which O_2 and H_2O are included because they are difficult to pump. The electron beam is known to dissociate such molecular species to reactive atomic species, like:

$$O_2 \rightarrow O^{2-} \text{ and}$$

$$H_2O \rightarrow OH^- + O^-$$

According to Electron Stimulated Surface Chemical Reaction (ESSCR) mechanism, prolonged electron beam irradiation on the surface of a phosphor material leads to surface dissociation, and hence a change of the surface chemical state. The reactive O^- atomic species may also adsorb onto to the surface of these materials and form a non-luminescent oxide layer with the elements on the surface. Such surface chemical state changes diminish the chemical stability of phosphor materials and the cathodoluminescence intensity [5,6].

5.2. Experimental

0.2 mol% Pr^{3+} doped $CaTiO_3$ was prepared by solid state reaction at 1200 °C for 4h by directly baking TiO_2 (anatase phase), $CaCO_3$, and $PrCl_3$. Si ions were also added in the compound in pursuit to enhance phosphorescence properties. This phosphor material was subjected to a prolonged electron beam irradiation to investigate its surface chemical changes *in-situ* at 1×10^{-6} O_2 and 1×10^{-8} Torr by an Auger Electron Spectroscopy (AES - PHI 549) using an electron beam of 2 keV energy and 10 μA beam current to probe the surface of the specimen, and Cathodoluminescence intensity changes were monitored by Cathodoluminescence (CL) spectrometer (Ocean Optics Inc. PC2000). The surface chemical state was investigated by a PHI 5000 *Versa-probe* X-ray Photoelectron Spectroscopy (XPS) using 100 μm 25 W 15 kV Al monochromatic x-ray beam.

5.3. Results and Discussion

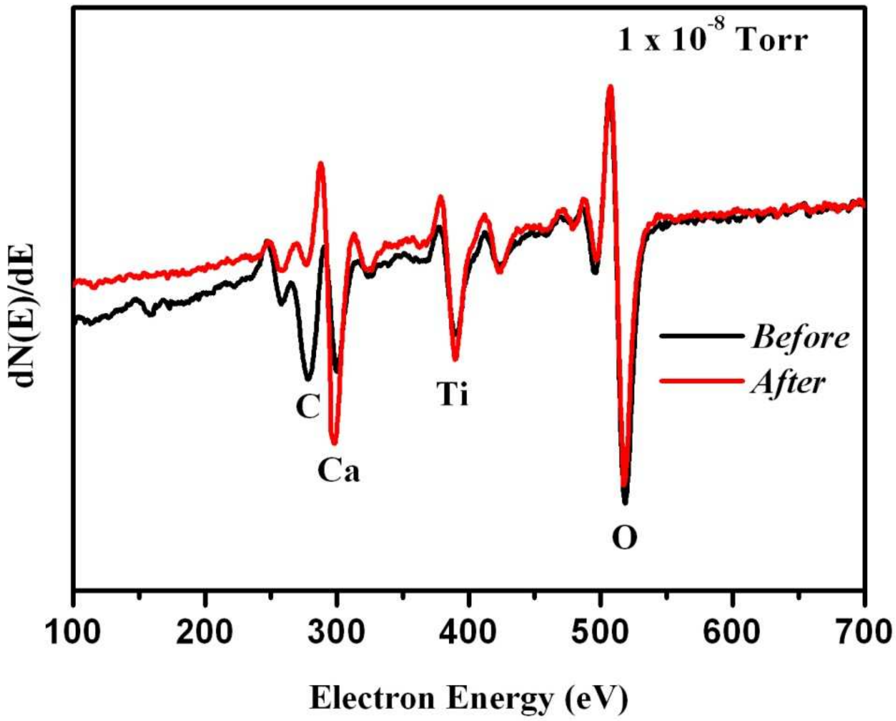

Figure 5.1: Auger spectra of $CaTiO_3$:Pr^{3+} before and after degradation at 1×10^{-8} Torr

The Auger spectrum (Fig. 5.1) shows the existence of Ca, C, Ti and O elements on the surface of the $CaTiO_3:Pr^{3+}$ phosphor at 1×10^{-8} Torr before degradation. Hence forth during the degradation process, the electron beam removes the adventitious C on the surface. Degradation is a result of the surface dissociation by changing the surface chemical state at the spot under electron beam irradiation as it is discussed below. It leads to cathodoluminescence intensity suppression. Fig. 5.2 shows the cathodoluminescence before and after degradation at 1×10^{-8} Torr (a), and at 1×10^{-6} Torr O_2 (b)

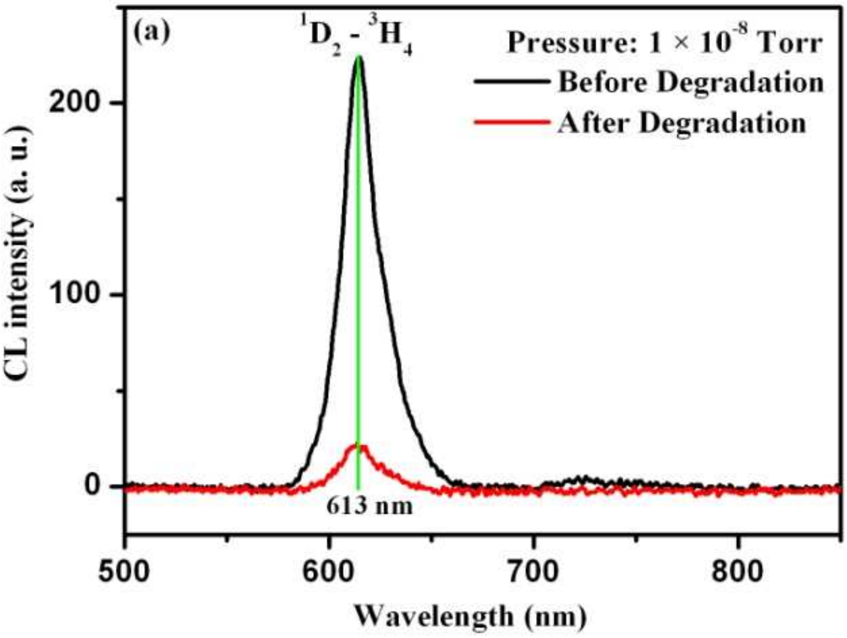

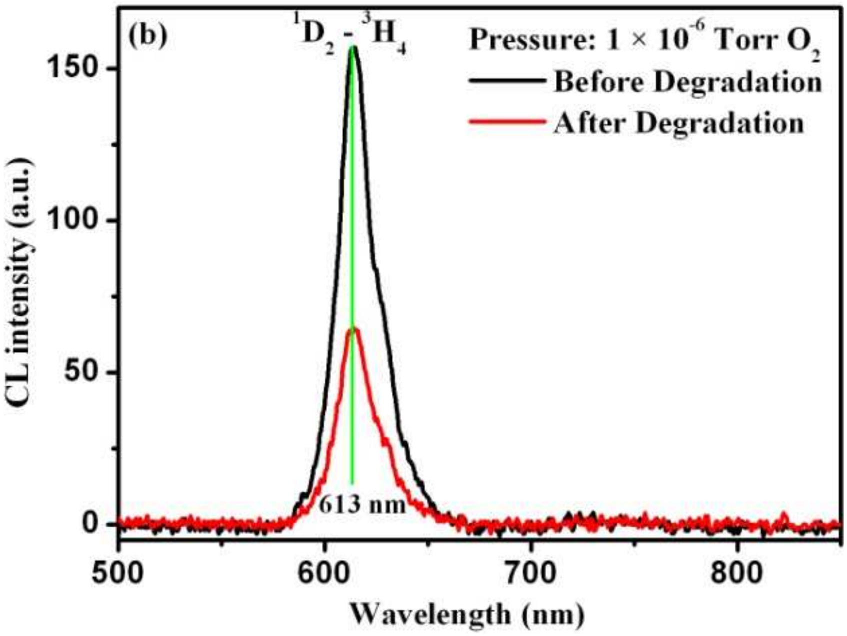

Figure. 5.2: $CaTiO_3$: Pr^{3+} Cathodoluminescence spectra before and after degradation at 1×10^{-8}Torr (a), and at 1×10^{-6}Torr O_2 (b)

Fig. 5.3a shows O species desorption from the surface, and according to the ESSCR mechanism, this brings about oxygen vacancies that lead to charge imbalance on the probed spot. It is a natural ability of materials to self compensate whenever there is charge imbalance by generating additional vacancies [3,5]. The resulting charge imbalance, results in negative Ti and Ca vacancy formation, which act as quenching centres of luminescence, and this may be the reason behind CL intensity decrement. The backfilling of O_2 in the system leads to fast oxidation of the surface, from 0 to 500 $C.cm^{-2}$ electron doses (Fig. 5.3b).

The rate at which the CL intensity degrades at 1 × 10^{-6} Torr O_2 is higher than that at 1 × 10^{-8} Torr because of the backfilled oxygen inside the vacuum chamber, which has a role of oxidizing the surface to form the non-luminescent layer. This is a result of more O^- atomic species that are formed by electron beam dissociation in an environment with more oxygen.

According the ESSCR mechanism, surface oxidation often results in an additional species that forms an additional layer on the surface which is non-luminescent, as mentioned earlier [5]. The

chemical state of the surface of $CaTiO_3:Pr^{3+}$ before and after the degradation process using a 2 keV energetic electron beam at 1×10^{-6} Torr O_2, was probed on the surface using an XPS.
According to Fig. 5.4, the Ca 2p peak consists of 3 peaks before degradation that are a contribution of Ca doublet at 345.9 and 346.6 eV Binding energies(BE) from the matrix ($CaTiO_3$) and 1 peak at 347.6 eV (BE) from $Ca(OH)_2$. According to van der Heide[13], The double is a result of negative BE shifts induced by inter and intra atomic initial state effects, because the atoms located at the outer most surface are expected to exhibit binding energy (BE) shifts due to the less stable chemical environment produced on the abrupt termination of the bulk lattice structure, and the $Ca(OH)_2$ compound that forms on the surface arises as a result of the OH^- group from the surrounding water vapour that is chemisorbed on the surface.

After degradation, the peak of lower BE from the Ca doublets disappears and an additional peak is introduced at 345.4 eV BE that comes from CaO as result of surface oxidation at 1×10^{-6} Torr O_2 [7, 8, 11].
According to Fig. 5.5, The Ti 2p peak consists of 4 peaks at 456.8 eV BE from Ti_2O_3, 457.4 eV BE from TiOH, 457.7 eV BE from the matrix ($CaTiO_3$) and at 458.4 from TiO_2 used as a reagent. In general titanium can assume Ti^{4+} from TiO_2 and $CaTiO_3$, Ti^{3+}, and Ti^{2+} oxidation states in sub oxides that may form as a result of chemisorbed OH^- group and surface irradiation by energetic particles like photons or an electron beam, like Ti-OH and Ti_2O_3 hexagonal titanium oxide [8, 9, 10, 12].

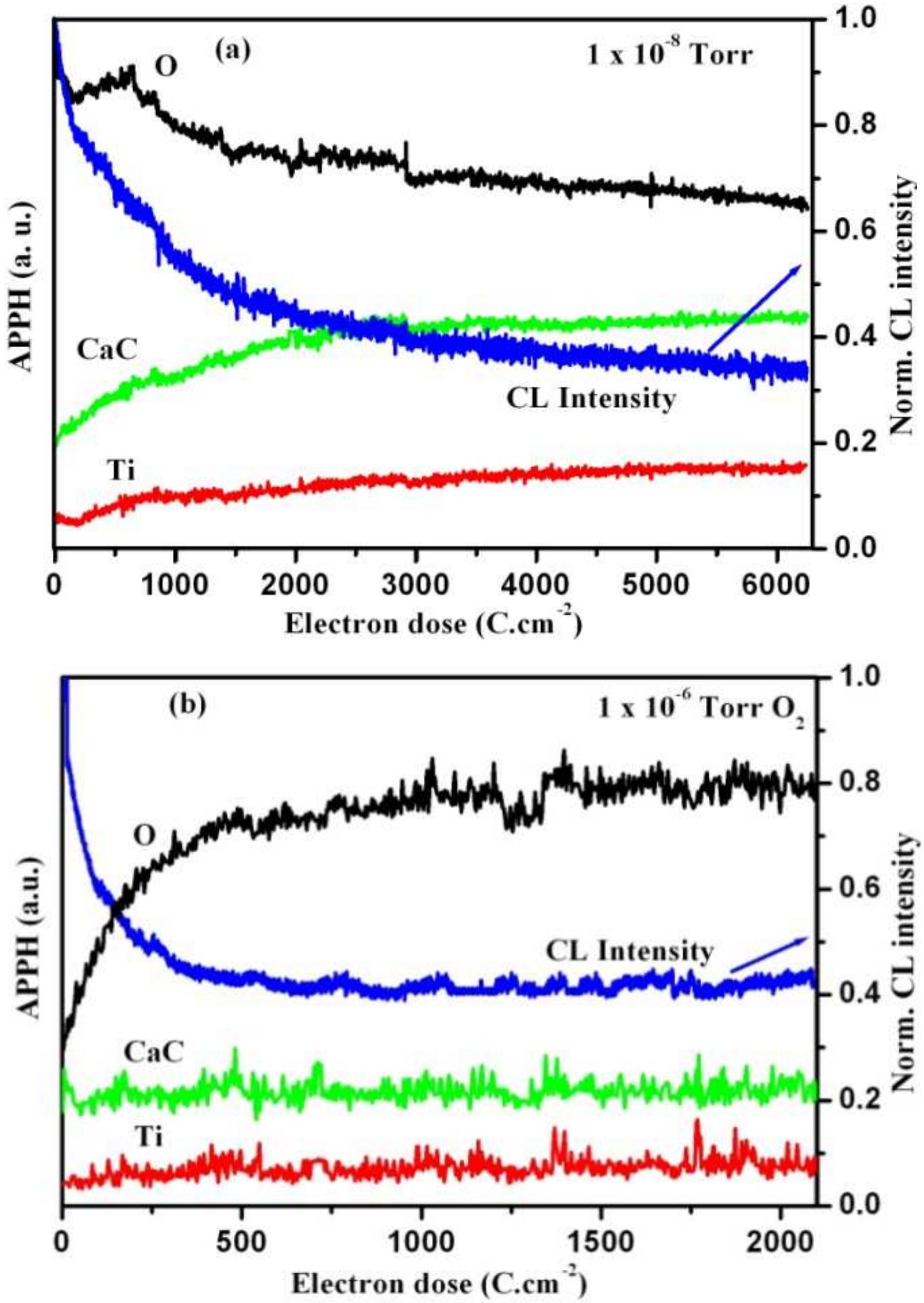

Figure 5.3: APPH and CL intensity changes of $CaTiO_3$: Pr^{3+} at 1×10^{-8} Torr (a), and 1×10^{-6} Torr O_2 (b)

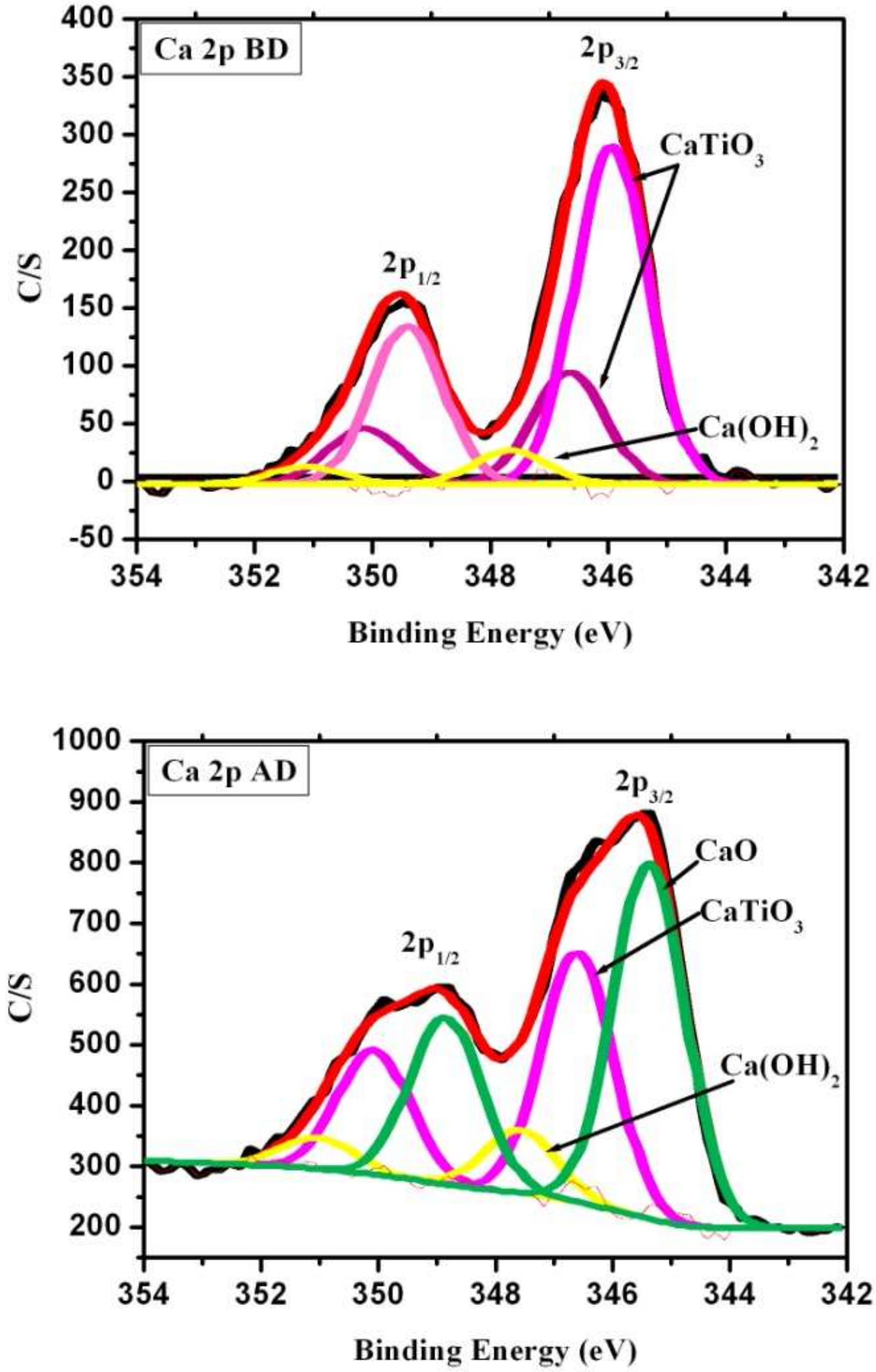

Figure 5.4: Spectra of Ca 2p before (Ca 2p BD) and after (Ca 2p AD) degradation

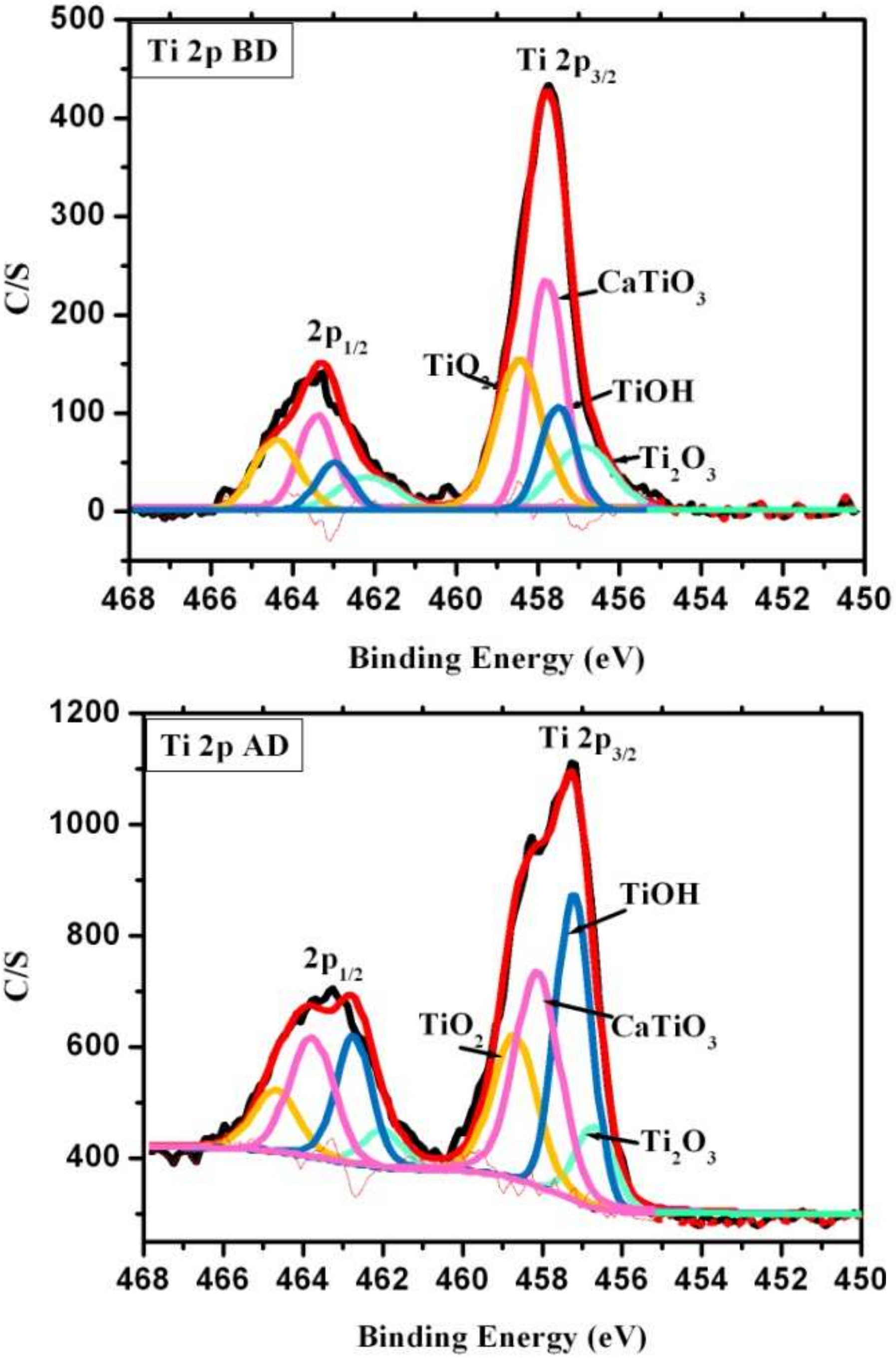

Figure 5.5: Spectra of Ti 2p before (Ti 2p BD) and after (Ti 2p AD) degradation

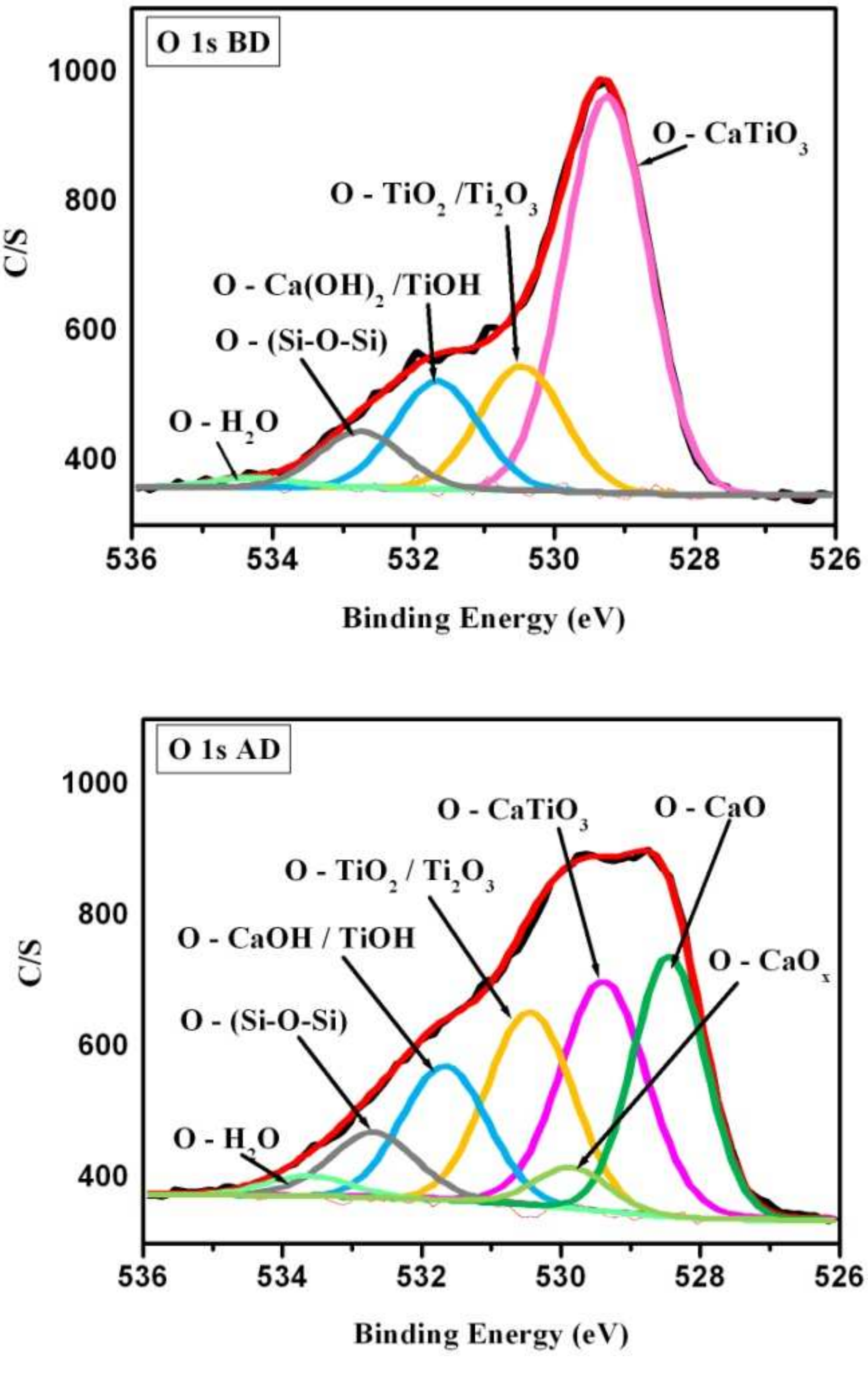

Figure 5.6: Spectra of O 1s before (O 1s BD) and after (O 1s AD) degradation

According to Fig. 5.6, Oxygen peak O 1s consist of 5 peaks prior degradation, contributed by peaks at 529.1 eV BE from the matrix ($CaTiO_3$), 530.3 eV BE from TiO_2 and Ti_2O_3, 531.5 eV BE from the OH^- group bonded species, 532.6 eV the Si-O-Si species may have been incorporated in the phosphor during the preparation of the system using silica crucibles orbeccause of the Si ions that were introduced into $CaTiO_3$ to generate more oxygen traps that will act by enhancing the decay time of the luminescence of, and 534.2 eV BE from the chemisorbed species. After Degradation, the O 1s peak is deconvoluted into 7 peaks, with the additional peaks at 528.4 from the CaO formed on the surface as a result of surface oxidation, and at 529.8 eV BE as a result of CaO_x sub oxide formation.

5.4. Conclusion

Upon prolonged electron beam doses on the surface of $CaTiO_3:Pr^{3+}$, the CL intensity of Pr^{3+} ions decreases and then stabilizes. The decrement is faster at 1×10^{-6} Torr O_2 than at 1×10^{-8} Torr because of more oxygen present in the vacuum that oxidizes the surface of the material faster. The XPS analysis performed on the surface degraded at 1×10^{-6}Torr O_2 suggests that CaO and CaO_x non luminescent layers formed on the surface. The resulting defect layer upon the formation of the layers is responsible for the decrease of luminescence intensity of $CaTiO_3:Pr^{3+}$**.** The surface instability of $CaTiO_3:Pr^{3+}$ phosphor at 1×10^{-6} Torr O_2 from 0 – 500 $C.cm^{-2}$ which is an environment that is more similar those of field emission displays, points out that the surface of this material needs to be coated to make it more stable against prolonged electron beam irradiation.

5.5. References

[1] P.J. Deren, R. Pazik, W. Strek, Ph. Boutinaud, R. Mahiou, J. Alloys Compd. **451** (2008) 595

[2] Yuexiao Pan, Giang Su, Haufang Xu, Tianhu chen, Weikun Gee, Chunlei Yang, and Mingmei, J. Solid State Chem. **174** (2003) 69

[3] Phillipe Boutinaud, Rachid Mahiou, Enrico Cavalli, Marco Bettinelli, Chem. Phys. Lett. **41**8 (2006) 185

[4] Jinfeng Tang, Xibin Yu, Liangzhun Yang, Chunlei Zhou, Xiudong Peng, Mater. Lett. **60** (2006) 326

[5] H.C. Swart, J.S. Sebastian, T.A. Trottier, S.L. Jones, and P.H. Holloway, J. Vac. Sci. Technol. **14**(3), (1996) 1697

[6] Shreyas S. Pitale, Vinay Kumar, I.M. Nagpure, O.M. Ntwaeaborwa, E. Coetzee, and H.C. Swart, J. Appl. Phys. **109** (2011) 013105

[7] Vinay Kumar, Varun Mishra, Shreyas S. Pitale, I.M. Nagpure, E. Coetzee, O.M. Ntwaeaborwa, J.J. Terblans, and H.C. Swart, J. Appl. Phys. **107** (2010) 123533

[8] Haimei Liu, Wensheng Yang, Ying Ma, Jiannian Yao, Appl. Catal A: **299** (2006) 218

[9] S. Myhra, G.E. Bishop and J.C. Riviere. Surf Technol, **19** (1983) 161

[10] Byung-Soo Kang, young-Taeg Sul, Carina B. Johansson, Se-jing Oh, Hyun-Ju Lee and Tomas Albrektsson, Clin. Oral Impl. Res. **Xx**, 2011; 000 – 000

[11] Jean-Charles Dupin, Danielle Gonbeaum Phillippe Vinatier and Alain Levasseur, Phys. Chem. Chem. Phys., **2** (2000) 1319

[12] Nina Aas, Thomas J. Pringle and Michael Bowker, J. chem. Soc. Faraday Trans. **90** (7), (1994) 1015

[13] P.A.W. van der Heide, Surf. Sci. **490** (2001) L619

6

Luminescent dynamics of Pr^{3+} in $MTaO_4$ host

6.1 Introduction

Rare earth tantalates ($MTaO_4$) with M = Gd, Y, La, are being extensively studied for possible applications in X-ray imaging systems and mercury free fluorescent lamps, and field emission display (FED) devices due to their high luminescence efficiency, physical and chemical stability, strong irradiation hardness and good X-ray absorption [1–4,6]. In recent years, trivalent praseodymium (Pr^{3+}) doped materials displaying red persistent luminescence have been of considerable interest in the development of long persistent materials. This persistent (long afterglow) luminescence was observed in several matrices. For example, red emission was observed from Pr^{3+} doped $CaTiO_3$, which is attributed to the intervalence charge transfer state (IVCT), through complete depopulation of the $^3P_0$ state and a subsequent populating of the $^1D_2$ state [5,6,22].

The rare earth tantalates are in general very difficult to prepare because they can only be crystallized at 1400 ^oC and higher temperatures. In addition it is difficult to produce single phase rare-earth tantalates, i.e. there may be impurity phases in the final product. This is attributed to the fact that there are generally several polymorphs of rare earth tantalates [8,12] One way of minimizing impurity phases in chemical compounds when using solid state reaction is by using Li_2SO_4 as a fluxing agent [8,14] or by preparing the compounds using other methods such as sol-gel method [12] that are known to produce materials that are pure and homogeneous.

A vacuum ultraviolet (VUV)–UV and synchrotron radiation were used to investigate luminescent properties of $GdTaO_4$ and $GdTaO_4:Eu^{3+}$ [4]. It was found that the broad-band emissions were peaking at 384 and 468 nm due to the TaO_4 group and a 316 nm emission due to the $^6P_J \rightarrow {}^8S_{7/2}$ transitions of Gd^{3+} when exciting at -253 °C, but the luminescence was quenched when exciting at room temperature. The excitation spectra of $GdTaO_4:Eu^{3+}$ monitoring the $^5D_0 \rightarrow {}^7F_2$ emission of Eu^{3+} comprised of the interband excitation of the host, the TaO_4 group excitation, the charge transfer states (CTS) of Eu^{3+}–O^{2-} and Gd^{3+} $^8S_{7/2} \rightarrow {}^6I_J$ transitions. Luminescent properties of Pr^{3+} doped $YTaO_4$, $GdTaO_4$ and $LaTaO_4$ are of a great interest from both scientific and applications point of view [3,4,16]. In addition it is well known that generally luminescent dynamics of Pr^{3+} differ from one host matrix/crystal structure to the other.

Furthering the research on rare-earth doped tantalates, in this paper the luminescence properties of Pr^{3+} in different orthotantalate phosphor hosts prepared in the presence of Li_2SO_4 are reported. In addition, the energy distribution of the defect levels within the forbidden region of these compounds determined using the TL spectroscopy is also reported.

6.2. Experimental

Three rare earth tantalate phosphors, $YTaO_4$, $GdTaO_4$, and $LaTaO_4$ doped with 0.5 mol% Pr^{3+} were prepared using the solid state reaction method, at 1200 °C for 4 h in the presence of Li_2SO_4 fluxing agent. The phosphors where prepared by directly firing stochiometric amounts of Y_2O_3, Gd_2O_3, or La_2O_3 with Ta_2O_5 and $PrCl_3$. These were mixed into a slurry using methanol and were then dried at 120 °C for 10 h prior 1200 °C baking. 30 wt% of Li_2SO_4 was then introduced as flux. The samples were cooled to room temperature after they were baked and were immediately washed with distilled water. After washing, the samples were ground into powder with agate pestle and mortar. The resulting compounds were $Y_{0.995}TaO_4:0.005Pr^{3+}$, $Gd_{0.995}TaO_4:0.005Pr^{3+}$ and $La_{0.995}TaO_4:0.005Pr^{3+}$.

The structure was identified with X-ray diffraction (XRD), using a Bruker, AXS D8 Advance X-ray diffractometer using Cu $\boldsymbol{K_\alpha}$ radiation. The XRD spectra were recorded at a scanning rate of 0.036 °/s. The excitation and emission spectra were measured at the Deutsches Elektronen Synchotron (DESY, Hamburg) using the SUPERLUMI station at HASYLAB39. The luminescence spectra at room temperature and at -263 °C were measured within the 300-1000 nm spectral range using 0.3 m (Acton Research Corporation) Spectra Pro308 monochromatorspectrograph in Czerny-Turner mounting equipped with a liquid nitrogen cooled (Princeton Instruments, Inc.) CCD detector.

The Spectral resolution of the analyzing monochromator was ~0.5 nm. The emission spectra were not corrected for the detector sensitivity and monochromator transmission. High resolution time-resolved luminescence excitation spectra were scanned within 50-330 nm with the primary 2 m monochromator in 15° McPherson mounting (3.2 A resolution) using a PMT (Hamamatsu R6358P) detector with a secondary ARC monochromator. The excitation spectra were corrected for the incident photon flux compared to that of a reference sample of sodium salycilate (NaSal) whose quantum efficiency is assumed to be about 58% and is constant over the excitation wavelength range of 4 to 25 eV. The temperature could be varied between -263 and 27 ^{o}C by means of a liquid-helium cryostat (Cryovac GmbH).

The excitation spectra were monitored for red emission of Pr^{3+} around 600 nm. PerkinElmer Lambda 950 UV/VIS spectrometer was used to measure diffuse reflectance spectra, and the diffuse radiation was collected in a 150 mm InGaAs integrating sphere. The collected radiation was then sent to PMT and PbS detectors. TL 10091, NUCLEONIX spectrometer for thermoluminescence (TL), and Shimadzu SSX-550 Scanning electron microscopy (SEM) were used to analyze thermoluminscent properties and surface morphology of the materials respectively.

6.3. Results and Discussions

Figure 6.1 shows the XRD patterns of $YTaO_4$, $LaTaO_4$ and $GdTaO_4$, all doped with 0.5 mol% of Pr^{3+}. Although most of the diffraction lines are in agreement with the lines of the standard ICSD spectra as indicated in figure 6.1, it is clear that the materials have additional phases (as marked with *) from reagents which did not fully react. This confirms the reports that it is not easy to fabricate single phased ortho-tantalates [9–11].

Figure 6.2 shows the SEM images of $GdTaO_4$ (Fig. 6.2a), $YTaO_4$ (Fig. 2b), and $LaTaO_4$ (Fig. 2c). As shown in fig. 6.2 (a) and (c), GdTaO4 and $LaTaO_4$ consist of irregular particles with sharp edges while $YTaO_4$ (Fig. 6.2b) consists of small polyhedron particles of different sizes.

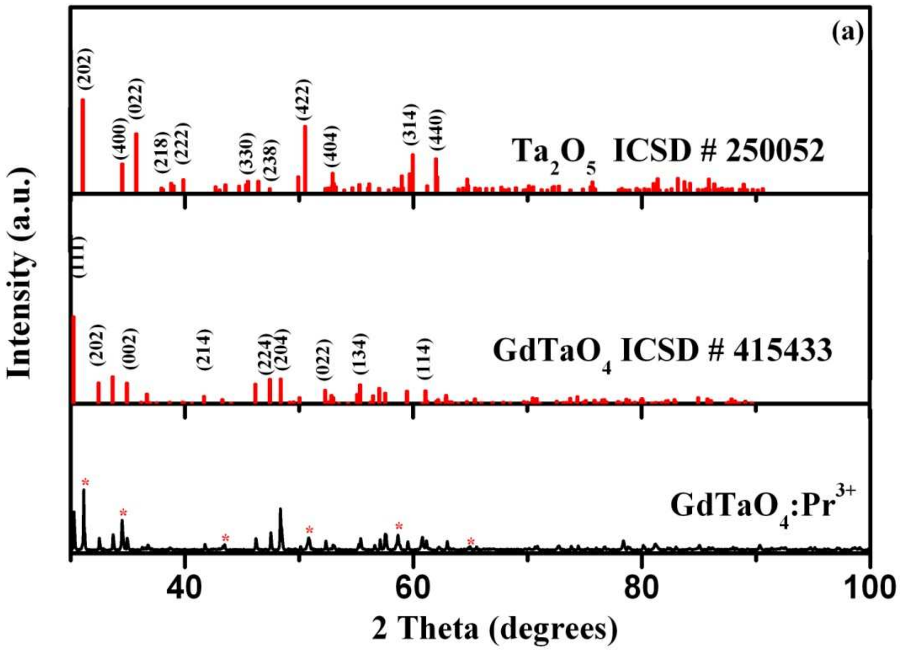

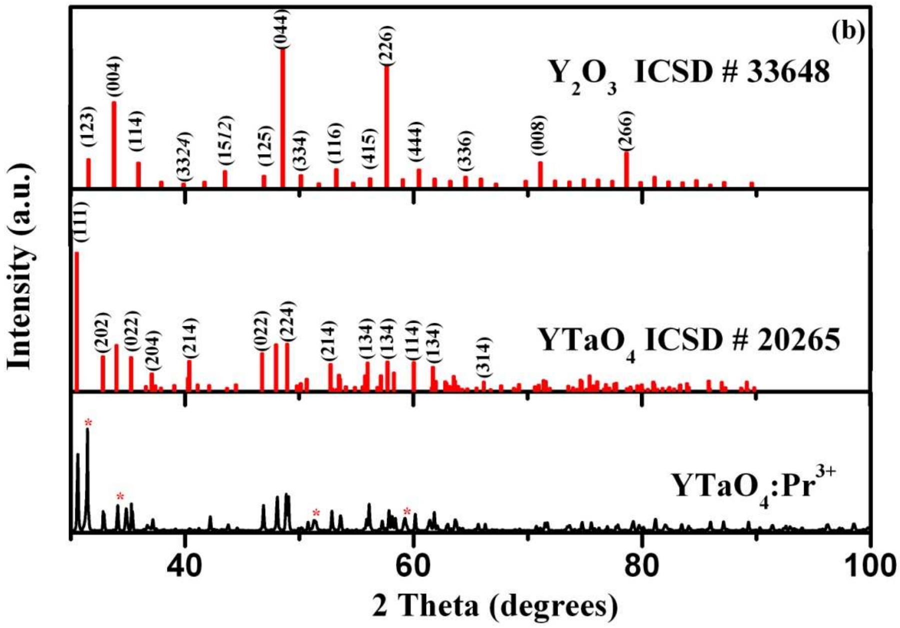

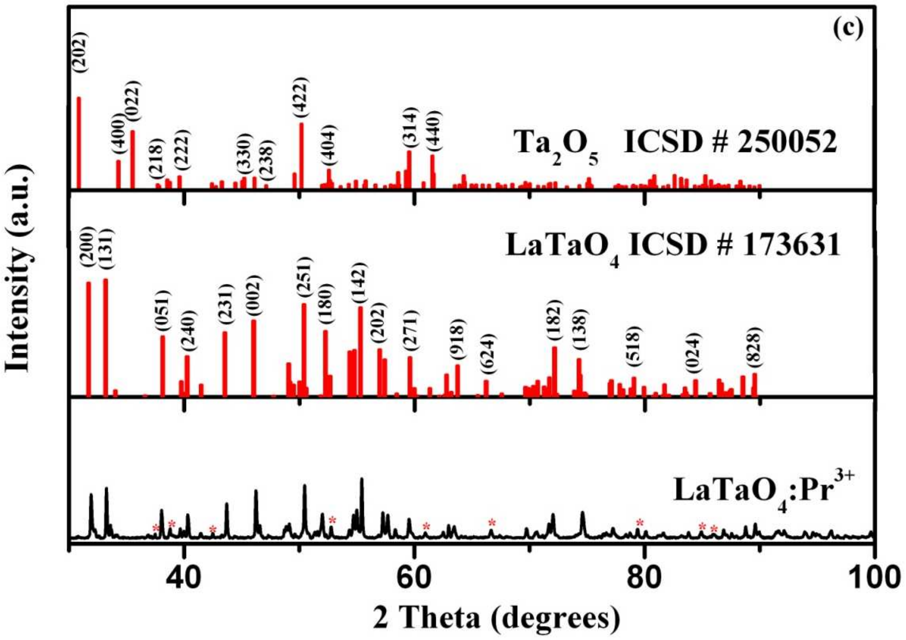

Figure 6.1: XRD patterns of $GdTaO_4$ (a), $YTaO_4$ (b) and $LaTaO_4$ (c) doped with Pr^{3+} ions

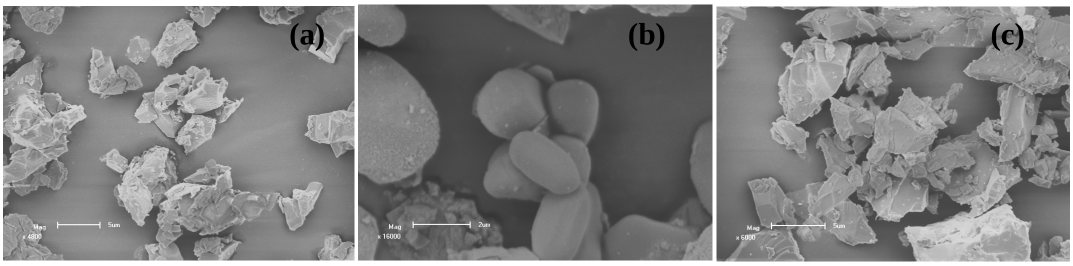

Figure 6.2: SEM images of $GdTaO_4$ (a), $YTaO_4$ (b) $LaTaO_4$ (c)

Diffuse reflectance spectra in figure 6.3 show absorption from the f – f levels of Pr^{3+} around 450 to 490 that correspond to the $^3H_4 \rightarrow {}^3P_{2,1}$, $^1I_6$, $^3P_0$ transitions. The absorptions around 600 nm also correspond to the f - f levels of Pr^{3+} but they are associated with the $^3H_4 \rightarrow {}^1D_2$ and $^3F_2 \rightarrow {}^3P_0$ transitions. A charge transfer from Pr^{3+} to the TaO_4 group was detected around 285 nm [12,14] from $YTaO_4:Pr^{3+}$ and $LaTaO_4:Pr^{3+}$. The transitions around 274 nm and 313 nm from $GdTaO_4:Pr^{3+}$ can be assigned to the $^8S \rightarrow {}^6I_j$, ^6P_j transitions of the Gd^{3+} ions [16]. The charge carriers excited to the TaO_4 CTS and the conduction band will eventually return to the Pr^{3+} ground state by emitting visible light. In the case of $GdTaO_4:Pr^{3+}$ phosphor, the carriers are transferred to Gd^{3+} by the TaO_4, and then from the Gd^{3+} centres to the Pr^{3+} luminescent centre [14].

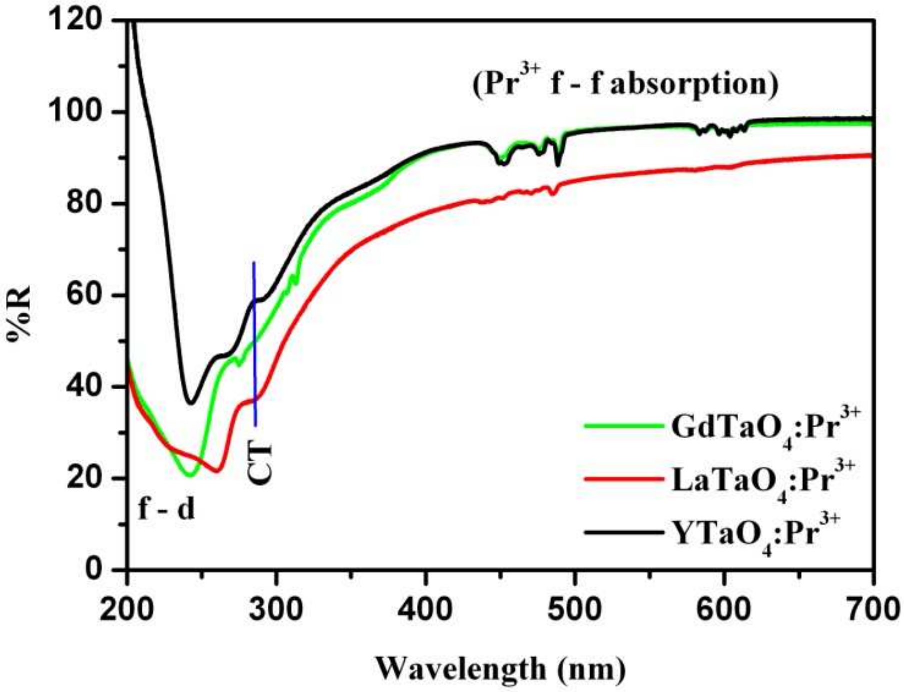

Figure 6.3: Diffused reflectance spectra of the rare- earth tantalates doped with Pr^{3+}

According to the diffused reflectance spectrum (Fig. 6.3) of $GdTaO_4:Pr^{3+}$, there exist both Gd^{3+} and Pr^{3+} absorption centres around 302 to 312 and at 272 to 279 nm from Gd^{3+} , and around 448 to 500 nm and 590 to 625 nm from Pr^{3+}. This is in agreement with the data reported by Blasse et al [16]. The excitation spectra (Fig. 6.4a) measured using the DESY synchrotron radiation has a higher acquisition limit of 330 nm, which forbids the f-f transitions of Pr^{3+}. The narrow f-f transitions of Gd^{3+} observed in the absorption (Fig. 6.3) are also present in the excitation spectra in figure 6.4a, and can be assigned to the $^8S \rightarrow {}^6P_j$ transitions around 302 to 312 nm (A –fig. 6.4a), and $^8S \rightarrow {}^6I_j$ transitions around 272 to 279 nm (B – Fig. 6.4a) at both 10 and 300 K. At 10 K, there is an additional excitation band that belongs to Gd^{3+} f - f transition around 240 to 252 nm, and can be associated with the $^8S \rightarrow {}^6D_j$ transitions (C – Fig. 6.4a). These are probably a result of the reduced number of phonons at -263 ^oC (10 K) compared to 27 ^oC (300 K). The suppression of these peaks (C –Fig. 6.4a) at 300 K may also be a result of the overlapping broad bands.

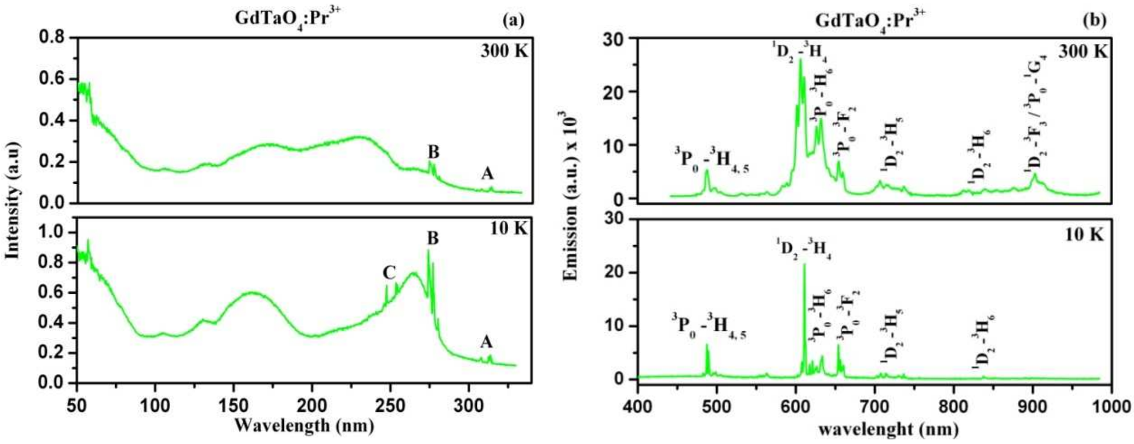

Figure 6.4: Luminescent transitions of Pr^{3+}doped in $GdTaO_4$; excitation (a) and emission (b) spectra

These narrow f - f Gd^{3+} transitions are positioned over a broad band that stretches from 200 to 275 nm, which can be attributed to the excitation of the TaO_4 group charge transfer [13,16]. The absorption edge of $GdTaO_4$ was detected at 225 nm, (Fig 6.3) and this is similar to the data reported in the literature. This implies that the peaks that occur below 225 nm overlap with the conduction band. These transitions may well be those of the 4f5d levels of both Gd^{3+} and Pr^{3+} ions [16,17].

The overall observed emission of the $GdTaO_4:Pr^{3+}$ system corresponds to the transitions of Pr^{3+} (Fig. 6.4b). This indicates that the energy absorbed by Gd^{3+} and the TaO_4 group was transferred to the luminescent centres (Pr^{3+} ions). The energy of the TaO_4 group was probably first transferred to Gd^{3+} through the charge transfer states, and finally to Pr^{3+} ions. The energy transfer taking place between these centres was probably by means of carrier exchange mechanism proposed by G. Blasse and A. Brill [13,16]. The emission peak around 910 nm is probably due to $^1D_2 \rightarrow {}^3F_3$ or/and $^3P_0 \rightarrow {}^1G_4$ transitions, which is prominent at 27 ^oC (300 K) and was quenched at -263 ^oC (10 K). The quenching of this emission may be a result of the strongly induced metal to metal charge transfer at low temperature [15].

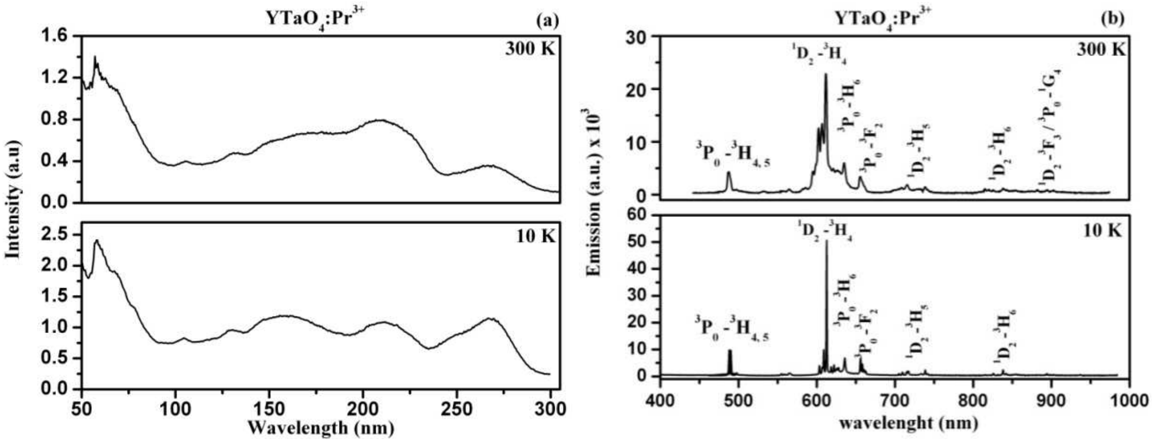

Figure 6.5: Luminescent transitions of Pr^{3+}doped in YTaO$_4$; excitation (a) and emission (b) spectra

The excitation spectra of YTaO$_4$:Pr^{3+} (Fig. 6.5a) is similar to that of GdTaO$_4$:Pr^{3+} with forbidden f-f transitions of Pr^{3+}. The broad excitation band at 225 – 286 nm can be assigned to charge transfer bands of the TaO$_4$ group. This was more prominent at -263 ^{o}C (10 K) probably due to reduced phonon quantity at this low temperature [5,8]. The bands below 225 nm can be assigned to 4f5d levels of Pr^{3+}. The band around 225 – 286 may also be the allowed 4f5d transition of Pr^{3+} which may be estimated using the energy difference equation (Eq. 6.1) proposed by P. Dorenbos [17].

$$\Delta \boldsymbol{E}(\boldsymbol{Pr},\boldsymbol{Ce}) \equiv \boldsymbol{E}(\boldsymbol{Pr},\boldsymbol{A}) - \boldsymbol{E}(\boldsymbol{Ce},\boldsymbol{A}) \qquad [\mathbf{6.1}]$$

The energy difference between the 4f5d levels of trivalent lanthanide ions is constant in any compound $\boldsymbol{A}$. This allows the approximation of the allowed Pr^{3+} 4f5d levels in YTaO$_4$ because the allowed 4f5d level of Ce^{3+} is reported around 410 nm in YTaO$_4$ [15,18]. The overall emission is a result of Pr^{3+} f - f transitions as shown in figure 5b, for acquisition at -263 ^{o}C (10 K) and at 27 ^{o}C (300 K).

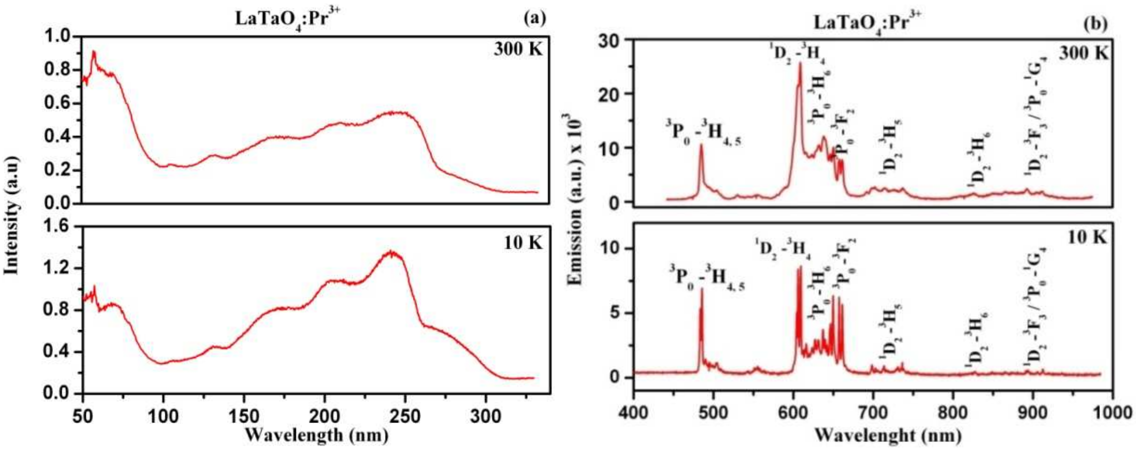

Figure 6.6: Luminescent transitions of Pr^{3+}doped in YTaO$_4$; excitation (a) and emission (b) spectra

LaTaO$_4$ exhibits a different structure compared to the fergusonite systems (GdTaO$_4$ and YTaO$_4$) and the overall emission peaks slightly differ from those of fergusonites (Fig. 6.6b). The excitation spectrum of LaTaO$_4$:Pr^{3+} shows more intense broad excitation bands at -263 ^{o}C (10 K) compared to those at -27 ^{o}C (300 K). The charge transfer of the TaO$_4$ is observed as a broad band around 280 nm (Fig 6.6a), and it matches that obtained in the diffused reflectance spectra (Fig. 6.3), and as also reported in the literature [15].

The $^1D_2 \rightarrow {}^3H_4, {}^3F_2$ and transitions show a clear peak splitting which may be a result of carriers falling to different stark manifolds of $^3H_4$ and $^3F_2$ [19]. The $^3P_0 \rightarrow {}^3F_2$ is more pronounced in the lanthanum matrix as opposed those of the other matrices.

A simplified energy transfer scheme from the TaO$_4$ group either to Gd^{3+} states in GdTaO$_4$:Pr^{3+} system or directly to Pr^{3+} states in LaTaO$_4$:Pr^{3+} and YTaO$_4$:Pr^{3+} systems, is presented in figure 7. According to this illustration, upon excitation the charge transfer as a result of the TaO$_4$ absorption results in an excitonic state which may in turn result in emission in the 300 nm region [13,14]. However when Pr^{3+} is doped in LaTaO$_4$ and YTaO$_4$, some or all of the energy in the excitonic states may be transferred to Pr^{3+} states. The Pr^{3+} 4f → 4f, 4f5d absorption is also taking place, such that the resulting emission is possibly a contribution from Pr^{3+} absorption, excitonic state and host energy transfer to Pr^{3+} states [12,14]. In GdTaO$_4$:Pr^{3+}; Gd^{3+} absorb energy during excitation and the excitonic states also transfer their absorbed energy to Gd^{3+} states, and eventually all the absorbed energy in Gd^{3+} states is transferred to Pr^{3+} states [14]. The resulting emission is a result of transitions in Pr^{3+} states (Fig. 6.4, 6.5 and 6.6).

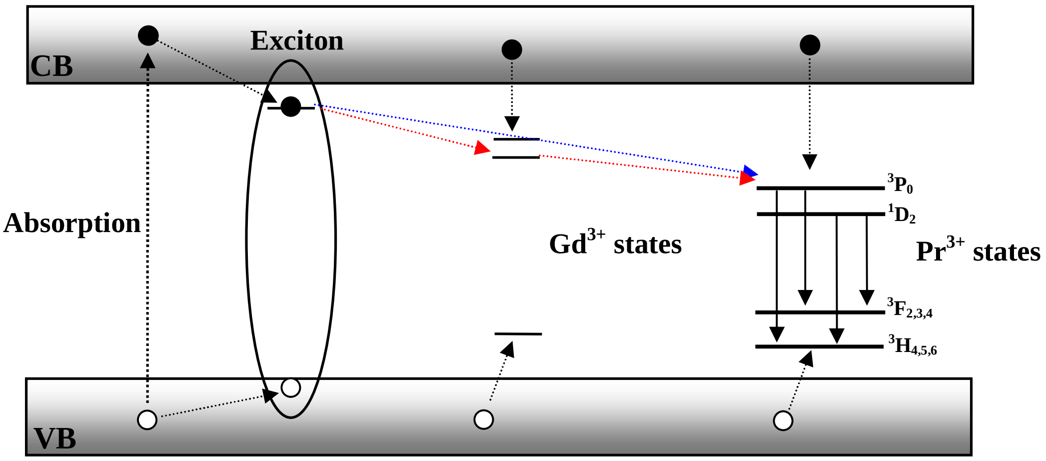

Figure 6.7: Energy transfer scheme between TaO_4, Gd^{3+} state and Pr^{3+} states

The phosphorescent decay curves (Fig. 6.8) of the three rare-earth compounds show that the systems have two components that are responsible for luminescence. The fast component can be attributed to the decaying of the f - f emission of the Pr^{3+}, and the slow component can be attributed to delayed emission as a result of trapping and detrapping of charge carriers. The trap levels may be more than one in this system, and amongst them is the oxygen vacancies ($V_O^{\cdot}$ *or* $V_O^{\cdot\cdot}$) that are responsible for electron trapping [7,20–22].

The effect of oxygen vacancy trapping centres in the phosphors is the observed red afterglow emission that approximately lasted for about 10 min (Table 1). This can be attributed to the trapping and de-trapping of carriers by the trap levels within the forbidden region [7,20]. The curves were fitted with a second order exponential equation (Eq. 6.2) and the decay parameters are presented in table 1.

$$\boldsymbol{I(t) = Ae^{-t/\tau_1} + Be^{-t/\tau_2}} \qquad [\mathbf{6.2}]$$

I(t) is the luminescence intensity, A and B are constants and *t* is the time. The first term on the right side of the equation describes the decay of luminescence from the dopant ion, and whose lifetime is presented by τ_1 (Table 1). The second term describes the rise time of carriers within shallow trap centres, and whose lifetime is presented by τ_2 (Table 1) [22].

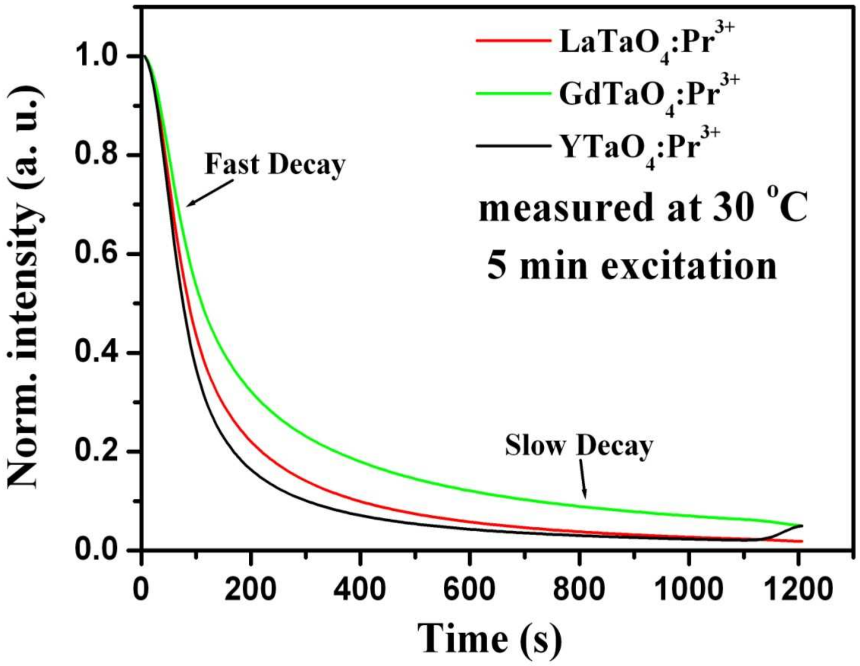

Figure 6.8: Phosphorescent decay curve of (Gd,La,Y)$TaO_4:Pr^{3+}$

Table 1: Decay times τ_1 and τ_2 for the Pr^{3+} doped rare-earth tantalate phosphors.

Compound	τ_1 (secs.)	τ_2 (secs.)	R^2
$GdTaO_4:Pr^{3+}$	64 ± 1	620 ± 63	0.993
$YTaO_4:Pr^{3+}$	77 ± 1	660 ± 31	0.996
$LaTaO_4:Pr^{3+}$	79 ± 1	660 ± 42	0.996

Thermoluminescent (TL) data were recorded from all the samples to evaluate the distribution of the energy traps within their forbidden energy band gap. Many electron traps in phosphorescent materials are attributed to oxygen vacancies, which may assume different orientations and can therefore occupy different levels [23]. The measurements were carried out at 325 °C for

$GdTaO_4:Pr^{3+}$, 300 °C for $YTaO_4:Pr^{3+}$ and 280 °C for $LaTaO_4:Pr^{3+}$ and the heating rate for all the samples was kept at 2 °C/sec.

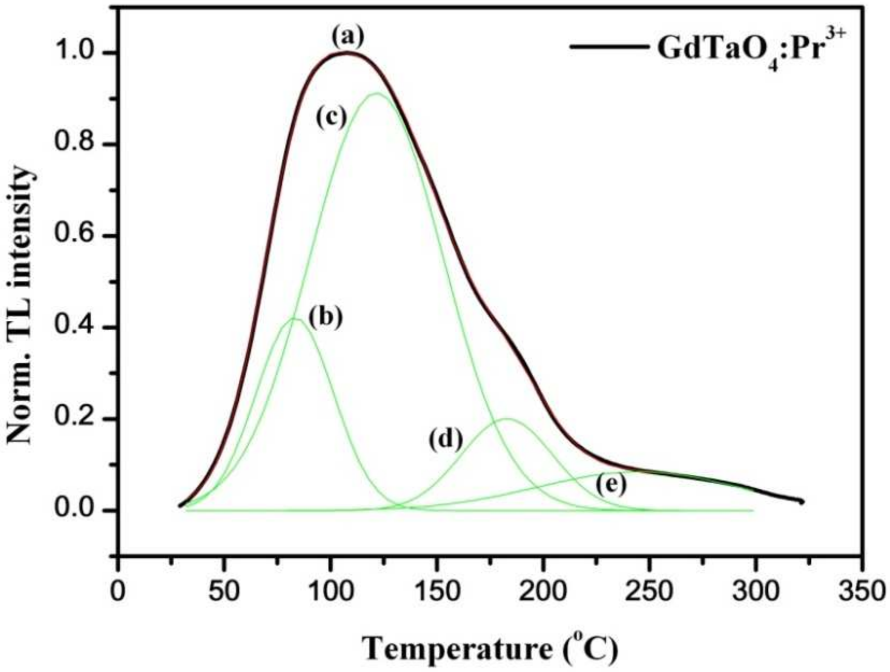

Figure 6.9: TL glow curve of $GdTaO_4:Pr^{3+}$

The glow curves obtained for the different samples were deconvoluted into thermal peaks by Gaussian fitting. The thermal peaks represent the discrete trap levels. The symmetry of $GdTaO_4:Pr^{3+}$ (Fig. 6.9) and $YTaO_4:Pr^{3+}$ (Fig. 6.10) glow curves describes a pair of isolated trap levels, and their depth was approximated using the second order kinetic model (Eq. 6.3) by Chen [25], and the results are presented in table 1.

$$\boldsymbol{E = 3.54\left(\frac{kT_m^2}{\omega}\right) - 2kT_m} \qquad [6.3]$$

$\boldsymbol{E}$ is the trap depth of the measured in eV, $\boldsymbol{k}$ = 1.38×10^{-23} m^2 kg s^{-2} K^{-1} is Boltzmann's constant, T_m is the temperature corresponding to the maxima of a thermal peak, and ω is the FWHM (full width at half maximum) of a thermal peak.

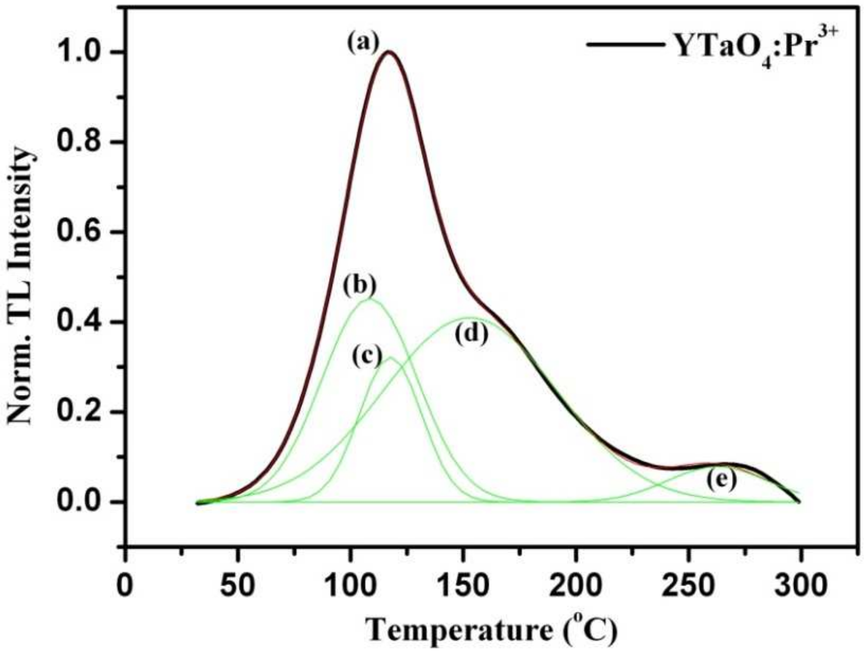

Figure 6.10: TL glow curve of YdTaO$_4$:Pr^{3+}

The trap levels of the perovskite LaTaO$_4$:Pr^{3+} phosphor, were approximated using the first order kinetic model (Eq. 6.4) because the discrete traps that are revealed by the glow curve are not isolated (Fig. 6.11) [25].

$$\boldsymbol{E = 2.52\left(\frac{kT_m^2}{\omega}\right) - 2kT_m} \qquad [\mathbf{6.4}]$$

The calculated full values of $\boldsymbol{\omega}$ (with $\boldsymbol{\omega_j}$ = b,c,d or e describing the thermal peaks) and $\boldsymbol{E}$ for LaTaO$_4$:Pr^{3+} are listed in table 2. The glow curve of LaTaO$_4$:Pr^{3+} consists of three thermal peaks, as opposed to the fergusonites (GdTaO$_4$:Pr^{3+} and YTaO$_4$:Pr^{3+}) which were deconvoluted into four thermal peaks. This may be due to different trap distribution because of the different structures of these compounds.

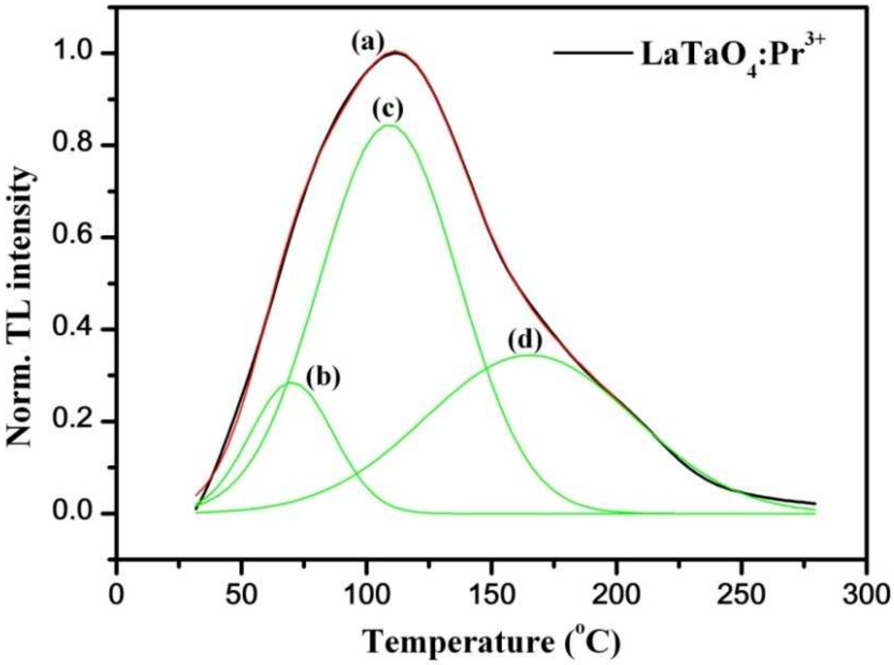

Figure 6.11: TL glow curve of $LaTaO_4:Pr^{3+}$

The broadening and the appearance of the peak shoulders in the glow curves is a result of emission coming from overlapping trap levels, which correspond to the peak positions of the deconvolution peaks (thermal peaks) of the main peak (glow curve) [26]. Numerous trap levels that have a very close energy distribution in the forbidden region of the tantalate phosphors may be responsible for the long afterglow because of trapping and de-trapping of carriers (electrons) from one level to another as they make their way to the luminescent centre [20-22].

As presented in the simplified energy level diagram in figure 6.12, the trapping centres are overlapping because of their close energy distribution as suggested by the glow curves (Fig. 9, 10 &11), which resemble a broad peak with several shoulders. The shoulders are attributed to a contribution from several peaks [24]. The electrons from such a system upon applying thermal energy jump from one trap level to another situated above it, and then finally to the conduction band [27]. The glow curves of $GdTaO_4:Pr^{3+}$ and $YTaO_4:Pr^{3+}$ (Fig. 9 & 10) resemble an isolated peak around 270 °C which can be attributed to electrons jumping from a deep trap centre straight into the conduction band [27].

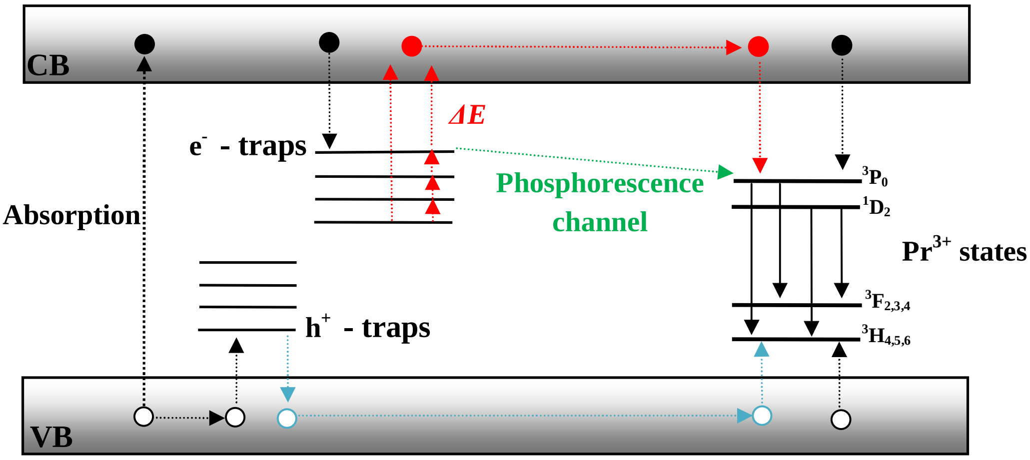

Figure 6.12: Energy level presentation of thermoluminescence process

The electrons that jump into the conduction band eventually fall into the luminescent centre resulting in observed TL emission. In the absence of thermal energy, some trapped electrons may gradually jump off from the trap centres and fall to the luminescent centres at room temperature. The resulting trapping and detrapping is responsible for the afterglow of the phosphors [20-22, 27].

Table 2: TL parameters of the rare-earth tantalate phosphors doped with Pr^{3+} ions

Compound	ω_b	ω_c	ω_d	ω_e
$GdTaO_4:Pr^{3+}$	37	63	43	95
E (eV)	***1.02***	***0.71***	***1.48***	***0.83***
$YTaO_4:Pr^{3+}$	42	28	77	44
E (eV)	***1.02***	***1.60***	***0.68***	***1.43***
$LaTaO_4:Pr^{3+}$	78	55	83	
E (eV)	***0.75***	***0.55***	***0.46***	

6.4. Conclusion

Pr $^{3+}$orthotantale phosphors were prepared in the presence of Li_2SO_4 fuel to improve the reaction rate. The compounds exhibited multiphases as observed from the XRD data. Pr^{3+} emission from $GdTaO_4:Pr^{3+}$, $YTaO_4:Pr^{3+}$, and $LaTaO_4:Pr^{3+}$ was observed in the blue-green region and was attributed to $^3P_0 \rightarrow {}^3H_{4,5,6}, {}^3F_2, {}^1G_4$ and $^1D_2 \rightarrow {}^3H_{4,5,6}$, $^3F_3$ transitions. The phosphorescence lifetime (**τ**) observed from these compounds as a result of shallow oxygen vacancy traps were 620 s for $GdTaO_4:Pr^{3+}$, 655 s for $YTaO_4:Pr^{3+}$ and 663 s for $LaTaO_4:Pr^{3+}$. The energy distribution of the oxygen vacancies that act as trap levels was approximated using the TL spectroscopy.

6.5. Reference

[1] L.H. Brixner, H.Y. Chen, Chemical Etching Characteristics **130** (1983) 2435.

[2] C.W.E. v. Eijk, Nuclear Instruments and Methods in Physics Research A **460** (2001) 1.

[3] A. Garcia-Murillo, C.L. Luyer, C. Dujardin, T. Martin, C. Garapon, C. Pedrini, J. Mugnier, Nuclear Instruments and Methods in Physics Research A **486** (2002) 181.

[4] L. Bo, H. Kun, X. Liu, M. Gua, S. Huanga, N. Chen, Z. Qib and G. Zhang, Solid. Stat. Comm. **144** (10-11) (2007) 484

[5] L.L. Noto, S.S. Pitale, J.J. Terblans, O.M. Ntwaeaborwa and H.C. Swart, Physica B: Physics of Condensed Matter, (2011), doi:10.1016/j.physb.2011.09.075

[6] M. Nyman, M.A. Rodriquez, T.M. Alam, T.M. Anderson, A. Ambrosini, Chem. Mater. **21** (2009) 2201

[7] E.J. Popovici, M. Nazarov, L. Muresan, D.Y. Noh, E. Bica, M. Morar, I. Arellano, E. Indrea, Phys. Proc. **2** (2009) 185

[8] E.J. Popovici, M. Nazarov, L. Muresan, D.Y. Noh, L.B. Tudoran, E. Bica, E. Indrea, J. Alloys Compd. **497** (2010) 201

[9] I.D. Arellano, M. Nazarov, D.Y. Noh, Revista Colombiana de Fisica, **41** (1), (2009)

[10] P. Maillard, F. Tessier, E. Orhan, F. Chevire, R. Marchand, Chem. Mater. **17** (2005) 152

[11] G. Gasparotto, N.M. Nascimento, M.A. Cebin, J.A. Zaghette, J. Alloys Compd. **509** (2011) 9076

[12] M. Gu, X.X. Xu, X. Liu, L. Qiu and R. Zhang, J. Sol-gel Sci. Tech. **35** (2005) 193

[13] B.O. Li, Z. Gu, J. Lin, M.Z. Su, J. Mater. Sci. **35** (2000)1139

[14] A. Hristea, E.J. Popovici, L. Muresan, M. Stefan, R. Grecu, A. Johnsson, M. Boman, J. Alloys. Compd. **471** (2009) 524

[15] M. Nyman, M.A. Rodriguez, L.E.S. Rohwer, J.E Martin, M. Waller, F.E. Osterloh, Chem Mater. **21** (2009) 4731

[16] G. Blasse and A. Bril, J. Lumin **3** (1970) 109

[17] P. Dorenbos, J. Lumin. **87 – 89** (2000) 970

[18] P. Dorenbos, J. Lumin. **91** (2000) 155

[19] P. Boutinaud, E. Pinel, M. Dubois, A.P. Vink, R. Mahiou, J. Lumin. **111** (2005) 69

[20] B.J. Nyman, M.E. Bjorketun, G. Wahnstrom, J. Sol. Stat. Ionics **189** (2011) 19

[21] P.J. Deren, R. Pazik, W. Strek, P. Bautinaud, R. Mahiou, J. Alloy Compd. **451** (2008) 595

[22] P.T. Diallo, P. Boutinaud, R. Mahiou, J.C. Cousseins, J. Phys. Stat. Sol. (a) **160** (1997) 255

[23] W. Jia, D. Jia, T. Rodriguez, D.R Evans, R.S. Meltzer, W.M. Yen, J. Lumin. **119-120** (2006) 13

[24] X. Zhang, C. CaO, C. Zhang, S. Xie, G. Xu, J. Zhang, X.J. Wang, Mater. Res. Bull. **9** (2010) 22

[25] R. Chen, J. Appl. Phys. **40** (1969) 570

[26] S.K. Sharma, S.S. Pitale, M.M. Malik, R.N. Dubey, and M.S. Qureshiphys, stat. sol. (a) **205** (11), (2008) 2695

[27] L. Weng, Z. Xu, F. Teng, W. Jiang, F. Zhang, L Meng, J. Rare Earth. **23** (6), (2005) 672

7

CL emission degradation of rare earth tantalate phosphors

7.1 Introduction

Up to now reddish-orange $Y_2O_3:Eu^{3+}$ phosphor with CIE coordinates of (0.64, 0.36), is one of the widely industrially accepted red phosphors for television displays because of its sharp intense line emission surpasses that of many red emitting phosphors. However there are expensive adaptations required to improve the colour rendering index of $Y_2O_3:Eu^{3+}$ to make it more reddish, such as filtering which is relatively expensive to achieve [1,2,3]. Such special requirements may have lead to expensive prices of devices that are made of phosphors that glows with natural red colour.

On the other hand, Pr_6O_{11} has emerged as a relatively cheap compound and when combined with compounds like $CaTiO_3$, red emitting $CaTiO_3:Pr^{3+}$ phosphor can be produced cost effectively. The red emission from $CaTiO_3:Pr^{3+}$ has (0.680, 0.311) CIE coordinates that are close to those of ideal red (0.630, 0.33) [2,3,4,5,6]. It is therefore likely that Pr^{3+} doped phosphors can emerge as future generation of phosphors glowing with an ideal red emission that may be useable in field emission displays (FED). Phosphors that are used in television display devices such as FEDs must have specific adaptations that will allow them to withstand the necessary operating conditions. Such adaptations include surface chemical stability that will make them resistant to low voltage electron beam irradiation ageing [7,10,11].

According to a widely reported electron stimulated surface chemical reaction (ESSCR) mechanism, prolonged exposure of phosphors to electron beam during normal operation of phosphor coated display screen can dissociate the phosphor into reactive species and a subsequent formation of new compound detrimental to the CL intensity. That is, electron beam induced surface dissociation is followed by formation of oxide layers as well as creation of point defects at the interface between the surface and the phosphor and these are known to cause drastic degradation of the CL intensity [7,10,11,12].

In this study, the surface chemical stability and the CL intensity degradation of red emitting (Y,Gd,La)TaO_4:Pr^{3+} phosphors were investigated using Auger Electron Spectroscopy (AES). The cathodoluminescence (CL) intensity degradation and surface chemical changes were monitored simultaneously during a prolonged electron beam irradiation. In addition, the chemical and electronic states of these materials, as well as oxide layers that were possibly formed during the electron irradiation were investigated by using X-ray Photoelectron spectroscopy (XPS).

7.2. Experimental

The samples were prepared by directly firing Ta_2O_5 with Gd_2O_3, La_2O_3 or Y_2O_3, and adding $PrCl_3$ to each reaction, to obtain $Gd_{0.995}TaO_4$:$0.005Pr^{3+}$, $La_{0.995}TaO_4$:$0.005Pr^{3+}$ or $Y_{0.995}TaO_4$:$0.005Pr^{3+}$. Li_2SO_4 flux was used to facilitate the reaction, according to the chemical reaction put forward by Hristea *et al* [14]. The phases were identified using a Bruker AXS D8 Advance X-ray diffractometer (XRD). The synthesized phosphor materials were subjected to prolonged electron beam irradiation to investigate their surface chemical changes *in-situ* at 1×10^{-6} O_2 using AES (PHI 549) system with an electron beam of 2 keV and 10 μA beam current to probe the surface of the specimen.

The CL data were collected at an angle of 60^o to the incident electron beam using Ocean Optics S2000 spectrometer. The emission peaks at 484 and 613 nm were monitored for the electron dose range of 0-900 C/cm^2. The surface chemical state was investigated with a PHI 5000 *Versa-probe* XPS system before and after electron bombardment using a 100 μm, 25 W, 15 kV Al monochromatic x-ray beam ($h\nu = 1486.6$ eV) to uncover the chemical changes that took place during the electron irradiation. For higher resolution spectra, the hemispherical analyzer pass energy was maintained at 11.8 eV. Measurements were performed using either a 1 eV/step and 45 min. acquisition times (binding energies ranging from 0-1400 eV) for survey scans or a 0.1 eV/step and 20-30 min. acquisition times for the high resolution scans.

7.3. Results and Discussion

Orthotantalates are compounds that require temperatures above 1400 °C to yield a pure phase. However they can also be prepared at low temperatures using flux agents to fuel the reactions, and the resulting product may also have impurity phases [15,16]. Figure 1 presents XRD patterns of $YTaO_4:Pr^{3+}$ (Fig. 7.1a), $LaTaO_4:Pr^{3+}$ (Fig. 7.1b) and $GdTaO_4:Pr^{3+}$ (Fig. 7.1c). The patterns show successful formation of these compounds when referenced to ICSD standard patterns, and there are small impurities from unreacted reagents as indicated with asterisks (*).

The overall emission of tantalate based phosphors that are doped with rare-earth ions may be a combined contribution coming from the host and rare-earth luminescent centres as reported by Pitale et al [11]. Where the host emission is attributed to $O^{2-}\rightarrow Ta^{5+}$charge transfer upon excitation and a subsequent emission of visible light. The luminescent center of $(Y,Gd,La)TaO_4$ is excitable with a 245 nm wavelength photon [13].

Figure 7.2 presents the CL emission of $(Y,Gd,La)TaO_4$ phosphors doped with Pr^{3+} ions, from which only emission coming from Pr^{3+} luminescent centres is observable. The emission is a result of different transitions that arise upon electron relaxation from $^3P_0$ and $^1D_2$ states to the $^3F_2$ and $^3H_{4,5,6}$ states, giving out blue and red emissions around the 485 nm region and the 610 – 725 nm region, respectively.

Difference in the Pr^{3+} emission intensity of the $^3P_0 \rightarrow {}^3H_4$ and $^1D_2 \rightarrow {}^3H_4$ for $GdTaO_4:Pr^{3+}$, $LaTaO_4:Pr^{3+}$ and $YTaO_4:Pr^{3+}$ was observed. Figure 2 shows the blue emission coming from $^3P_0 \rightarrow {}^3H_4$ transition to be relatively more intense than the red emission from the $^1D_2 \rightarrow {}^3H_4$ transition under electron beam irradiation of $LaTaO_4:Pr^{3+}$ and relatively equal for $GdTaO_4:Pr^{3+}$ while the red emission is dominant over the blue emission in $YTaO_4:Pr^{3+}$ [2].

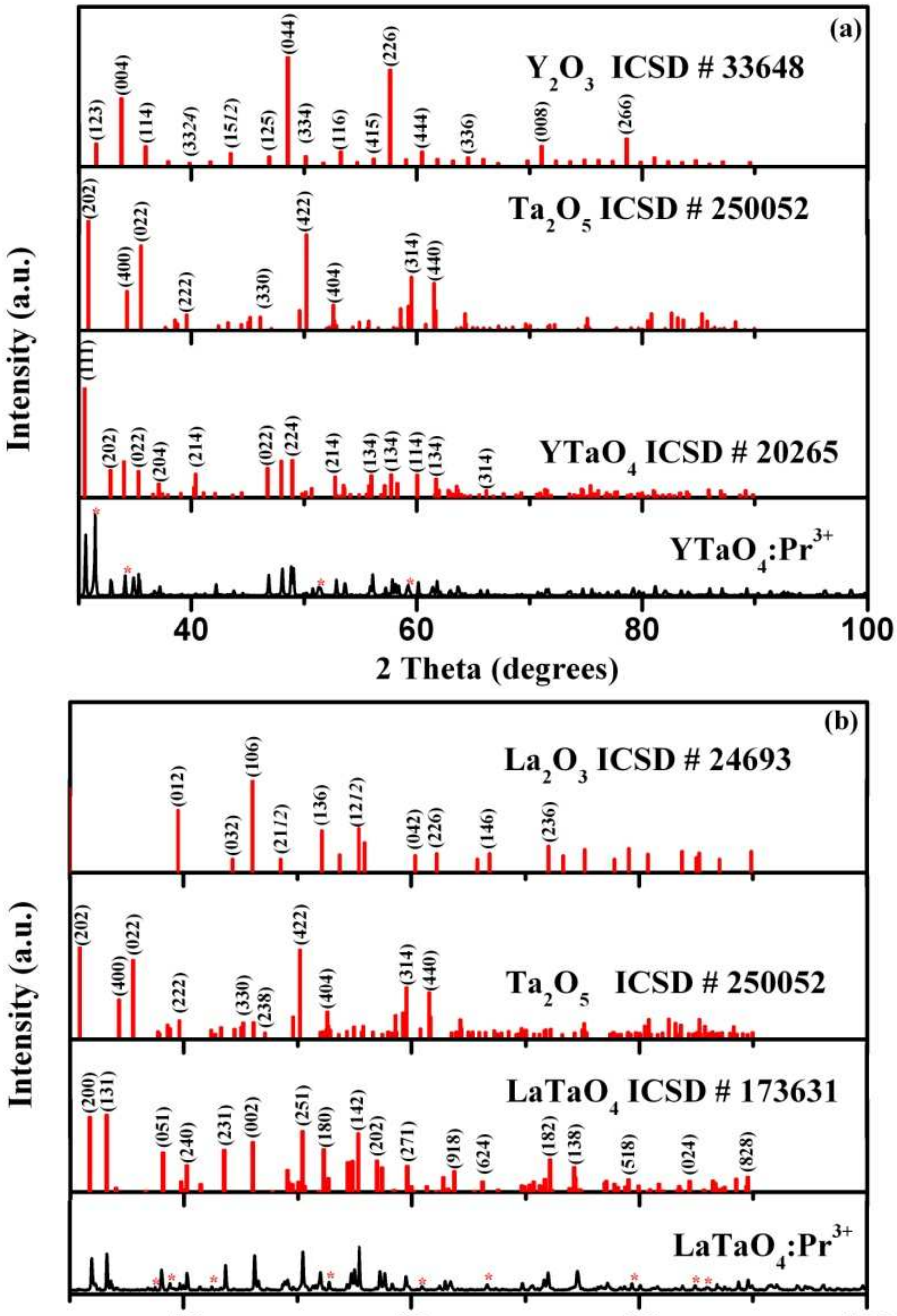
(a)
Y2O3 ICSD # 33648
(123) (004) (114) (3324) (1512) (125) (044) (334) (116) (415) (226) (444) (336) (008) (266)
Ta2O5 ICSD # 250052
(202) (400) (022) (222) (330) (422) (404) (314) (440)
YTaO4 ICSD # 20265
(111) (202) (022) (204) (214) (022) (224) (214) (134) (134) (114) (134) (314)
YTaO4:Pr3+
Intensity (a.u.)
40
60
80
100
2 Theta (degrees)
(b)
La2O3 ICSD # 24693
(012) (032) (106) (2112) (136) (1212) (042) (226) (146) (236)
Ta2O5 ICSD # 250052
(202) (400) (022) (222) (330) (238) (422) (404) (314) (440)
LaTaO4 ICSD # 173631
(200) (131) (051) (240) (231) (002) (251) (180) (142) (202) (271) (918) (624) (182) (138) (518) (024) (828)
LaTaO4:Pr3+
Intensity (a.u.)
40
60
80
100
2 Theta (degrees)

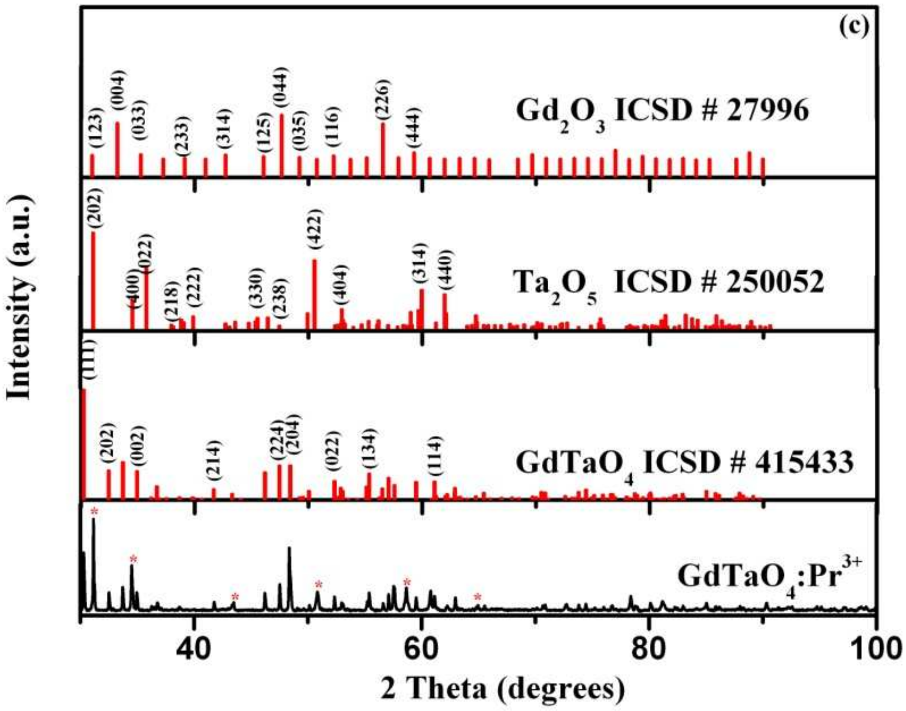

Figure 7.1: XRD patterns of (Y,La,Gd)TaO$_4$:Pr^{3+}

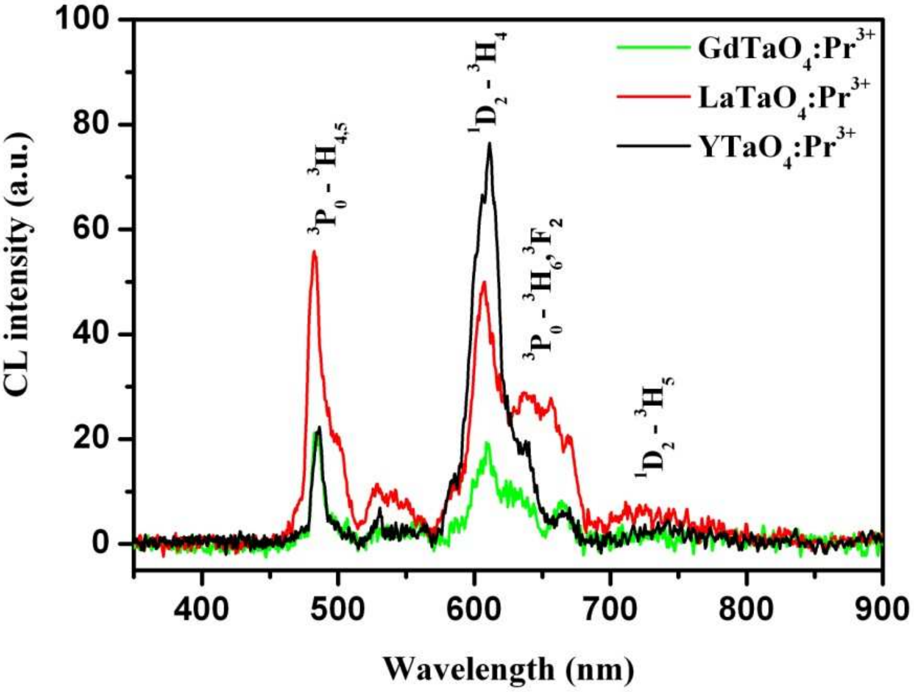

Figure 7.2: CL emission spectra of (Y,La,Gd)TaO$_4$:Pr^{3+}

The surface of the phosphors was subjected to a prolonged electron beam irradiation *in-situ* in an O_2 environment of 1 x 10^{-6} Torr, and the surface elemental changes were monitored by an Auger peak to peak height (APPH) profile. As proposed by Swart et al [12] in the ESSCR mechanism, the electron beam has the ability to dissociate the chemical species present in the vacuum chamber of the Auger spectrometer, such as, H_2O and O_2. Along with the sample surface dissociation, the resulting reactive species O^- that are formed during gas dissociation on the surface may change the surface chemical state. The Auger spectra of $(Y,La,Gd)TaO_4:Pr^{3+}$ are presented in figure 7.3 showing the chemical/elemental composition on the surface of the phosphors before and after the CL degradation process.

A prominent feature in all the Auger spectra is that after the degradation process, almost all adventitious carbon (C) and sulphur (S) species were depleted from the surface and the Y, La, Gd and Ta low energy peaks were more prominent. The CL intensity of the 613 nm emission of $YTaO_4:Pr^{3+}$ increased and stabilized when O stabilized (Fig. 7.4a). Within 100 $C.cm^{-2}$ electron doses on the surface of $LaTaO_4:Pr^{3+}$ (Fig. 7.4b), La and O increased on the surface and S desorbed.

Within this interval, the CL intensity of the 484 nm emission slightly decreased and began to stabilize. The decrement may be a result of surface oxidation as reported by Noto et al [10].
The APPH profile of $GdTaO_4:Pr^{3+}$ shows that O is continuously increasing on the surface and this may be attributed to the O_2 background in the chamber [10]. During the degradation process of $GdTaO_4:Pr^{3+}$ the CL intensity of both red and blue emission remained stable. This may be attributed to the oxide formed on the surface during degradation or because of the impurity oxide phases that did not react, as per the role of oxides in preventing CL loss as reported by Pitale et al [11].

The electron stimulated surface chemical reaction (ESSCR) taking place on the surface during the degradation has an effect of changing the surface chemical state by forming addition species. The newly formed species are often non-luminescent and their formation is accompanied by defect layer situated at the interface between the new non-luminescent layer and the phosphor layer. The defect layer has a detrimental effect on the luminescent intensity [7,10,12].

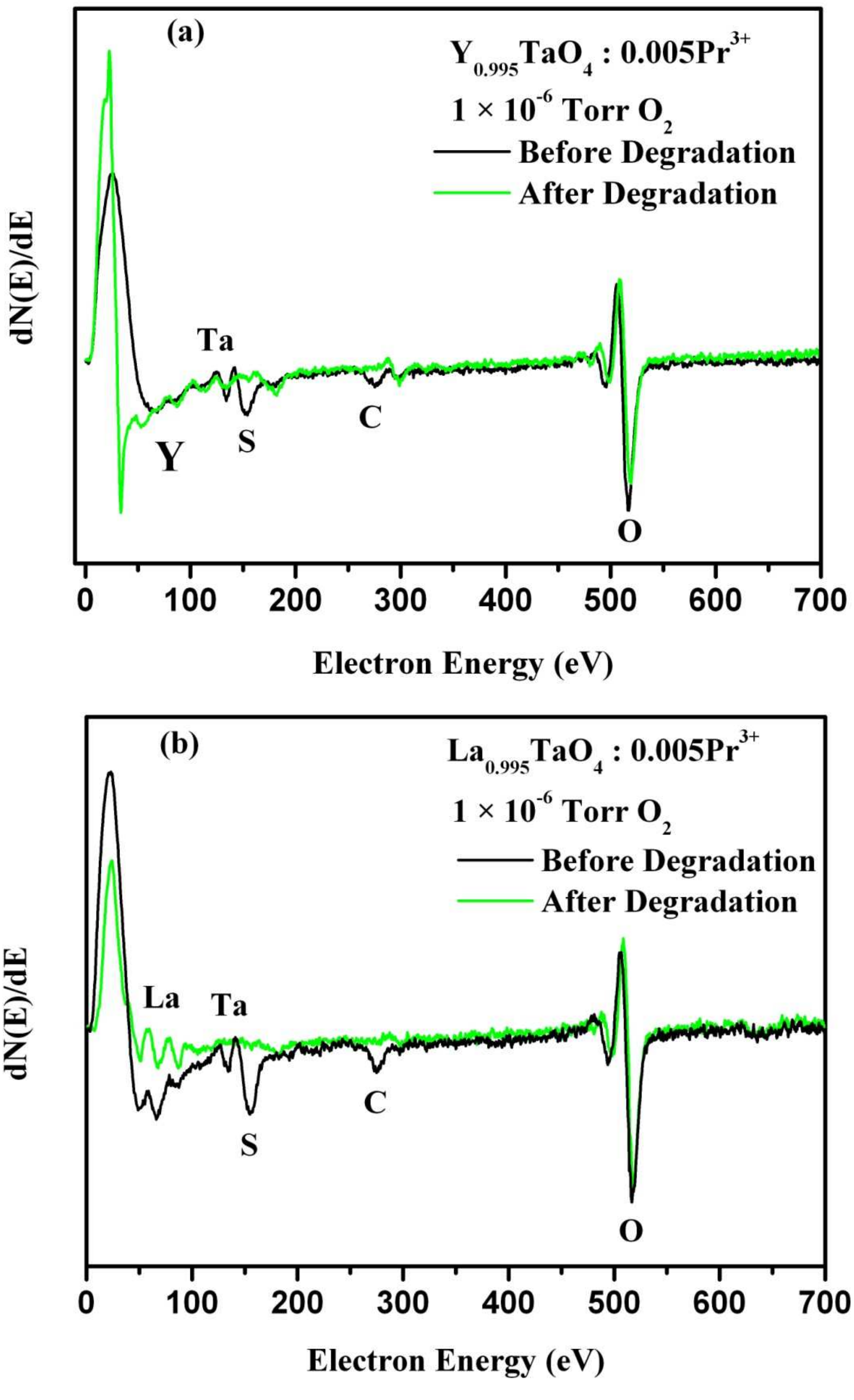
(a)
$Y_{0.995}TaO_4$: 0.005Pr^{3+}
1 × 10^{-6} Torr O_2
Before Degradation
After Degradation
dN(E)/dE
Ta
Y
S
C
O
0
100
200
300
400
500
600
700
Electron Energy (eV)
(b)
$La_{0.995}TaO_4$: 0.005Pr^{3+}
1 × 10^{-6} Torr O_2
Before Degradation
After Degradation
dN(E)/dE
La
Ta
S
C
O
0
100
200
300
400
500
600
700
Electron Energy (eV)

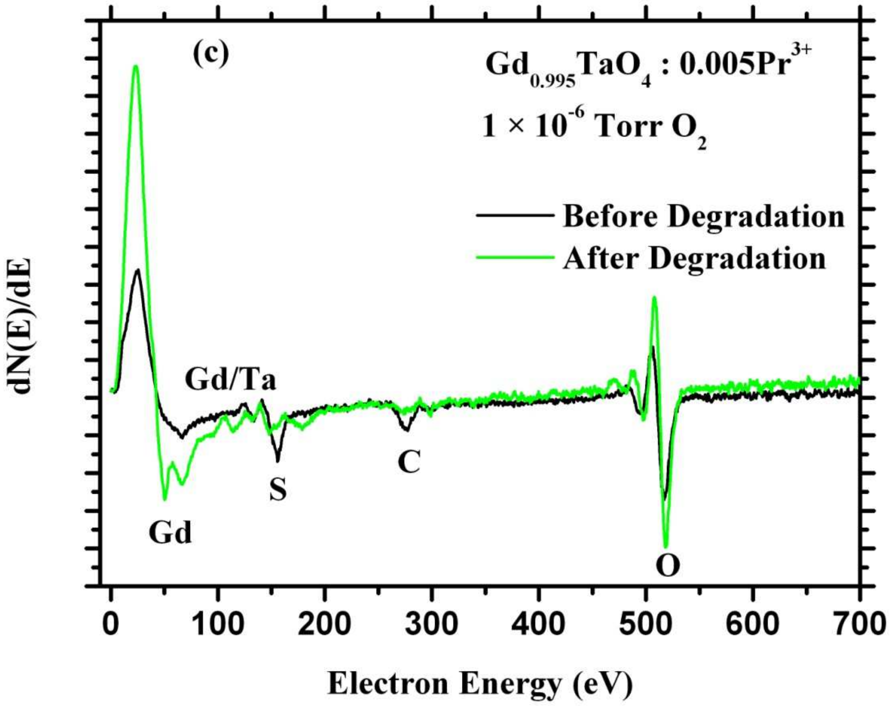

Figure 7.3: AES spectra of (Y,La,Gd)TaO_4:Pr^{3+} before and after electron bombardment.

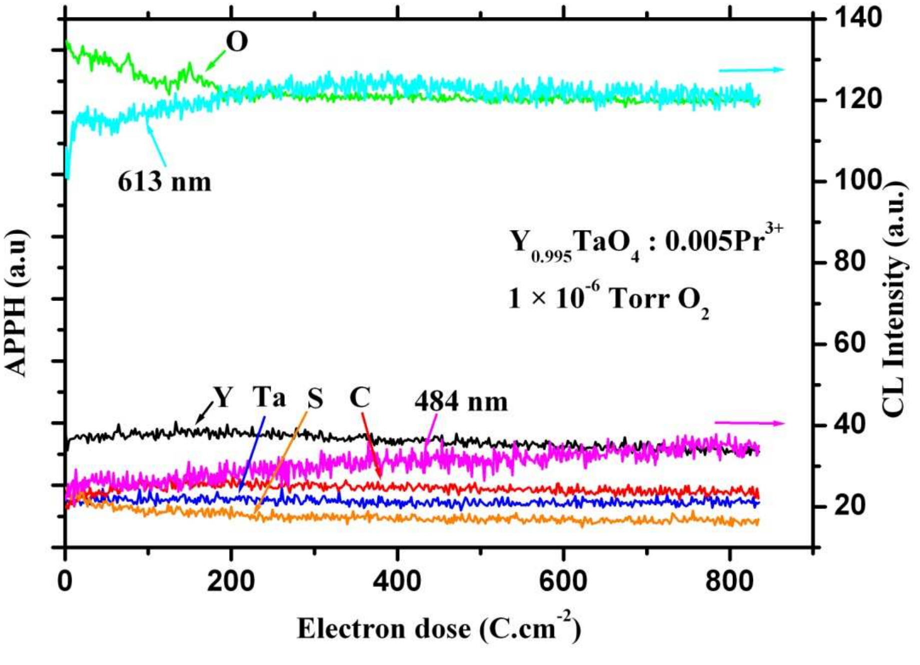

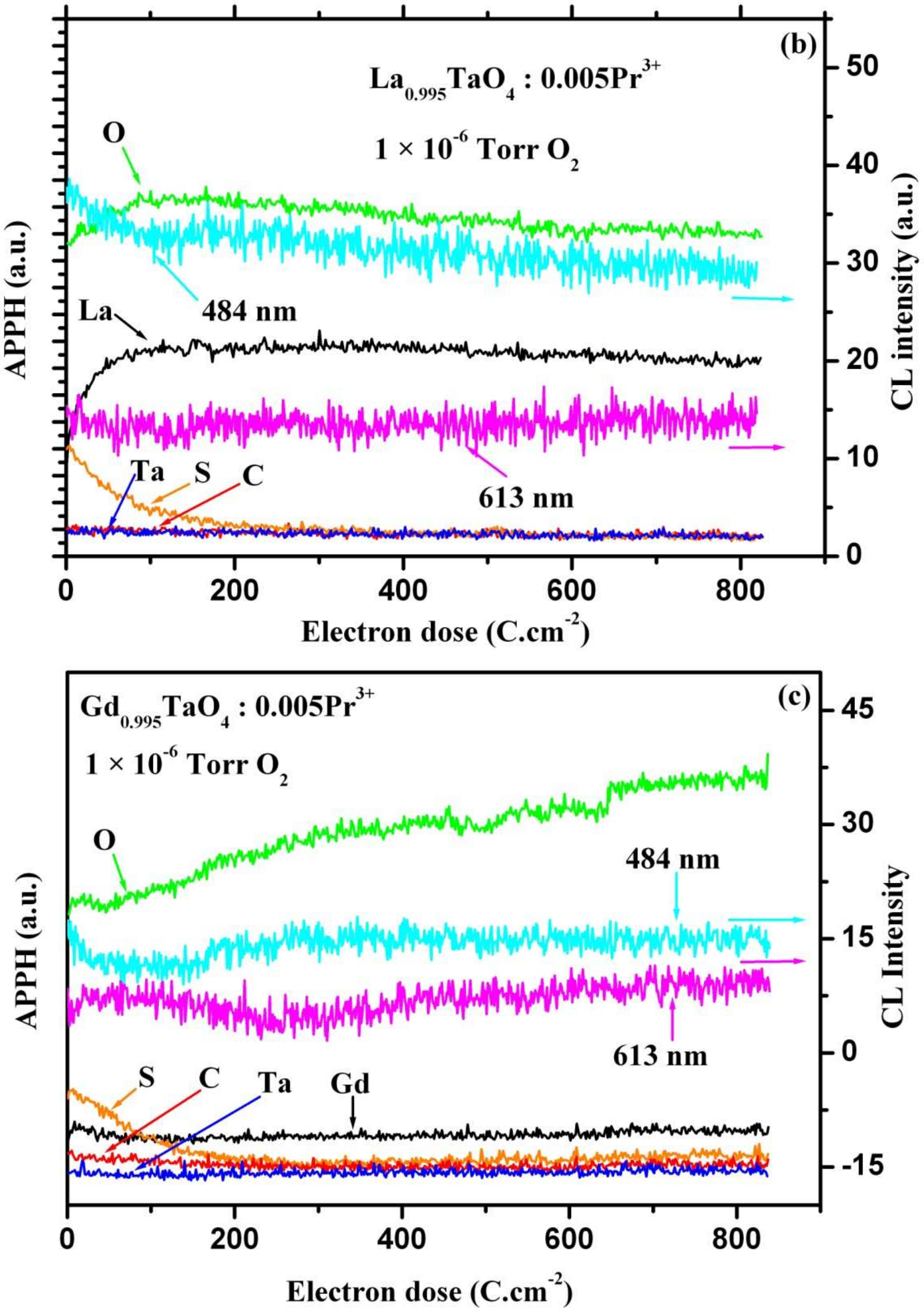

Figure 7.4: CL degradation profile of (Y,La,Gd)TaO$_4$:Pr^{3+}

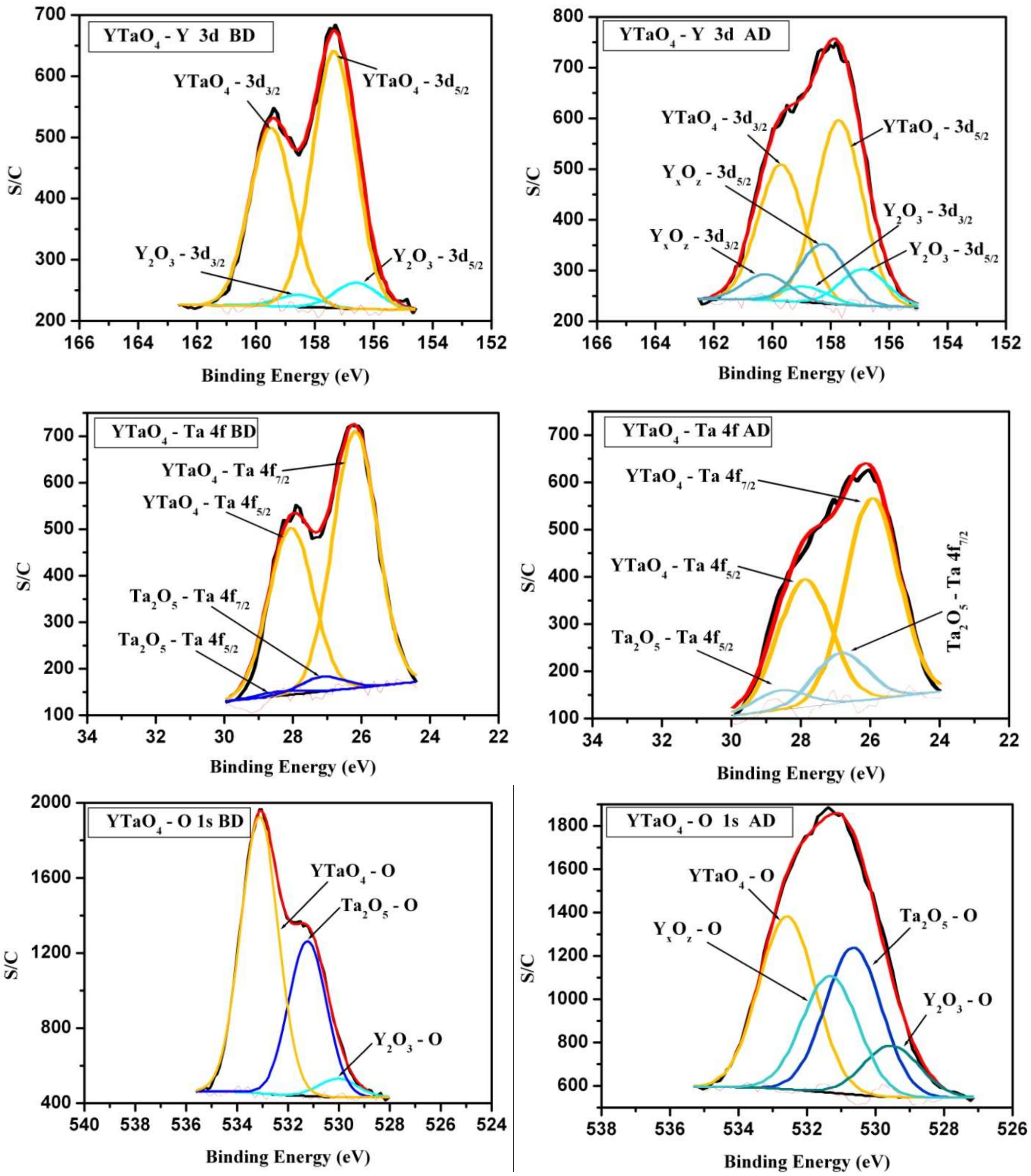

Figure 7.5: $YTaO_4:Pr^{3+}$ spectra before and after degradation

XPS analysis was performed on the surface of $(Y,La,Gd)TaO_4:Pr^{3+}$ before and after degradation to further investigate the chemical changes that took place on the surface during the electron

beam irradiation period. The XPS analysis of $GdTaO_4$ was done and the revealed information was not satisfying and will further be investigated. Hence it is not part of the thesis.
As observed on the phosphors after degradation, the spot where the electron beam had impinged on the surface was marked by a dark layer, which is exactly where XPS analysis was performed. The dark layer is a result of the burning effect that is induced by the electron beam interaction with the surface of the sample [8,9]. XPS results of $YTaO_4:Pr^{3+}$ are presented in figure 7.5 for both undegraded and degraded phosphors as BD (before degradation) and AD (after degradation), respectively. In the spectra are binding energy positions of Y – 3d, Ta – 4f and O – 1s before and after degradation including that of the oxide that was formed after the degradation process.

The 3d and 4f peaks are split into two components, $3d_{3/2}$ and $3d_{5/2}$, and $4f_{5/2}$ and $4f_{7/2}$, respectively as a result of spin-orbit coupling [17]. The Y peak (BD) is deconvulated into 4 peaks, at 158.6 eV ($3d_{3/2}$) and 156.6 eV ($3d_{5/2}$) binding energies that are a contribution from Y_2O_3 [18]. Y_2O_3 may be present on the surface as an unreacted species during the preparation of $YTaO_4$ as revealed by XRD (Fig. 7.1). The other two peaks at 159.6 eV ($3d_{3/2}$) and 157.5 eV ($3d_{5/2}$) binding energies can be attributed to $YTaO_4$, which is the main compound, according to the XPS fitting. As far as the literature is concerned, this is the first report on the peak position of $YTaO_4$ binding energy positions.

The XPS spectra of $YTaO_4$ (Fig 7.5) after degradation (AD) reveals an additional oxide species that has its binding energy peak positions at 160.1 eV ($3d_{3/2}$) and 158.2 eV ($3d_{5/2}$), refer to as Y_xO_z with $0<X<2$ and $0<Z<3$. The Ta peak is also deconvoluted into 4 peaks before degradation (BD), with contribution coming from Ta in Ta_2O_5 at peak positions 28.9 eV ($4f_{5/2}$) and 27.0 eV ($4f_{7/2}$) [20] and $YTaO_4$ at 27.9 eV ($4f_{5/2}$) and 26.0 eV ($4f_{7/2}$). After degradation, the contribution from $YTaO_4$ is reduced because there is more of Ta_2O_5 forming on the surface as a result of the electron beam irradiation.

The O 1s spectra (Fig 7.5) before degradation (BD) consist of peaks at 529.3, 530.6 and 532.7 eV which were assigned to oxygen atoms in Y_2O_3 [17], Ta_2O_5 [20] and $YTaO_4$, respectively. After degradation (AD) there is an emerging peak that is attributed to Y_xO_z at 531.3 eV. The oxygen peak after degradation suggests an increment of oxygen atom contribution from Ta_2O_5

and Y_2O_3. This compliments the suggestion of the increment observed from Ta and Y peaks after degradation.

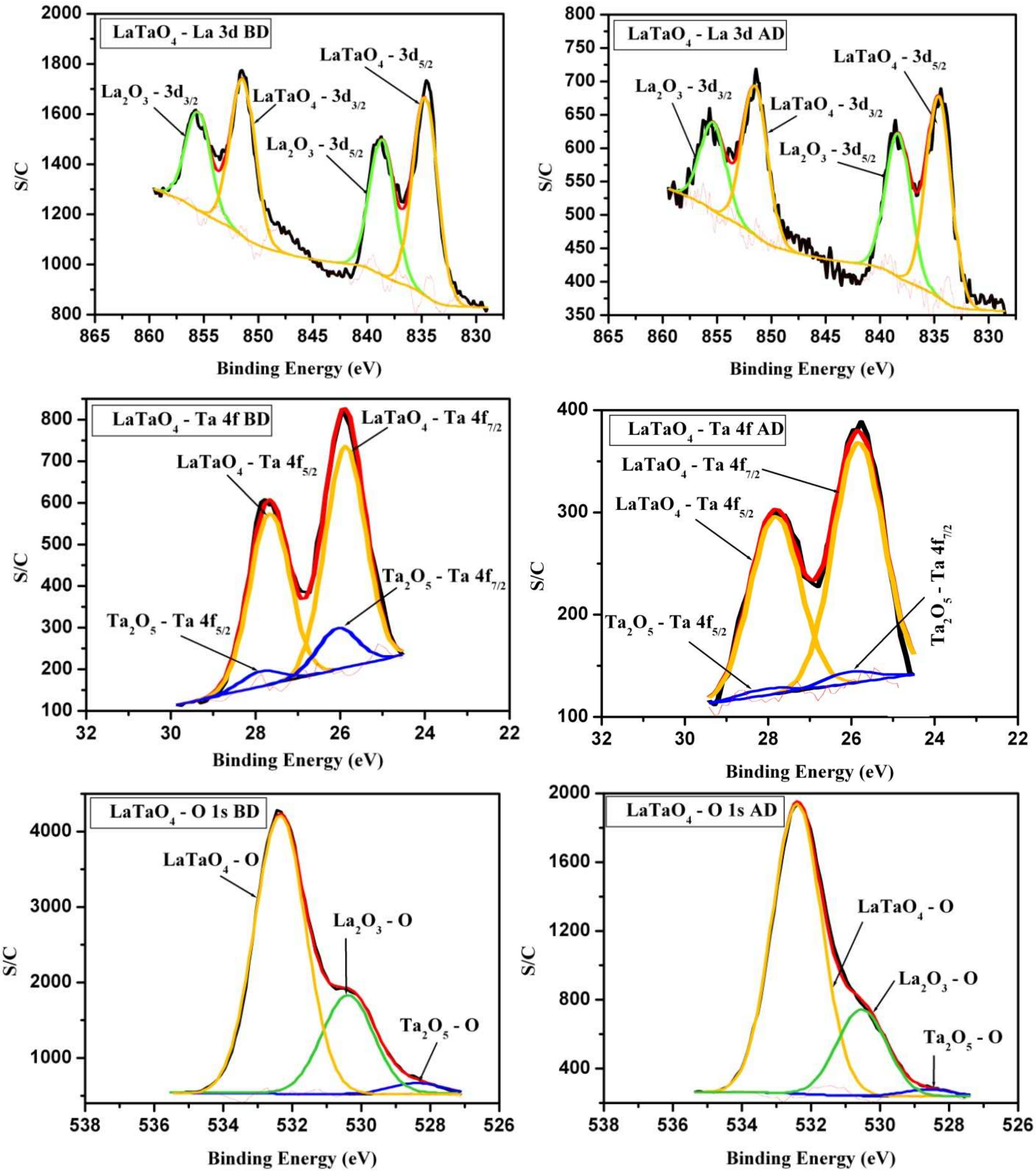

Figure 7:6 $YTaO_4:Pr^{3+}$ spectra before and after degradation

Figure 7.6 shows the surface chemical state analysis of $LaTaO_4:Pr^{3+}$ before and after degradation process. As per XRD (Fig. 7.1) analysis of $LaTaO_4:Pr^{3+}$, the main compound ($LaTaO_4$) is accompanied by impurities on the surface too. The spectra show La – 3d, Ta – 4f and O – 1s peak contribution in $LaTaO_4:Pr^{3+}$ before and after the degradation process. La(3d) state is split into $3d_{3/2}$ and $3d_{5/2}$ states.

The La peak (Fig. 7.6) before degradation (BD) is deconvoluted into 4 peaks, which are a contribution from La_2O_3 at 855.4 eV ($3d_{3/2}$) and 838.6 eV ($3d_{5/2}$) [24], and $LaTaO_4$ at 851.4 eV ($3d_{3/2}$) and 834.5 eV ($3d_{5/2}$). The peak positions of $LaTaO_4$ are also not available in the literature and hence we proposed new positions.

The Ta (Fig. 7.6) peak before degradation (BD) has a contribution coming from Ta in Ta_2O_5 at peak positions 27.9 eV ($4f_{5/2}$) and 26.0 eV ($4f_{7/2}$) [25] and $LaTaO_4$ at 27.7 eV ($4f_{5/2}$) and 25.8 eV ($4f_{7/2}$). In both the degraded and the undegraded sample, the $LaTaO_4$ contribution dominates on the surface, and the Ta_2O_5 peak reduces after degradation

The O 1s spectra (Fig. 7.6) before degradation (BD) consists of peaks at 528.4, 530.3 and 532.3 eV which come from oxygen atoms in Ta_2O_5 [26], La_2O_3 [27] and $GdTaO_4$, respectively. The oxygen peak after degradation (AD), supports the peak contribution changes that are observed in the La and Ta peaks. It is clear that the surface was stable in this case and no species were formed.

7.4. Conclusion

$MTaO_4:0.5Pr^{3+}$ (M = Gd, La and Y) phosphors were prepared by solid state reaction at 1200°C for 4h in the presence of Li_2SO_4, acting as a flux agent. The phase of the phosphors was successfully achieved as confirmed by XRD, and the CL showed equal contribution of emission intensity from ${}^3P_0 \rightarrow {}^3H_4$ and ${}^1D_2 \rightarrow {}^3H_4$ transitions of Pr^{3+} in $GdTaO_4:Pr^{3+}$, more contribution from ${}^1D_2 \rightarrow {}^3H_4$ than ${}^3P_0 \rightarrow {}^3H_4$ transition in $YTaO_4:Pr^{3+}$ and more contribution from ${}^3P_0 \rightarrow {}^3H_4$ than ${}^1D_2 \rightarrow {}^3H_4$ transition in $LaTaO_4:Pr^{3+}$. Surface chemical changes were probed using XPS, after the phosphors were exposed to 900 $C.cm^{-2}$ electron doses *in-situ* at 1×10^{-6} Torr O_2 pressure using a 2 keV electron beam. XPS revealed that the CL degradation was caused by the formation of new species on the surface as sub-oxide, which we name Y_xO_z, and Gd_xO_z. The surface of $LaTaO_4$ phosphor was stable and no new sub oxide layer formed on its surface.

7.5. References

[1] M. Iwasaki**,** D.N. Kim**,** K. Tanaka**,** T. Murata**,** K. Morinaga**,** J. Sci. Tech. Adv. Mater. **4** (2), (2003) 137

[2] P.T. Diallo , P. Boutinaud, R. Mahiou, J.C. Cousseins, J. Phys. Stat. Sol. (a) **160** (1997) 255

[3] C. Gheorgies, P. Boutinaud, M. Loic, V.O. Atanasiu, J. Opt. Elec. Adv. Mater. **11** (5), (2005) 583-589

[4] S. Li, X. Liang, J. Mater. Sci. Mater. Elec. **19** (2008) 1147

[5] W. Tang, K. Wang, X. Bi, D. Chen, J. Mater. Sci. 42 (2007) 9915

[6] J. Zhi, A. Chen, L.K. Ju, J. Opt. Mater. **31** (2009) 1667

[7] S.H. Chen, S.H. Greef, H.C. Swart, J. Lumin. **113** (2005) 191

[8] V. Kumar, V. Mishra, S.S. Pitale, I.M. Nagpure, E. Coetzee, O.M. Ntwaeaborwa, J.J. Terblans, and H.C. Swart, J. Appl. Phys. **107** (2010) 123533

[9] S.S. Pitale, V. Kumar, I.M. Nagpure, O.M. Ntwaeaborwa, E. Coetzee, and H.C. Swart, J. Appl. Phys. **109** (2011) 013105

[10] L.L. Noto, S.S. Pitale, J.J. Terblans, O.M. Ntwaeaborwa, H.C. Swart. Physica B: Physics of Condensed Matter 2011, doi:10.1016/j.physb.2011.09.075

[11] S.S. Pitale, L.L. Noto, I.M. Nagpure, O.M. Ntwaeaborwa,J.J. Terblans and H.C. Swart, Adv. Mater. Res. **306-307** (2011) 251

[12] H.C. Swart, J.S. Sebastian, T.A. Trottier, S.L. Jones, and P.H. Holloway, J. Vac. Sci. Technol. **14** (3), (1996) 1697

[13] G. Blasse, A. Bril, J. Lumin, **3** (1970) 109.

[14] A. Hristea, E.J. Popovici, L. Muresan, M. Stefan, R. Grecu, A. Johnsson, M. Boman, J. Alloys. Compd. **471** (2009) 524.

[15] Gu, M.; Xu, X. X.; Liu, X.; Qiu L.; Zhang, R. J. Sol-gel Sci. Tech. **35** (2005) 193.

[16] E.J. Popovici, M. Nazarov, L. Muresan, D.Y. Noh, L.B. Tudoran, E. Bica, E. Indrea, J. Alloys Compd. **497** (2010) 201.

[17] V. Craciun, J. Howard, E.S. Lmabers, R.K. Singh, D. Craciun, J. Perriere, Appl. Phys. A **69** (1999) S535

[18] A. Gauzzi, H.J. Mathieu, J.H. James, B. Kellett, J. Vaccum. **41** (4 – 6), (1990) 870

[19] M. S. Dhlamini, J.J. Terblans, O.M. Ntwaeaborwa, H.C. Swart, J. Phys. Stat. Sol. **9** (2004) 2366

[20] J.H. Thomas III, L.H.Hammer, J. Electrochem. Soc. **136** (1989) 2004

[2122] D. Raiser, J.P. Deville, J. Electron Spectrosc. Relat. Phemon. **57** (1991) 91

[22] V.I. Nefedov, D. Gati, B.F. Dzhurinskii, N.P. Sergushin, Y.V. Salyn, Zh. Neorg. Khimii **20** (1975) 2307

[23] K.C. Tsai, W.F. Wu, C.G. Chao, C.P. Kuan, J. Electrochem. Soc. **153** (5), (2006) G492

[24] Y. Uwamino, T. Ishizuka, J. Electron Spectrosc. Relat. Phenom. **34** (1984) 67

[25] S.F. Ho, S. Contarini, J.W. Rabalais, J. Phys. Chem. **91** (1987) 4779

[26] W.Y. Howng, R.J. Thorn, J. Chem. Phys. Solids **41** (1980) 75

[27] D.D. Sarma, C.N.R. Rao, J. Electron Spectrosc. Relat. Phenom. **20** (1980) 25

8

Summary and future work

8.1. Summary

The work reported on this thesis is on inorganic alloys ($CaTiO_3$, $GdTaO_4$, $YTaO_4$, $LaTaO_4$) that were activated with Pr^{3+}, with the intention of exploring the luminescence characteristics of Pr^{3+}. The surface chemical stability of the compounds was evaluated by exposing the phosphors to a prolonged electron beam irradiation in-situ using Auger Electron Spectroscopy. The energy distribution of the trap levels was estimated from characterization done using thermoluminescence spectroscopy.

The compounds were prepared by solid state reaction at 1200 ^{o}C, and $CaTiO_3$ prepared by directly firing TiO_2 (Anatase phase) and $CaCO_3$ for 4h. The compound was doped with several mol% concentrations of Pr^{3+} from $PrCl_3$ compound to optimize the output emission intensity. The rare-earth tantalate phosphors were prepared by directly firing Ta_2O_5 with Y_2O_3, La_2O_3, or Gd_2O_3 for 4h to obtain $LaTaO_4$, $YTaO_4$, and $GdTaO_4$ respectively. The tantalates were doped with 0.5 mol% concentration of Pr^{3+} from $PrCl_3$ and the synthesis was carried through in the presence of 30 wt% Li_2SO_4 flux agent. The role of the flux agent in this instant was to increase the reaction rate by acting as an intermediate that converts the reagents to reactive species, lower the reaction temperature required for the final compound to form and to facilitate crystallinity to control particle sizes.

$CaTiO_3:Pr^{3+}$ phosphor with a single red emission peak around 613 nm was co-doped with In^{3+} to charge compensate the local sites where a trivalent ion Pr^{3+} substitutes for a divalent ion Ca^{2+}. It was found that In^{3+} charge compensation from 0.05 to 0.1 mol% has an effect of enhancing the red emission intensity and afterglow decay time of $CaTiO_3:Pr^{3+}$. The phosphorescence lifetime (τ) observed for different In^{3+} co-doped in $CaTiO_3:Pr^{3+}$ was 7.6 s for 0.05 mol% In^{3+}, 11.2 s for 0.1 mol% In^{3+}, 6.3 s for mol% In^{3+} and 2.03 s for mol% In^{3+}. For the orthotantalates it was approximated as 620 s for $GdTaO_4:Pr^{3+}$, 655 s for $YTaO_4:Pr^{3+}$ and 663 s for $LaTaO_4:Pr^{3+}$. The depth of the trap levels was investigated using TL.

The surface chemical stability and its effects on CL intensity under prolonged electron beam irradiation were investigated, for $CaTiO_3:Pr^{3+}$, $LaTaO_4:Pr^{3+}$, $YTaO_4:Pr^{3+}$ and $GdTaO_4:Pr^{3+}$ in-situ using AES (PHI 549) at 1×10^{-8} Torr and 1×10^{-6} Torr O_2 . The resulting surface chemical state changes were traced using XPS and the resulting layers that formed on the surface of these compounds were, TiO_2, CaO and CaO_x for $CaTiO_3$.

Surface chemical changes were probed on the surface of Tantalum oxide phosphors that were prepared by solid state reaction at 1200 ^oC, after they were exposed to 900 $C.cm^{-2}$ electron doses. The experiment was carried out to investigate the effects of the electron beam on the cathodoluminescence (CL) emission intensity of $MTaO_4:Pr^{3+}$ (M = Y, Gd and La) phosphors. X-ray diffraction (XRD) confirmed the successful formation of these phosphors, and their surface was probed by a 2 keV electron beam at 1×10^{-6} Torr O_2 pressure using Auger Electron Spectroscopy (AES) system. X-ray Photoelectron spectroscopy (XPS) was used to analyze the chemical changes that took place on the surface as a result of electron beam impingement, and it revealed the formation of new species on the surface. The newly formed species were Y_xO_z, and Gd_xO_z oxides and with $0<x<2$, and $0<z<3$. The surface of $LaTaO_4$ phosphor was stable and no new sub oxide layer formed on its surface.

8.2. Future work

The structure of $CaTiO_3$ compound is temperature dependent and at room temperature it is orthorhombic and at low temperature (<-196 ^{o}C) the compound assumes a monoclinic structure. Orthorhombic $CaTiO_3$ supports transitions from the $^1D_2$ state and at temperature lower than -196 ^{o}C it supports transitions from both $^1D_2$ and $^3P_0$. In^{3+} is also reported to generate defect levels when it is doped in a compound. The focus of the work presented in this thesis was on measurements carried out at 27 ^{o}C, where only $^1D_2$ transition is supported and $CaTiO_3:In^{3+}$ does not emit. This opens up a research opportunity focusing on the effects of In^{3+} charge compensation at temperature below -196 ^{o}C or at temperature higher than 400 ^{o}C and to search for a possible absorption from In^{3+}, which may at the end result the defect emission or transfer energy to Pr^{3+} centres and result additional increment of the phosphor's luminescence intensity.

Intervalence charge transfer has been accepted as the main reason behind the single red emission of Pr^{3+} at room temperature, which has an effect of completely depopulating the $^3P_0$ state by feeding the $^1D_2$ state. Further studies can be done by investigating the exact position of the intervalence charge transfer at different temperature. As opposed to making a conclusion based on -196 and 27 ^{o}C measurements, temperature above 400 ^{o}C should also be explored. It would also provide additional proof if XPS measurements were to be carried out at different temperature to discover more about the ability of Pr^{3+} to oxidize to Pr^{4+} at different temperature.

The rare-earth compounds were doped with 0.5 mol% base on the Pr^{3+} optimal concentration in $YTaO_4$ compound. The future approach can be on optimizing Pr^{3+} in each compound and search for the resulting effect on phosphorescence lifetime and the energy distribution of the trap levels. Techniques like Deep Level Transient Spectroscopy (DLTS) can also be used to approximate the defect levels in the material to assist the information coming from TL.

8.3. Publications

1. Pitale SS, Noto LL, Nagpure IM, Ntwaeaborwa OM, Terblans JJ, Swart HC, ***Promising Zn3Ta_2O_8:Pr^{3+} red phosphor for low voltage cathodoluminescence applications***, AMR2011 Emerging Focus on Advanced Materials – Advance Materials Research, 306-307 (2011) 251-254.

2. Noto LL, Pitale SS, Gusowski MA, Terblans JJ, Ntwaeaborwa OM, Swart HC, ***The Enhancement of Pr^{3+} red emission by adding In^{3+} as a co-dopant in $CaTiO_3$:Pr^{3+} phosphor***, Physica B: Physics of Condensed Matter, (2011), doi:10.1016/j.physb.2011.09.075

3. Noto LL, Pitale SS, Gusowki MM, Terblans JJ, Ntwaeaborwa OM, Swart HC, ***Enhancement of Pr^{3+} red emission by adding In^{3+} as co-dopant in $CaTiO_3$:Pr^{3+} phosphor***, SAIP'2011 Proceedings, the 56th Annual Conference of the South African Institute of Physics, edited by I. Basson and A.E. Botha (University of South Africa, Pretoria, 2011), p 254-257. ISBN: 978-1-86888-688-3

4. Noto LL, Pitale SS, Gusowki MA, Terblans JJ, Ntwaeaborwa OM and Swart HC, ***In^{3+} charge compensation in $CaTiO_3$:Pr^{3+}***, J. Alloys Compd. *Submitted December 2011*

5. Noto LL, Pitale SS, Gusowki MA, Ntwaeaborwa OM, Terblans JJ, Swart HC, ***Luminescent dynamics of Pr^{3+} in $MTaO_4$ host***, J. Phys. Chem. C, *Submitted January 2012*

6. Noto LL, Pitale SS, Nagpure IM, Ntwaeaborwa OM, Terblans JJ, Swart HC, ***CL emission degradation of rare-earthtantalate phosphors,*** J. Mater. Sci. *submitted January 2012*

8.4. Research presentation

The work contained in this thesis has been presented in international conferences and national conferences, including local workshops as per list below:

1. Noto LL, Pitale SS, Terblans JJ, Swart HC, ***Optimization of Pr^{3+} concentration in CaTiO$_3$ host***, the 55th Annual Conference of the South African Institute of Physics, Pretoria, South Africa, 2010 (National Conference)

2. Noto LL, Pitale SS, Terblans JJ, Ntwaeaborwa OM, Swart HC, ***Surface chemical changes of CaTiO$_3$:Pr^{3+} upon electron beam irradiation***, 4th South African Conference on Photonic Materials, Kariega, South Africa, 2011 (International conference)

3. Noto LL, Pitale SS, Gusowki MM, Terblans JJ, Ntwaeaborwa OM, Swart HC, ***Enhancement of Pr^{3+} red emission by adding In^{3+} as co-dopant in CaTiO$_3$:Pr^{3+} phosphor***, the 56th Annual Conference of the South African Institute of Physics, Pretoria, South Africa, 2011 (National Conference)

4. Noto LL, Pitale SS, Gusowski MA, Terblans JJ, Ntwaeaborwa OM, Swart HC, ***Red Emission of Pr^{3+} ions***, Workshop for photonics students, Stellenbosch, 2011 (Workshop)